RF-QPC Charge Detector and S-T_+ Qubit in a Lateral Double Quantum Dot Device

by

Jeffrey David Mason

A thesis
presented to the University of Waterloo
in fulfillment of the
thesis requirement for the degree of
Doctor of Philosophy
in
Physics

Waterloo, Ontario, Canada, 2017

I hereby declare that I am the sole author of this thesis. This is a true copy of the thesis, including any required final revisions, as accepted by my examiners.

I understand that my thesis may be made electronically available to the public.

Abstract

A measurement system is developed for studying a lateral double quantum dot (DQD) device formed in the two-dimensional electron gas (2DEG) of a GaAs/AlGaAs heterostructure. Copper powder and RC filters are constructed to isolate the device from sources of instrumentation and thermal noise, allowing the temperature of the 2DEG to reach 70 mK. Coaxial cables and bias tees allow Gaussian shaped pulses to be delivered to several depletion gates of the device for the purpose of quantum dot qubit manipulation. A conventional charge detector based on a quantum point contact (QPC) and a room temperature current preamplifier is implemented. This readout has a bandwidth of 25 kHz and a sensitivity of order $10^{-3}\ e/\sqrt{\text{Hz}}$ when using a 200 μV (3 nA) bias. To improve readout bandwidth, a radio-frequency QPC (RF-QPC) circuit is also developed. A superconducting niobium inductor, manufactured using photolithography techniques, is the basis of a 520 MHz matching network. The RF-QPC system noise temperature is 5.2 K, limited by the cryogenic semiconductor amplifier. Its sensitivity is $2\times10^{-3}\ e/\sqrt{\text{Hz}}$ when using a -85 dBm carrier. The RF-QPC has a bandwidth of 15 MHz. A summary of the first quantum dot physics measurements is provided. Data related to fundamental phenomena such as conductance quantization of a QPC, Coulomb blockade for a single dot, and spin blockade for a DQD are presented. A qubit based on two-electron spin states in a DQD (S-T_+ qubit) is created and coherent oscillations of the qubit known as Landau-Zener-Stückelberg oscillations are observed. Analysis of the spin-to-charge conversion mechanism associated with the qubit readout reveals the role played by metastable charge states, a result published in Physical Review B 92, 125434 (2015).

Acknowledgements

I would like to thank my advisor Jan Kycia. Your enthusiasm for research makes the lab an exciting place to work. Thank you to Jeff Hill and Chas Mugford for fixing leaks on the Oxford dilution fridge and teaching me how to run it. Thank you to all my fellow UW grad students including David Pomaranski, Halle Revell, Borko Djurkovic, Luke Yaraskavitch, Jeff Quilliam, Shuchao Meng, and Lauren Persaud for all the help over the years. In the NRC group, I would like to thank Zbig Wasilewski for making the 2DEG and Alicia Kam for doing the electron beam lithography. Lastly, many thanks to Sergei Studenikin and Andy Sachrajda. Certainly I would not have been able to make any quantum dot measurements without your help. I am glad we were able to publish a result together.

Dedication

This is dedicated to my parents, David and Karen Mason, my brother Luke and sister-in-law Lana. Thank you for all the support.

Table of Contents

List of Tables ix

List of Figures x

1 Lateral Quantum Dot Devices 1

1.1 Introduction 1

1.2 Two-Dimensional Electron Gas 6

1.3 Depletion Gate Layout 7

1.4 Coulomb Blockade 9

1.4.1 Coulomb Blockade Diamonds 12

1.5 Quantum Point Contact 14

1.6 DC-QPC Readout 18

1.7 Double Quantum Dot Stability Diagram 22

1.7.1 Bias Triangles 24

1.7.2 Plunger Gate Lever Arms 26

1.8 Spin Blockade for a Double Quantum Dot 29

1.9 Conclusion 32

2 Measurement System **33**

2.1 Introduction 33

2.2 Shielding, Grounding, and Wiring 33

2.3 Low-frequency Filtering 37

2.4 Electron Temperature 43

2.5 High-bandwidth Gates 50

2.6 DC-QPC Readout Sensitivity 57

2.7 Conclusion 60

3 RF-QPC Charge Detector **61**

3.1 Principle of Operation 61

3.2 Superconducting Matching Network 64

3.3 Readout Circuit 71

3.4 Noise Temperature 76

3.4.1 Noise Temperature Definition 76

3.4.2 Noise Temperature of an Amplifier Cascade 78

3.4.3 Noise Temperature of a Lossy Transmission Line 79

3.4.4 RF-QPC Noise Temperature Measurement 80

3.5 Sensitivity Theory 83

3.6 Sensitivity and Bandwidth Measurements 87

3.7 Comparison 92

3.8 Other Charge State Readout Techniques 93

3.8.1 Radio-frequency Single Electron Transistor 93

3.8.2 Quantum Capacitance Detectors 94

3.9 Conclusions and Future Work 96

4 **S-T_+ Spin Qubit** **97**

4.1 Introduction 97

4.2 Landau-Zener Effect 98

4.3 Energy Levels of Two-Electron States 99

4.4 Operation of the S-T_+ Spin Qubit 102

4.5 Spin Funnel 105

4.6 Spin-to-charge Conversion 108

4.6.1 Introduction 108

4.6.2 Role of Metastable Charge States 108

4.6.3 Telegraph Noise produced by the LZS Pulse 114

4.7 Ground State Initialization 116

4.7.1 LZS Oscillations without Applied Initialization 117

4.7.2 Boxcar Integrator 119

4.8 Conclusions and Future Work 121

References **122**

Appendices **134**

A Miscellaneous Issues with LZS Data **134**

B Two-Level Systems **139**

List of Tables

1.1 Plunger gate lever arms 28

3.1 Matching network parameters 68

3.2 RF-QPC readout parameters and charge sensitivity 92

List of Figures

1.1 Quantum dots designed by the NRC group 2
1.2 Bloch spheres for single-electron and two-electron spin qubits 3
1.3 Formation of a 2DEG in a GaAs/AlGaAs heterostructure 6
1.4 Double quantum dot depletion gate layout 8
1.5 Coulomb blockade for a single quantum dot 11
1.6 Coulomb blockade diamonds for a single quantum dot 13
1.7 Quantum point contact conductance 15
1.8 Adiabatic waveguide 17
1.9 DC-QPC readout technique 20
1.10 Double quantum dot circuit and stability diagram 22
1.11 Double quantum dot stability diagram - zero bias 24
1.12 Double quantum dot stability diagram - finite bias 25
1.13 Bias triangles for plunger gate lever arm calculation 27
1.14 Spin blockade for a double quantum dot 31

2.1 NRC device sample holder 35
2.2 NRC device wire bonding configuration 36
2.3 Copper powder filter pictures 39

2.4 Metal powder filter data . . . 41
2.5 Filter circuits . . . 43
2.6 Electron temperature measurement - conductance resonance . . . 45
2.7 Narrowest conductance resonance . . . 47
2.8 Electron temperature measurement - width of charge transfer line . . . 48
2.9 High-bandwidth gate circuit diagram . . . 52
2.10 High-bandwidth gate lines and coax heat sinking . . . 53
2.11 Frequency response of the high-bandwidth gates . . . 54
2.12 Calibration of the high-bandwidth gates . . . 55
2.13 Tunnel rate measurement technique . . . 56
2.14 DC-QPC sensitivity and bandwidth analysis . . . 58
2.15 Delft device and DC-QPC noise spectrum . . . 59

3.1 Matching network . . . 62
3.2 Superconducting matching network data . . . 66
3.3 Examples of S_{11} versus frequency data . . . 69
3.4 Optical lithography process for the niobium inductor . . . 70
3.5 RF-QPC circuit on the dilution refrigerator . . . 72
3.6 Pictures of the RF-QPC circuit components . . . 73
3.7 Frequency response of several RF-QPC components . . . 75
3.8 Thévenin equivalent circuit of a resistor . . . 76
3.9 Amplifier noise temperature definition . . . 77
3.10 Noise temperature of a cascade of three amplifiers . . . 79
3.11 Noise temperature of a lossy transmission line . . . 80

3.12 QPC shot noise as a function of DC bias 82

3.13 Homodyne receiver circuit 84

3.14 RF-QPC sensitivity analysis 89

3.15 RF-QPC bandwidth and carrier power 91

3.16 Charge detection using an RF-SET 94

3.17 Measurement of the quantum capacitance of a double quantum dot 95

4.1 Landau-Zener effect 98

4.2 Two-electron spin state energy levels 100

4.3 Operation of the S-T_+ qubit 102

4.4 LZS gate voltage pulse 103

4.5 Spin funnel 106

4.6 Magnetic field dependence of the S-T_+ anticrossing 107

4.7 LZS experiment in the few electron regime of a double quantum dot 109

4.8 LZS oscillations and telegraph noise in a stability diagram 111

4.9 Spin-to-charge conversion mechanisms involving metastable charge states . 112

4.10 QPC transconductance as a function of detuning and pulse duration 114

4.11 Ground state initialization techniques 117

4.12 LZS oscillations without applied initialization - NRC data 118

4.13 QPC transconductance as a function of pulse duration 119

4.14 Measurement of LZS oscillations using the RF-QPC and boxcar integrator 120

A.1 LZS distortions parallel to the sweep direction 135

A.2 Effect of V_{QPC} on the LZS oscillations 136

A.3 Artifact in the LZS data produced by the RF-QPC carrier 137

A.4 Effect of decreasing the top gate voltage on the LZS oscillations 138
A.5 Effect of decreasing the right side gate voltage on the LZS oscillations . . . 138

B.1 Two Level Systems and the Bloch Sphere 141

Chapter 1

Lateral Quantum Dot Devices

1.1 Introduction

A quantum dot is a submicron structure that confines electrons or holes in all three dimensions on length scales of tens of nanometers. The confinement potential forces the electrons in the dot to occupy discrete energy levels similar to the electrons of an atom. Quantum dots are thus sometimes referred to as artificial atoms. They have been realized in many systems including nanoparticles [1], carbon nanotubes [2], and semiconducting nanowires [3]. This work concerns quantum dots formed in the two-dimensional electron gas (2DEG) of a GaAs/AlGaAs heterostructure. Scanning electron microscopy (SEM) images of such devices designed by the Sachrajda group at the National Research Council Canada (NRC) are displayed in Fig. 1.1. From left to right are shown a single, double, and triple quantum dot device. Each device is composed of metallic electrodes called gates patterned on top of the heterostructure using electron beam lithography techniques. Applying negative voltages to these gates depletes the underlying 2DEG, creating electron puddles at the positions marked by the white circles. These puddles are the quantum dots. By tuning the gate voltages, the number of electrons occupying each dot can be reduced from hundreds to 2, 1, or even 0.

This work details the first steps towards establishing a quantum dot research program in a low temperature physics laboratory. The ultimate goal is to study quantum dot physics

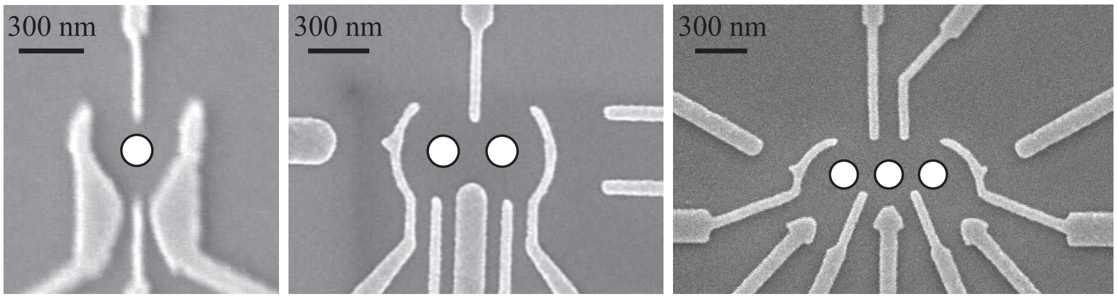

Figure 1.1: SEM images of depletion gate layouts for single, double, and triple quantum dot devices. The white circles show the approximate positions of the dots. All three devices are designed by the NRC group.

as it relates to the ongoing effort to implement a quantum computer. The development of the field of quantum computing with quantum dot devices has been guided over the past nearly 20 years by a 1998 paper of David DiVincenzo and Daniel Loss [4, 5]. In the paper, the authors propose a quantum computer based on single-electron spin states. The geometry of their proposed device is similar to that of the double quantum dot (DQD) and the linear triple quantum dot (TQD) devices of Fig. 1.1(b,c). Each dot contains a single electron spin and the tunnel barrier between dots is controlled with the metallic gates. The qubit basis states are the Zeeman split states $|\uparrow\rangle$ and $|\downarrow\rangle$ of an electron in a magnetic field.

For a general set of basis states $|0\rangle$ and $|1\rangle$, any qubit state $|\psi\rangle = \cos(\theta/2)\,|0\rangle + e^{i\phi}\sin(\theta/2)\,|1\rangle$ is represented by a unit vector on the Bloch sphere with polar and azimuthal angles θ and ϕ [Fig. 1.2(a)]. The Bloch sphere representation of the single-electron spin qubit is shown in Fig. 1.2(b). The basis states $|\uparrow\rangle$ and $|\downarrow\rangle$ are located on the z-axis and equal weighted superpositions are located in the transverse plane. The superposition states $(|\uparrow\rangle + |\downarrow\rangle)/\sqrt{2}$ and $(|\uparrow\rangle - |\downarrow\rangle)/\sqrt{2}$ define the x-axis. The red vector represents the system in the $|\uparrow\rangle$ state. Moving the vector to any point on the sphere requires two types of rotations, typically a z-axis and an x-axis rotation are employed. These are the single-qubit gate operations. A rotation about the x-axis $|\uparrow\rangle \leftrightarrow |\downarrow\rangle$ is achieved using the electron spin resonance (ESR) technique while the energy difference between the basis states produces coherent rotations $(|\uparrow\rangle + |\downarrow\rangle)/\sqrt{2} \leftrightarrow (|\uparrow\rangle - |\downarrow\rangle)/\sqrt{2}$ about the z-axis. Two-qubit operations are achieved using the metallic gates to tune the tunnel barrier between dots thus controlling the exchange energy for neighboring electrons. Such a technique allows, for example, the implementation of the SWAP gate $|\uparrow\downarrow\rangle \rightarrow |\downarrow\uparrow\rangle$. In addition to possessing this universal set of quantum gate operations, the proposed quantum computer satisfies other Divincenzo criteria [6]; it is scalable, the qubits can be initialized to a fiducial state (eg. ground state by cooling in a magnetic field), and qubit readout is possible using the spin-to-charge conversion technique (Section 4.6). A qubit based on the DiVincenzo/Loss proposal has been implemented in a DQD device [7].

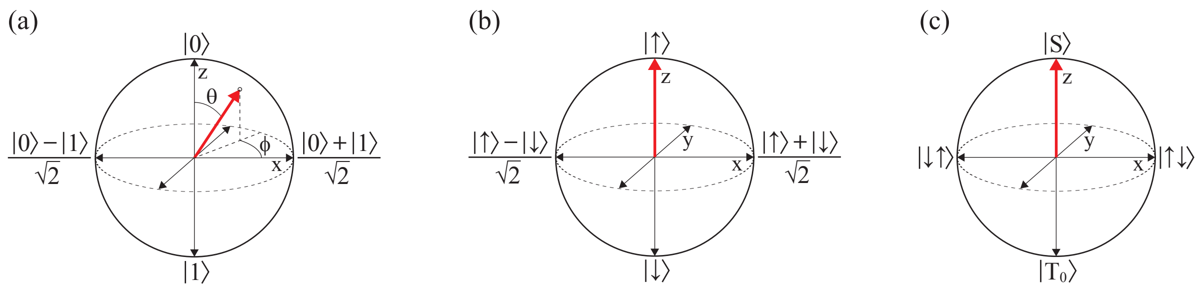

Figure 1.2: Bloch sphere for (a) general qubit [$0 \leq \theta \leq \pi$ and $0 \leq \phi < 2\pi$] (b) single-electron spin qubit, and (c) two-electron singlet-triplet qubit S-T_0. The red unit vector represents the qubit state.

For any device to form the basis of a viable quantum computer, the lifetime of a qubit must be long relative to the time required to execute a gate operation. The qubit lifetime is characterized with three timescales, T_1, T_2, and T_2^*. The T_1 time refers to the decay of the excited qubit state to the ground state. In the case of single-electron spin states, this means a $|\uparrow\rangle \rightarrow |\downarrow\rangle$ transition which occurs on a timescale $T_1 > 1$ s in a 1 T magnetic field [8]. The timescale associated with the decay of a superposition state is called the decoherence time and labeled T_2. For the single-electron qubit, $T_2 = 0.44$ μs has been achieved using a spin-echo technique similar to that used in nuclear magnetic resonance experiments [9]. Since the qubit readout procedure generally requires an average over an ensemble rather than the measurement of a single system, a related quantity called the dephasing time, T_2^*, is sometimes used to characterize the decay of a superposition state.

For single electron spins in GaAs/AlGaAs heterostructures, T_2^* in the tens of nanoseconds range is typical. For example, $T_2^* = 37$ ns is reported in Ref. [9]. The single-qubit gate operation $(|\uparrow\rangle + |\downarrow\rangle)/\sqrt{2} \rightarrow (|\uparrow\rangle - |\downarrow\rangle)/\sqrt{2}$ requires ~0.1 ns while the $|\uparrow\rangle \rightarrow |\downarrow\rangle$ operation can be executed in 20 ns [10]. The two-qubit SWAP gate can be achieved in 350 ps [11]. Typically ~10^4 operations must be performed within a decoherence time [12, 13] so work remains to decrease the gate operation time and/or increase T_2.

The dephasing of the electron spin is primarily the result of the hyperfine interaction with the nuclear spins of the substrate. Each electron interacts with approximately 10^6 spin-3/2 Ga and As nuclei and the effect of the nuclear spins on the electron spin is commonly described with reference to an effective nuclear field called the Overhauser field. The root-mean-square of the statistical fluctuation of this internal field is a few mT [14]. It is these fluctuations of the nuclear field that lead to the decoherence of the electron spin.

In addition to using single-electron spin states to create qubits, a qubit based on two-electron spin states can also be implemented in a quantum dot device. The qubit basis states are the singlet $|S\rangle = (|\uparrow\downarrow\rangle - |\downarrow\uparrow\rangle)/\sqrt{2}$ and either the $m = 0$ triplet $|T_0\rangle = (|\uparrow\downarrow\rangle + |\downarrow\uparrow\rangle)/\sqrt{2}$ or the $m = +1$ triplet $|T_+\rangle = |\uparrow\uparrow\rangle$. Such singlet-triplet qubits are realized in a DQD device with each of the two tunnel coupled dots occupied by a single electron.

The Bloch sphere for the S-T_0 qubit is shown in Fig. 1.2(c). The $|S\rangle$ and $|T_0\rangle$ basis states define the z-axis and the states $|\uparrow\downarrow\rangle$ and $|\downarrow\uparrow\rangle$, which are linear superpositions of $|S\rangle$ and $|T_0\rangle$, define the x-axis. A magnetic field gradient parallel to the external field is provided by the nuclear spins or a micromagnet. This creates an energy difference between the states $|\uparrow\downarrow\rangle$ and $|\downarrow\uparrow\rangle$ thus producing a rotation $|S\rangle \leftrightarrow |T_0\rangle$ about the x-axis . This operation can be achieved on subnanosecond timescales [15]. The metallic gate controlled finite exchange energy for the two electrons creates an energy difference between $|S\rangle$ and $|T_0\rangle$ and drives rotations $(|T_0\rangle + |S\rangle)/\sqrt{2} \leftrightarrow (|T_0\rangle - |S\rangle)/\sqrt{2}$. This is the single-electron qubit SWAP gate operation $|\uparrow\downarrow\rangle \leftrightarrow |\downarrow\uparrow\rangle$ and, as mentioned above, can be executed in 350 ps [11]. Two-qubit operations are realized by capacitively coupling two DQDs. Using the spin blockade phenomenon, the spin/charge configuration of one DQD controls the exchange energy and therefore the oscillation frequency of the other DQD [16, 17]. The T_1 for the S-T_0 qubit is on the order of milliseconds [18]. If the magnetic field gradient is provided by the nuclear spins, $T_2^* = 10$ ns although the decoherence time, T_2, has been increased to 276 μs using the Carr-Purcell-Meiboom-Gill spin-echo technique [19]. It is thus possible to reach ~10^4 gate operations in a decoherence time provided the two-qubit gate can be executed in less than 30 ns [16].

Relative to the S-T_0 qubit, the S-T_+ qubit is a recent development in the field. It was first demonstrated in Ref. [20] and theoretical proposals for single and two-qubit gates have been presented [21]. Operation of the qubit requires a magnetic field gradient transverse to the external field, typically provided by the nuclear spin system. The coupling of the $|S\rangle$ and $|T_+\rangle$ states that results from this field gradient produces an anticrossing in the energy level spectrum. Superposition states of $|S\rangle$ and $|T_+\rangle$, and thus single-qubit operations, are realized by means of Landau-Zener tunneling at this anticrossing. Limited by fluctuations in the nuclear spin system, $T_2^* = 10$ ns [20]. Because our NRC collaborators have shown recent interest in the Landau-Zener tunneling phenomenon [22, 23], the S-T_+ qubit is investigated in this work. A discussion is found in Chapter 4.

Important for any implementation of a quantum computer is the ability to quickly and accurately measure the states of the qubits. In the case of spin qubits in a quantum dot device, such a readout technique employs an electric field sensor such as a quantum point contact (QPC) [24] and a technique for mapping each qubit spin state to a unique charge configuration that can be distinguished with the sensor. This latter requirement is usually achieved using the spin blockade phenomenon [25]. A now common technique for increasing the fidelity of the qubit state measurement (i.e. lowering the probability of making an error) by increasing the measurement speed is to embed the QPC in a radio-frequency (rf) resonant circuit [26, 27]. The resulting sensor is known as an RF-QPC. Details related to the implementation of this technique are provided in Chapter 3.

This first chapter reviews basic quantum dot physics. It begins with more detailed discussions of the 2DEG and quantum dot formation using the metallic depletion gates. Analysis of electrical transport measurements follow. They reveal the fundamental phenomena of Coulomb blockade and conductance quantization. With this foundation, charge detection using a quantum point contact (QPC) and the creation of a charge stability diagram are then discussed. The chapter ends with a section concerning the phenomenon of spin blockade, necessary for the spin qubit study of Chapter 4.

1.2 Two-Dimensional Electron Gas

Consider the bandstructure diagrams of the physically separated intrinsic GaAs and Si doped n-$Al_xGa_{1-x}As$ layers shown in Fig. 1.3(a) [28]. Following Anderson's rule, the diagrams are drawn with reference to the vacuum level, E_{vac} [29]. The electron affinity χ_1 (χ_2) is the energy required for an electron at the bottom of the conduction band, E_{C1} (E_{C2}), to escape the n-$Al_xGa_{1-x}As$ (GaAs) crystal. Electrons at the top of the valance band in the n-$Al_xGa_{1-x}As$ and GaAs crystals have energies E_{V1} and E_{V2} respectively. The conduction and valance band offsets $\Delta E_C = E_{C1} - E_{C2}$ and $\Delta E_V = E_{V1} - E_{V2}$ are tuned with the concentration x. The Si donor energy levels and thus the Fermi energy, E_{F1}, lie near the conduction band edge on the n-$Al_xGa_{1-x}As$ side. Being an intrinsic semiconductor, the Fermi energy of the GaAs layer, E_{F2}, is located in the middle of the band gap.

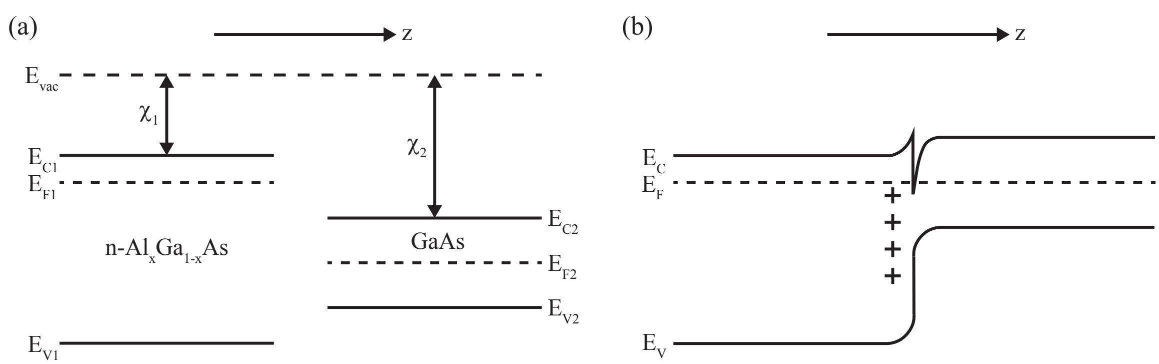

Figure 1.3: (a) Energy band diagrams of physically separated n-doped $Al_xGa_{1-x}As$ and intrinsic GaAs crystals. (b) Equilibrium energy band diagram of a heterostructure of the two semiconductors. The electric field resulting from the electrons and their positively charged Si donor ions (+) bends the energy bands creating a potential well that dips below the Fermi energy and thus a two-dimensional electron gas near the interface.

In the context of a heterostructure, with the materials in contact, some of the electrons released by the Si donors cross into the GaAs layer until a common Fermi level, E_F, is established across the entire heterostructure. This process leaves behind non-neutralized positively charged donor impurities in the n-$Al_xGa_{1-x}As$ layer. This separation of electrons and ionized donors creates an electrostatic potential, $\phi(z)$, that attempts to drive the electrons back into the n-$Al_xGa_{1-x}As$ layer. The step in conduction band energy, however, prevents the electrons from returning to the donors. The electrostatic potential simply pushes the electrons against the interface of the two materials. Including this electrostatic energy, $-|e|\phi(z)$, produces the equilibrium band diagram of Fig. 1.3(b). The result is a potential well in the conduction band near the interface on the GaAs side. If the concentration, x, and the doping level are chosen appropriately, this potential well can be engineered to dip below E_F, leading to a layer of electrons near the interface. Since this layer has a thickness of 5-10 nm, discrete energy levels called z-subbands are created with a typical spacing of ~100 meV [30]. This large energy level spacing combined with the low electron density (~10^{15} m^{-2}) means that only the lowest z-subband is typically occupied. In this case, the electron gas is viewed as two-dimensional with free plane wave motion within the interface layer.

1.3 Depletion Gate Layout

A scanning electron microscopy image of the NRC split-gate device is shown in Fig. 1.4(a). The nine labeled TiAu metallic gates (T, LS, LP, C, RP, RS, Q1, Q2, Q3) are located on top of the GaAs/AlGaAs heterostructure. Schematic cross sections of the device cutting through three gates and the underlying 2DEG are sketched in (b)-(e). Although not drawn to scale, the sketches are intended to correspond to a cross-section taken at the position of the dashed line in (a). Since the low electron density of the 2DEG, $n_s = 2.1 \times 10^{15}$ m^{-2}, corresponds to a large Fermi wavelength, $\lambda_f = \sqrt{2\pi/n_s} = 55$ nm, and a large screening length, the electric field of a gate will locally deplete the 2DEG lying 90 nm below [14]. From (b) to (e), the three gate voltages are made progressively more negative with respect to the 2DEG. In (b), the gates are grounded and the 2DEG is undisturbed. Depletion directly underneath the gates is shown in (c) and, to some extent, also between the gates in (d). At approximately -1 V the 2DEG is completely depleted, leaving the electrically insulating region shown in (e). The ability to vary the electron density between pairs of gates allows the formation of variable resistance constrictions in the 2DEG, examples of which are represented as pairs of curved lines in (a).

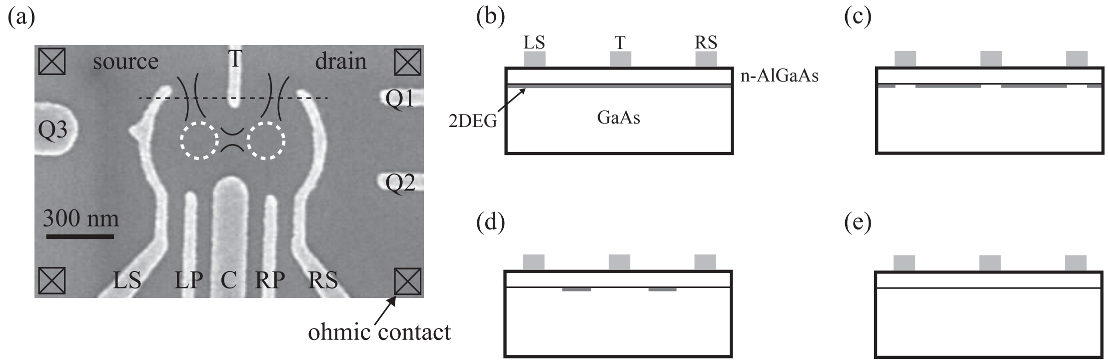

Figure 1.4: (a) SEM image of the the DQD device. Dashed white circles indicate the approximate positions of the quantum dots. Pairs of curved black lines indicate constrictions in the 2DEG that determine the dot-to-dot and dot-to-lead tunneling resistances. Positions of ohmic contacts to the 2DEG are indicated with ⊠. (b)-(e) Cross-sections through the heterostructure and three surface gates at the position of the dashed line in (a). From (b) to (e), the gate voltages decrease, changing the degree of 2DEG depletion.

For typical gate voltages of $V_T = V_{LP} = V_{RP} \approx -0.5$ V and $V_{LS} = V_C = V_{RS} \approx -1$ V, the 2DEG is depleted in such a way as to form two quantum dots near the positions marked by white dashed circles on the SEM image. The left and right side gate voltages, V_{LS} and V_{RS}, play the dominant role in determining the electrostatic energy of the dots. The tunnel coupling (resistance) between the dots is controlled primarily with V_C and the coupling to the leads (electron reservoirs in top left and top right labeled source and drain) is tuned using V_T. Fine tuning of the dot energies is accomplished with the left and right plunger gate voltages, V_{LP} and V_{RP}. Ohmic contacts to the 2DEG allow for the performance of electrical transport measurements. With a proper tuning of the gate voltages, each dot contains a well defined number of electrons. Each DQD charge state is labeled (N_1,N_2), where N_1 (N_2) electrons occupy the left (right) dot. For example (2,1) means two electrons on the left dot and one electron on the right dot.

1.4 Coulomb Blockade

Before discussing DQD physics, it is useful to analyze an electrical transport measurement involving a single quantum dot. Starting with a DQD structure, a single dot is formed by simply increasing V_C until the central potential barrier separating the dots is eliminated. A circuit diagram of the resulting configuration is superimposed on an SEM image in Fig. 1.5(a). The single dot, represented by a white circle, is shown tunnel coupled to source and drain leads and capacitively coupled to the gate labeled with a generic G in this section. Tunnel coupling implies both a capacitive coupling to the leads and an electrically resistive connection through which the quantum dot can exchange electrons with the leads. Only the effect of gate G is considered in the following development. The other gates are held constant at the voltages required to form the single dot. Consider the quantum dot to contain charge Q at voltage V. The source, drain, and gate are connected to voltage sources V_S, V_D, and V_G and electrostatically coupled to the quantum dot through capacitors C_S, C_D, and C_G. The electrostatic energy of the quantum dot, U_e, is calculated as a function of these six parameters. Begin by calculating the charge on each of the three capacitors. The voltage across the source capacitor is $V - V_S$, implying a stored charge of $C_S(V - V_S)$. Proceeding in a similar manner for the drain and gate capacitors and summing the results produces the expression

$$Q = C_S(V - V_S) + C_D(V - V_D) + C_G(V - V_G).$$

Define the capacitance of the single dot as $C = C_S + C_D + C_G$, solve for CV, and substitute into $U_e = \frac{1}{2}CV^2 = C^2V^2/2C$ to give the expression for the electrostatic energy of the quantum dot

$$U_e(N) = \frac{\left[-(N - N_0)|e| + C_S V_S + C_D V_D + C_G V_G\right]^2}{2C},$$

where $Q = -(N - N_0)|e|$ has been used. N is the number of electrons that occupy the quantum dot with the gates energized and N_0 is the number of electrons in the dot required to compensate the positive donors when the voltage sources are all zero [31]. The confinement potential that leads to the quantization of charge number also produces a discrete energy spectrum, similar to an atom. Adding these single particle energies, E_i, to the electrostatic part gives an expression for the total energy of the quantum dot [14]

$$U(N) = \frac{[-(N - N_0)|e| + C_S V_S + C_D V_D + C_G V_G]^2}{2C} + \sum_{i=1}^{N} E_i. \tag{1.1}$$

Analysis of electrical transport does not, however, typically make use of $U(N)$ directly due to its quadratic dependence on V_G. Instead transport phenomena are discussed with reference to a related quantity, the electrochemical potential, defined as $\mu(N) = U(N) - U(N-1)$. It is the change in dot energy associated with adding the N^{th} electron to an $N-1$ electron quantum dot (only ground states are considered here). Using Eq. 1.1, produces an expression for the electrochemical potential

$$\mu(N) = \left(N - N_0 - \frac{1}{2}\right)E_C - \frac{E_C}{|e|}(C_S V_S + C_D V_D + C_G V_G) + E_N, \tag{1.2}$$

where $E_C = e^2/C$ is referred to as the charging energy. The energy difference between consecutive electrochemical potentials, called the addition energy, is given by

$$E_{add}(N) = \mu(N+1) - \mu(N) = E_C + \Delta E,$$

where ΔE is the energy difference between two discrete energy levels. For lateral gated quantum dots formed in GaAs/AlGaAs heterostructures, $E_C \approx$1 meV and $\Delta E \approx$100 μeV as shown in the following subsection [32].

The electrochemical potentials, approximately equally spaced by E_C, are represented in quantum dot energy diagrams by a ladder of levels as shown in Fig. 1.5(b). Source and drain leads contain Fermi-Dirac distributions of electrons with chemical potentials μ_S and μ_D respectively. A voltage bias, $V_{SD} = V_S - V_D$, is applied producing an energy difference between the leads, $\mu_{SD} = \mu_S - \mu_D = -|e|V_{SD}$, called the bias window. Referring to Eq. 1.2, note that V_G can be used to move the ladder of electrochemical potentials up and down in energy while maintaining the energy difference between levels. The value of V_G chosen in the left-hand energy diagram places $\mu(N)$ within the bias window. In this case of $|V_{SD}| \approx 0$, the energy gained by removing an electron from the source is equal to the energy required to add the N^{th} electron to the dot. Also, with the N^{th} electron in the dot, the energy gained by removing it from the dot is equal to the energy required

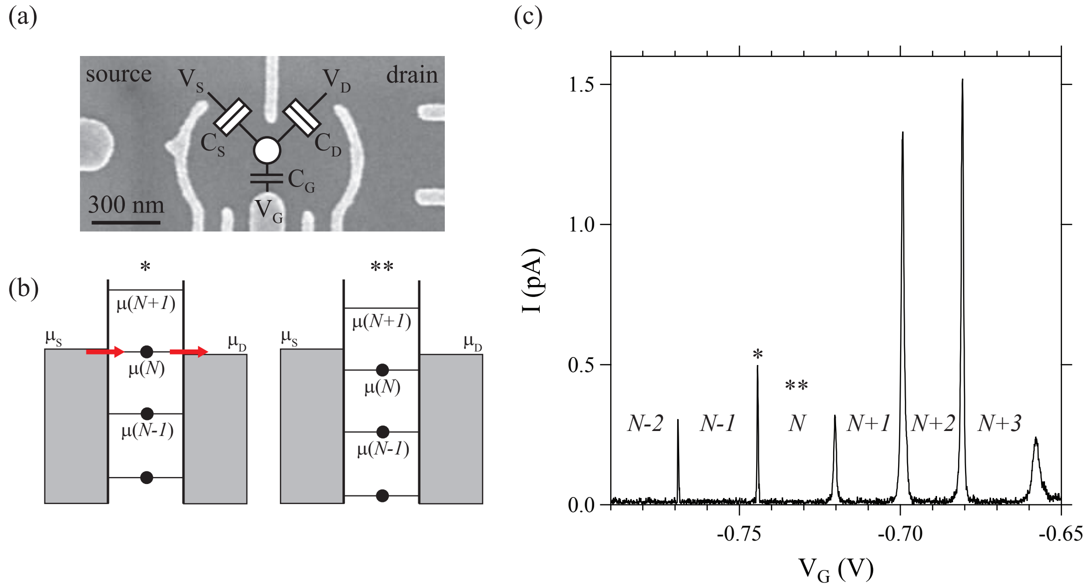

Figure 1.5: (a) Single quantum dot circuit shown on an SEM image of the device. The quantum dot (white circle) is tunnel coupled to the source and drain leads and capacitively coupled to the gates. (b) Energy level diagrams showing the arrangement of levels for the single electron transport ($*$) and Coulomb blockade ($**$) conditions. (c) Electrical current flowing through a single quantum dot as a function of V_G. As V_G decreases, the number of electrons occupying the dot changes from N to $N-1$ at the peak labeled $*$.

to add it to the drain [32]. Single electron transport between a filled state in the source and an empty state in the drain via the quantum dot is thus possible. The magnitude of the current depends on the tunnel rate between the dot and the leads. In the right-hand diagram, V_G is set so that no level lies within the bias window and transport between the source and drain cannot occur (ignoring cotunneling). This current blocking phenomenon, being related to the electrostatic (charging) energy of the quantum dot, is called Coulomb blockade. Fig. 1.5(c) is a plot of the current flowing through a quantum dot as a function of V_G. The plot shows peaks in current due to single electron tunneling events ($*$) and regions of Coulomb blockade ($**$). As V_G decreases, the number of electrons on the single dot changes from N to $N-1$ at the $*$ peak. Although Coulomb blockade is easily observed using a DC bias, the data in the figure is actually the result of an AC current measurement. A 0.5 μV_{rms}, 12 Hz sine wave is applied to the source lead with a lock-in amplifier and the resulting current is measured with a DL Instruments, model 1211 current preamplifier (Ithaco) connected to the drain lead. The lock-in measures the output of the Ithaco.

Note that observation of this Coulomb blockade phenomenon requires that the quantum dot be coupled to the leads but still possess a well defined number of electrons. The Heisenberg uncertainty relation provides an estimate of the required dot-to-lead tunneling resistance. Since the electrochemical potentials are spaced by the charging energy $E_C = e^2/C$ (ignoring the single electron levels due to the confinement potential), quantization of the electron number on a quantum dot requires that the uncertainty in the dot energy, ΔE, be less than E_C. If the dot has capacitance C and the tunneling resistance is R_t, the RC time constant for charging the dot is $\Delta t = R_t C$. Setting $\Delta E = E_C$, the uncertainty relation, $\Delta E \Delta t > h$, then produces a lower bound for R_t of $h/e^2 \approx 25.8$ kΩ [32].

1.4.1 Coulomb Blockade Diamonds

The data and energy level diagrams of Fig. 1.5 correspond to the case $|V_{SD}| \gtrsim 0$. Fig. 1.6(a) shows the effect of increasing $|V_{SD}|$. It is a color scale plot of dI/dV_{SD} as a function of V_{SD} and V_G. The measurement involves applying a DC voltage to the source lead and measuring the dot current with an Ithaco connected to the drain lead. A numerical derivative produces the figure. The six labeled points correspond to the electrochemical potential level diagrams (b)-(g). Note that as V_G is increased for $V_{SD} \approx 0$, peaks in dI/dV_{SD} corresponding to the three leftmost peaks in Fig. 1.5(c) are observed. The values of V_G at which these resonances occur are not the same in the two figures due simply to device drift in the time between the measurements. Non-zero current and non-zero dI/dV_{SD} is measured at $V_{SD} = 0$ perhaps because of a DC offset voltage produced by the Ithaco or thermocouple voltages produced at solder joints due to temperature gradients along the fridge wiring. Probably due simply to the coarse resolution of the data plot along the V_{SD} axis, there does not seem to be a value of V_{SD} at which the current is zero.

As $|V_{SD}|$ increases from zero, triangular shaped regions open up. The edges of these triangles which are extended as black lines for $|V_{SD}| > 1$ mV intersect to form diamond

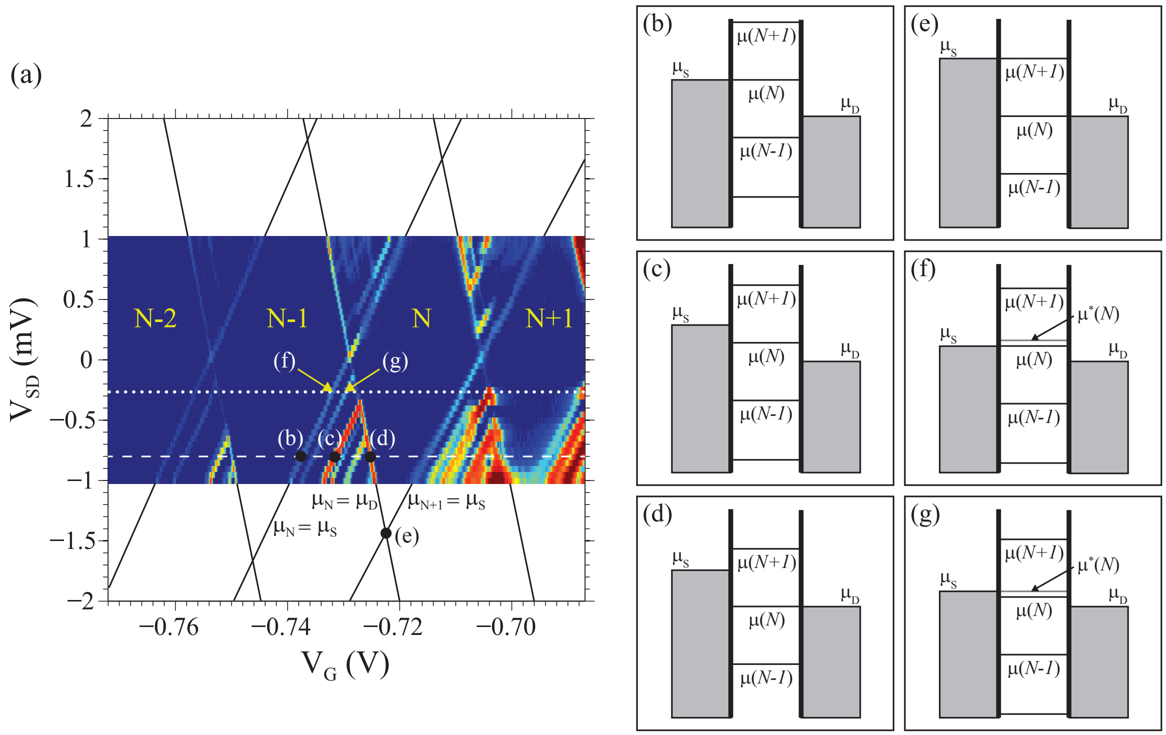

Figure 1.6: (a) Coulomb blockade diamonds for a single quantum dot. Plot of dI/dV_{SD} as a function of bias V_{SD} and gate voltage V_G. Labeled points correspond to the energy level diagrams in (b)-(g).

shaped regions of Coulomb blockade. For this reason, such data sets are referred to as Coulomb blockade diamonds. These diamonds, labeled $N-2$, $N-1$, N, and $N+1$ in the figure, are a generalization of the regions between current peaks in the limit of small $|V_{SD}|$ shown in Fig. 1.5(c). Each positive (negative) sloped edge corresponds to a resonance between a dot level and the source (drain) lead. Several are labeled in the figure. Consider increasing V_G along the horizontal dashed line at $V_{SD} = -800\ \mu V$. At the point labeled (b), $\mu(N) = \mu_S$ and current through the dot begins to flow via the cycle $N-1 \rightarrow N \rightarrow N-1$, producing a peak in dI/dV_{SD}. As V_G is increased further, current continues to flow [point (c)] until $\mu(N) = \mu_D$ at point (d) and the current stops, producing another peak in

dI/dV_{SD}. Note that in moving from point (b) to (d), the dot energy decreases by $|eV_{SD}|$ as V_G increases. This change in energy is linearly related to the corresponding change in gate voltage, ΔV_G [32]. The proportionality constant is called the lever arm for the gate, typically labeled α. Therefore, by definition, $|eV_{SD}| = \alpha|\Delta V_G|$ and the lever arm is given by the simple expression $\alpha = |eV_{SD}|/|\Delta V_G|$. The dashed line at $V_{SD} = -800$ μV intersects three triangular regions, each giving a slightly different value for ΔV_G. The resulting values for α lie in the range 70-75 meV/V. Consider the point labeled (e), located at the intersection of the $\mu(N) = \mu_D$ and $\mu(N+1) = \mu_S$ lines. Since $\mu_S - \mu_D = -|e|V_{SD}$ and $\mu(N+1) - \mu(N) = E_{add}$, $E_{add} = -|e|V_{SD}$. For point (e), $V_{SD} = -1.4$ mV and so $E_{add} = 1.4$ meV.

Within each triangular region, there are several lines that run parallel to the boundary edges. These correspond to excited states. Consider the boundary (i.e. ground state) and excited state lines that intersect the horizontal dotted line at points (f) and (g) respectively. Moving V_G positive along the dotted line, $\mu(N) = \mu_S$ at the boundary point (f) and the dot current increases, producing a peak in dI/dV_{SD} similar to point (b). Further increase of V_G produces another change in current and thus another peak in dI/dV_{SD} at point (g) where $\mu^*(N) = \mu_S$, $\mu^*(N)$ being the electrochemical potential for an excited state of the N-electron dot. Since $\mu^*(N)$ corresponds to a transition between the $(N-1)$-electron ground state and the N-electron excited state while $\mu(N)$ is the energy difference between ground states, $\mu^*(N)$ is larger than $\mu(N)$ by the excitation energy of the N-electron dot. Similar to the lever arm calculation, $\mu^*(N) - \mu(N) = \alpha\Delta V_G$, so knowing α and taking the value of ΔV_G required to move between the (f) and (g) (at constant V_{SD}) allows a calculation of the excitation energy. For this particular excited state, the excitation energy is 150 μeV. Incidentally, since $E_C = E_{add} - \Delta E$, the charging energy is about 1.25 meV.

1.5 Quantum Point Contact

The conductance of constrictions in the 2DEG are tuned by adjusting gate voltages as shown in Fig. 1.7(a). As the gate voltages decrease, the extent of depletion of the 2DEG increases and the general trend is a decreasing conductance; zero conductance is called the pinch-off regime. The most notable aspects of the data are the plateaus at integer multiples of $G_Q = 2e^2/h$ [33, 34]. Constrictions displaying such behavior are called quantum point contacts (QPCs).

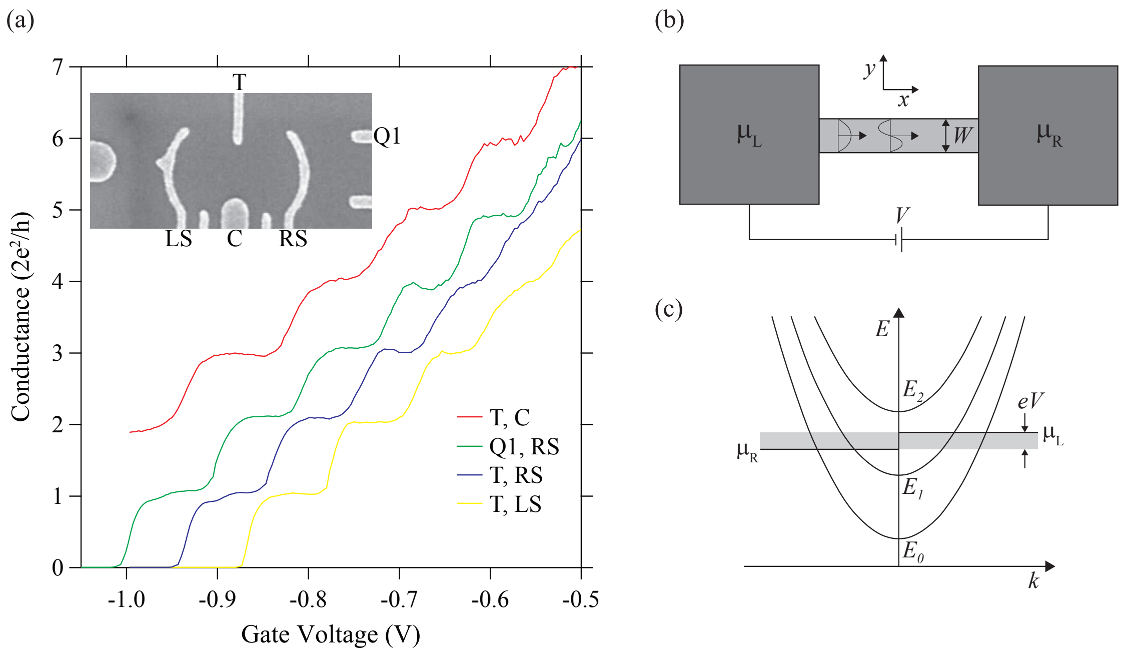

Figure 1.7: (a) Conductance as a function of gate voltage for several QPCs of the device. Inset: SEM image of the device with gate labels. (b) A voltage bias is applied between two electron reservoirs (contacts) connected by a ballistic conductor. Boundary conditions in the y-direction force the electron wavefunction to have nodes at the edges of the conductor. (c) Parabolic dispersion for three channels. The lowest two channels participate in transport [32].

A discussion of quantized conductance begins by approximating the QPC as a ballistic conductor of width W connecting two electron reservoirs (contacts) as shown in Fig. 1.7(b) [30]. Confinement of the electron wave function in the y-direction by infinite potential barriers leads to quantization of the electron motion and the following expression for the energy eigenvalues [35]:

$$E_{n,k} = \frac{\hbar^2 k^2}{2m} + E_n, \quad E_n = \frac{\pi^2 \hbar^2}{2mW^2} n^2, \tag{1.3}$$

where k is the x-component of the wavevector. The first term results from the free plane wave motion along the length of the conductor (x-direction) and second term, E_n, is related to the width of the wire. The index n, the quantum number that arises due to the confinement potential, labels a subband or channel. Each channel possesses a parabolic energy dispersion with a different cut-off energy, E_n, examples of which are shown in Fig. 1.7(c) [32].

Calculate the current flowing through the conductor that results from an applied bias voltage. For each channel, n, integrate the product of electron charge, e, and velocity, $v(k)$, over the one-dimensional k-space to produce an expression for the current traveling from left to right (i.e. states with $k > 0$)

$$I_L = 2e \sum_n \int_0^\infty \frac{dk}{2\pi} v(k) f(k),$$

where $f(k)$ is the occupation function and the factor of two accounts for spin. Use the definition of group velocity, $v(k) = (1/\hbar) dE/dk \Rightarrow dk = dE/\hbar v(k)$ to convert to an energy integral

$$I_L = \frac{2e}{h} \sum_n \int_{E_n}^\infty f(E, \mu_L) dE,$$

where the occupation function is taken to be $f(E, \mu_L)$, the Fermi function for the left reservoir. Similarly for current due to electrons traveling right to left (i.e. states with $k < 0$)

$$I_R = -\frac{2e}{h} \sum_n \int_{E_n}^\infty f(E, \mu_R) dE,$$

where the minus sign is required because the current is traveling in the opposite direction to I_L. The net current is given by

$$I = I_L + I_R = \frac{2e}{h} \sum_n \int_{E_n}^\infty [f(E, \mu_L) - f(E, \mu_R)] dE. \tag{1.4}$$

In the limit of zero temperature, the Fermi functions are replaced by step functions and the net current becomes

$$I = \frac{2e}{h} N(\mu_L - \mu_R) = G_Q N V,$$

where the voltage bias is $V = (\mu_L - \mu_R)/e$ and N is the number of channels with $E_n < \mu_R$, called open channels (Fig. 1.7(c); assume no cutoff energy within the gray shaded bias window). Clearly the conductance is quantized in units of $G_Q = 2e^2/h$. The corresponding resistance $R_c = 12.9$ kΩ per channel in the case of this ballistic conductor (i.e. no electron scattering) results from power dissipation of the electrons and holes in the contacts [30, 32]. The resistance R_c is therefore called the contact resistance.

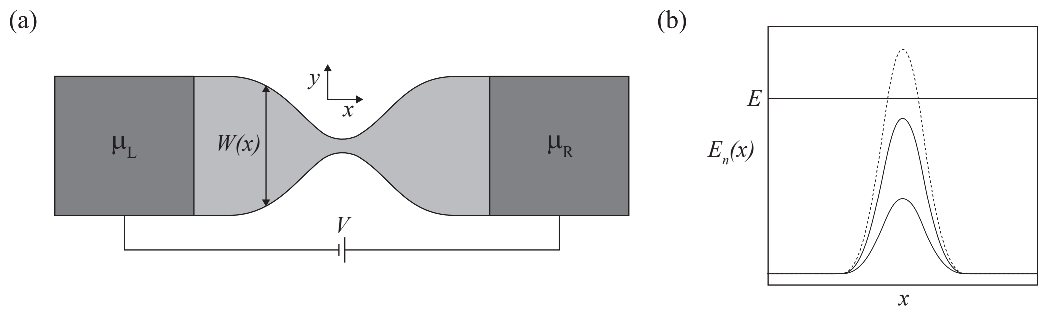

Figure 1.8: (a) A voltage bias is applied between two electron reservoirs (contacts) connected by a conductor in the form of an adiabatic waveguide. (b) Potential barriers for three channels that form at the narrowest part of the waveguide. For an electron of energy E, two of the three channels are open.

Although this calculation gives insight into the conductance quantization phenomenon, the QPC is clearly not a uniform conductor connecting the electron reservoirs. Typically the next level of approximation views the QPC as a adiabatic waveguide, a schematic of which is shown in Fig. 1.8(a). In this case, the width is a function of the x-coordinate and as a result, E_n of Eq. 1.3 becomes x-dependent and takes the following form:

$$E_n(x) = \frac{\pi^2 \hbar^2}{2mW^2(x)} n^2.$$

This energy expression enters the 1D Schrödinger equation as a potential energy [35]. Sketches of $E_n(x)$ in Fig. 1.8(b) show that it acts as a potential barrier for electron motion through the waveguide. Note that this potential still carries the index n and that the maximum height, which occurs at the narrowest part of the constriction, increases with n.

If $W(x)$ is a smoothly varying function (i.e. changes on a length scale that is large relative to $W(x)$ itself), the potential barriers are nearly classical [35]. An electron of energy E, therefore, avoids the barrier if E exceeds the barrier height (open channel) and is reflected otherwise (closed channel).

Moving from the adiabatic waveguide to a potential landscape that more closely approximates that of a QPC is straightforward since the number of open channels and thus the conductance are determined by the narrowest part of the waveguide. Changes to the shape thus do not alter the transport properties provided the narrowest region is maintained. Of course, for the QPCs of the DQD structure, as the gate voltages decrease, the width of this narrowest region decreases. As a result, the heights of the potential barriers increase and one-by-one the channels close, decreasing the conductance in the step-like pattern displayed in Fig. 1.7(a). Note that a modification of the expression for current in Eq. 1.4 is required in the adiabatic waveguide and QPC cases. As alluded to above, the potential barriers are not strictly classical. In a small energy window near the top of a barrier, quantum mechanical tunneling occurs. Adding a transmission coefficient for each channel, $T_n(E)$, to the integrand of Eq. 1.4 is required.[1] It is the energy dependence of $T_n(E)$ that leads to the smooth transitions between the plateaus in the transport data of Fig. 1.7(a). That is, the conductance does not simply snap to a multiple of G_Q. As a result, it is possible to fine tune the conductance of a QPC in order to control tunneling rates and charge detector sensitivity.

1.6 DC-QPC Readout

In a transport measurement of a single quantum dot, each current peak marks a transition between stable charge states of the dot. The charge state can thus be monitored by simply counting these current peaks [36]. Although a similar technique is possible for the DQD case, charge detection with an electric field sensor such as a QPC is usually preferred [24, 37, 38]. Its speed and ability to capture charge state changes that involve the transfer of an electron between the dots make an electric field sensor necessary for control and

[1] Also the lower limit of the integral becomes $-\infty$.

measurement of DQD based qubits.

Fig. 1.9(a) shows an SEM image of the DQD device. The dashed white circles show the approximate positions of the quantum dots and the nearby QPC charge detector is formed by gates Q1 and RS. The QPC resistance, R_{QPC}, plotted as a function of V_{Q1} is shown in Fig. 1.9(b). Between the last plateau (12.9 kΩ) and pinch-off, the slope is large and as a result R_{QPC} is highly sensitive to the electric field produced by gate Q1. For use as a charge detector, the working point (black circle) is chosen where R_{QPC} is maximally sensitive to electric fields, including the electric fields of DQD electrons. Each DQD charge state corresponds to a unique value of R_{QPC} and, for a voltage biased QPC, to a unique value of QPC current, I_{QPC}. A typical QPC voltage bias of 200 μV is created by a 2 V digital-to-analog converter (DAC) output and a 10000:1 voltage divider as shown in (a). The resulting I_{QPC} (3 nA) is measured using the Ithaco (I/V). An electron moving from right to left dot, away from the QPC, reduces the electric field at the QPC and produces an increase in I_{QPC}. Similarly an electron moving from left to right dot reduces I_{QPC}. Adding an electron to either dot reduces I_{QPC} while expelling an electron to the leads increases I_{QPC}. As an example, ejecting an electron from the right dot to the leads typically reduces R_{QPC} by 1 kΩ, increasing I_{QPC} by 50 pA (Section 2.6).

Instead of measuring I_{QPC} and relating it to a particular DQD charge state, sometimes it is preferable to measure transconductance defined as dI_{QPC}/dV_{LP} [37]. Being a derivative of I_{QPC}, transconductance only reveals changes in the DQD charge state. The technique involves applying a DC voltage across the QPC (again 200 μV) and an oscillating voltage (1 $\mathrm{mV_{rms}}$, 17 Hz) to plunger gate LP using a lock-in amplifier and the 100:1 voltage divider shown in the dashed box in Fig. 1.9(a) (the 5:1 voltage divider and a DAC output produce the constant voltage required to deplete underneath the gate). The oscillating electric field of gate LP produces an oscillation in R_{QPC} and thus I_{QPC}. This AC current is turned into a voltage by the Ithaco. The lock-in amplifier measures the 17 Hz component of the Ithaco output and produces a voltage proportional to the transconductance of the QPC.

Fig. 1.9(c) is a gray scale plot of QPC transconductance as a function of side gate voltages V_{RS} and V_{LS}. The black and white lines divide the plot into charge stable regions of the DQD. The details of this charge stability diagram are discussed in Section 1.7. For the purposes of explaining the transconductance measurement, consider the scan taken

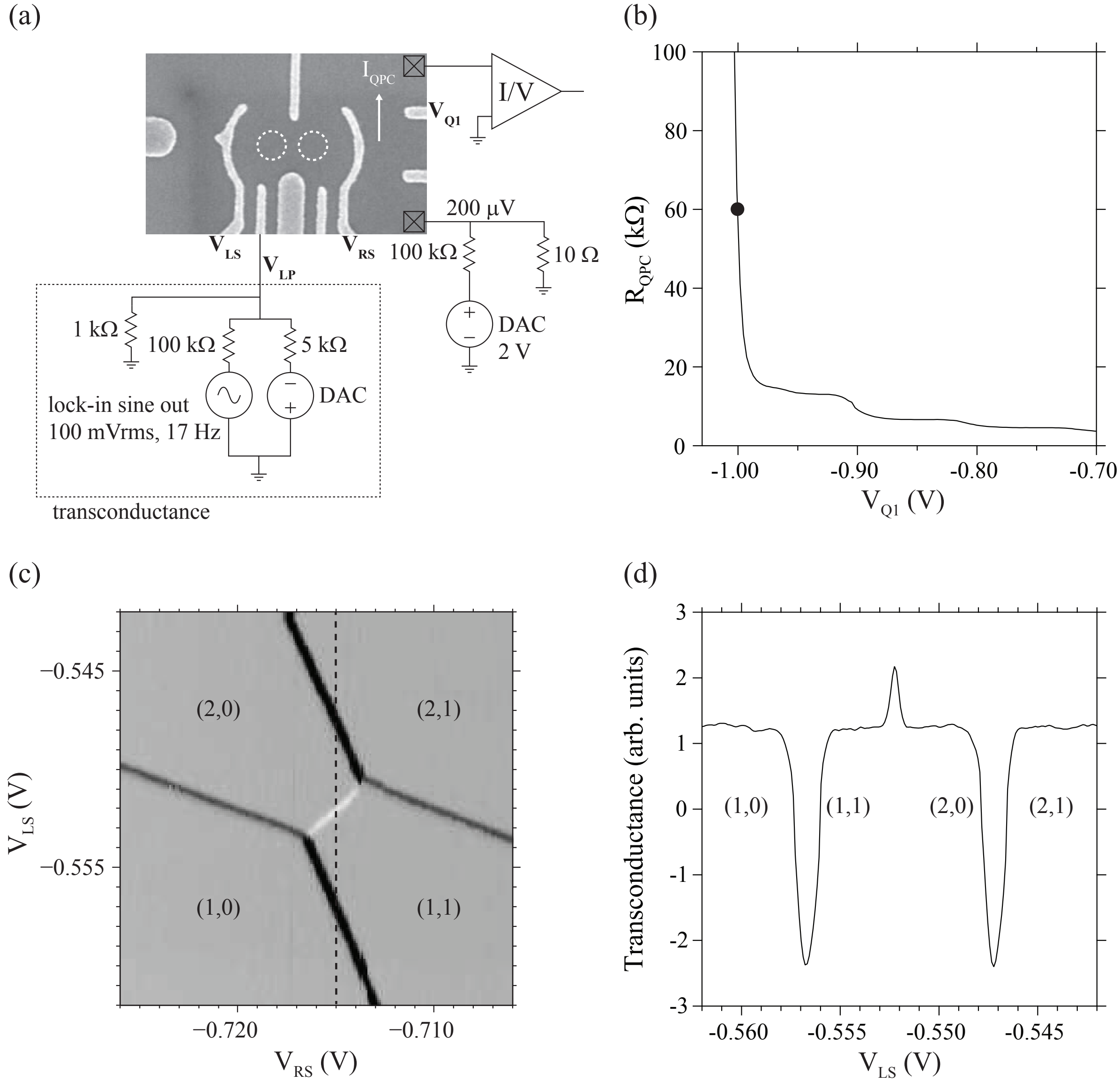

Figure 1.9: (a) DC-QPC readout configuration. The QPC current resulting from V_{QPC} is measured with the Ithaco (I/V). To measure dI_{QPC}/dV_{LP}, a voltage oscillation is applied to gate LP using the circuit in the dashed box. (b) Charge detector resistance as a function of V_{Q1} (black circle at working point). (c) DQD stability diagram acquired using the transconductance technique. (d) Line scan along the vertical dashed line in (c).

along the dashed line and displayed in Fig. 1.9(d). The regions of approximately constant background signal mark stable charge states. In these regions, the QPC sees only the oscillating electric field produced by gate LP. The positive sign of this background signal is explained by the following argument. During the segment of the oscillation when V_{LP} is decreasing ($dV_{LP} < 0$), the electric field at the QPC causes a decrease in I_{QPC} ($dI_{QPC} < 0$). Similarly, when V_{LP} is increasing (d$V_{LP} > 0$), I_{QPC} also increases ($dI_{QPC} > 0$). The transconductance signal, being a ratio of two numbers with the same sign, thus has a positive sign.

The dip in signal observed at $V_{LS} = -0.547$ V indicates a degeneracy of two charge states that differ by one electron, (2,1) and (2,0). At this degeneracy point, an electron oscillates between the right dot and the right lead in response to the oscillating V_{LP}. When V_{LP} is decreasing, I_{QPC} changes for two reasons. The effect of the gate alone is to reduce I_{QPC}. The electric field of the gate, however, also ejects an electron from the DQD which increases I_{QPC}. A similar argument can be made for an increasing V_{LP}. In both cases, the electric fields of the gate and the moving electron are 180° out of phase with each other at the QPC. The component of I_{QPC} in phase with the V_{LP} oscillation is therefore reduced by the electron motion and the transconductance signal decreases. If the electric field produced by the moving electron is larger than that of the gate, the transconductance signal can actually swing negative as shown in the figure.

The peak in signal observed at $V_{LS} = -0.552$ V indicates a degeneracy of two charge states that possess the same number of electrons, (1,1) and (2,0). The oscillating V_{LP} causes an electron to move between the two dots. When V_{LP} decreases, the electron moves from left dot to right dot and towards the QPC. The electron now being closer to the QPC results in a larger decrease in I_{QPC} than would be possible with the gate alone. When V_{LP} increases, the electron moves back to the left dot, away from the QPC. In this case, the electric fields produced by the gate and the electron both result in an increase in I_{QPC}. Clearly the electron motion enhances the amplitude of the I_{QPC} oscillation and thus leads to an increase in transconductance signal.

1.7 Double Quantum Dot Stability Diagram

Fig. 1.10(a) shows a DQD circuit superimposed on an SEM image of the device. Each dot is tunnel coupled to a lead and strongly capacitively coupled to a side gate, LS or RS. The two quantum dots interact with each other through a tunnel barrier controlled with gate C. The gates C, T, LP, and RP are all held at constant voltages while the side gate voltages, V_{LS} and V_{RS}, are made progressively more negative, expelling electrons to the leads until both quantum dots are empty. Measuring the QPC transconductance during this process produces the charge stability diagram of Fig. 1.10(b). The transconductance extrema form boundaries between equilibrium charges states defined by N_1 electrons in the left dot and N_2 electrons in the right dot. These charge stable regions are labeled (N_1, N_2).

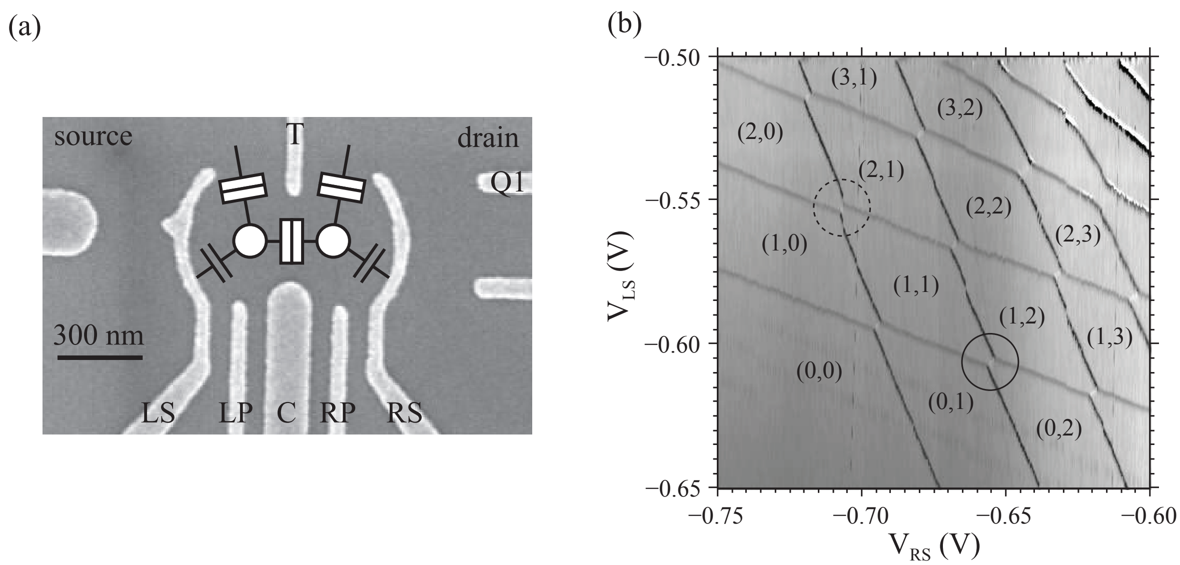

Figure 1.10: (a) Schematic DQD circuit shown on an SEM image of the device. Each quantum dot (white circle) is tunnel coupled to a lead and capacitively coupled to the gates. The dots are also tunnel coupled to each other. (b) Grey scale plot of QPC transconductance as a function of the side gate voltages V_{LS} and V_{RS}. The QPC charge detector is formed between gates Q1 and RS.

In analogy with the Coulomb blockade analysis of Section 1.4, the boundaries are discussed with reference to the electrochemical potentials $\mu_1(N_1, N_2)$ and $\mu_2(N_1, N_2)$ defined by the following expressions:

$$\mu_1(N_1, N_2) = U(N_1, N_2) - U(N_1 - 1, N_2)$$
$$\mu_2(N_1, N_2) = U(N_1, N_2) - U(N_1, N_2 - 1),$$

where $U(N_1, N_2)$ is the total energy of the DQD in charge state (N_1, N_2). The electrochemical potential $\mu_{1(2)}(N_1, N_2)$ is the energy required to add the $N_{1(2)}^{th}$ electron to an $N_{1(2)} - 1$ electron left (right) dot with $N_{2(1)}$ electrons on the right (left) dot [31].

A zoom-in of Fig. 1.10(b) (dashed circle) is displayed in Fig. 1.11(a). Energy level diagrams showing electrochemical potentials for the DQD are shown in (b). Defining the zero of energy such that the chemical potentials of the source and drain leads are equal to zero ($\mu_S = 0 = \mu_D$), the boundary lines separating charge states that differ by one electron correspond to either $\mu_1 = 0$ ($\square$; nearly horizontal) or $\mu_2 = 0$ ($\diamond$; nearly vertical). The related reductions in QPC transconductance signal are plotted as black and dark gray pixels to form the negatively sloped lines known as addition lines. The capacitive coupling of the left (right) side gate to the right (left) dot, not included in the simple circuit of Fig. 1.10(a), determines the slope of the near vertical (horizontal) lines.

Where two addition lines meet, the electrochemical potentials of both leads and both quantum dots are equal ($\triangle$,$\triangledown$). These points are called triple points because they mark a degeneracy of three charge states. With a small voltage bias applied across the DQD, electron transport from left to right lead via the cycle (1,0) $\rightarrow$ (2,0) $\rightarrow$ (1,1) $\rightarrow$ (1,0) occurs at $\triangle$. Hole transport can proceed from right to left via the cycle (2,1) $\rightarrow$ (2,0) $\rightarrow$ (1,1) $\rightarrow$ (2,1) at $\triangledown$. The positively sloped white line connecting the triple points is called a charge transfer line. It marks a degeneracy between two charge states that possess an equal number of electrons, in this case (2,0) and (1,1). Moving along the charge transfer line from $\triangle$ to $\triangledown$, $\mu_1(2,0)$ and $\mu_2(1,1)$ stay in resonance but move further below the energy of the leads. Perpendicular to this line runs an axis labeled ε, known as the detuning axis. The charge transfer line intersects this axis at $\varepsilon = 0$. Moving along the ε-axis, the energy difference between the electrochemical potentials $\mu_1(2,0)$ and $\mu_2(1,1)$ changes while their average energy remains constant ($\circ$, $\bullet$).

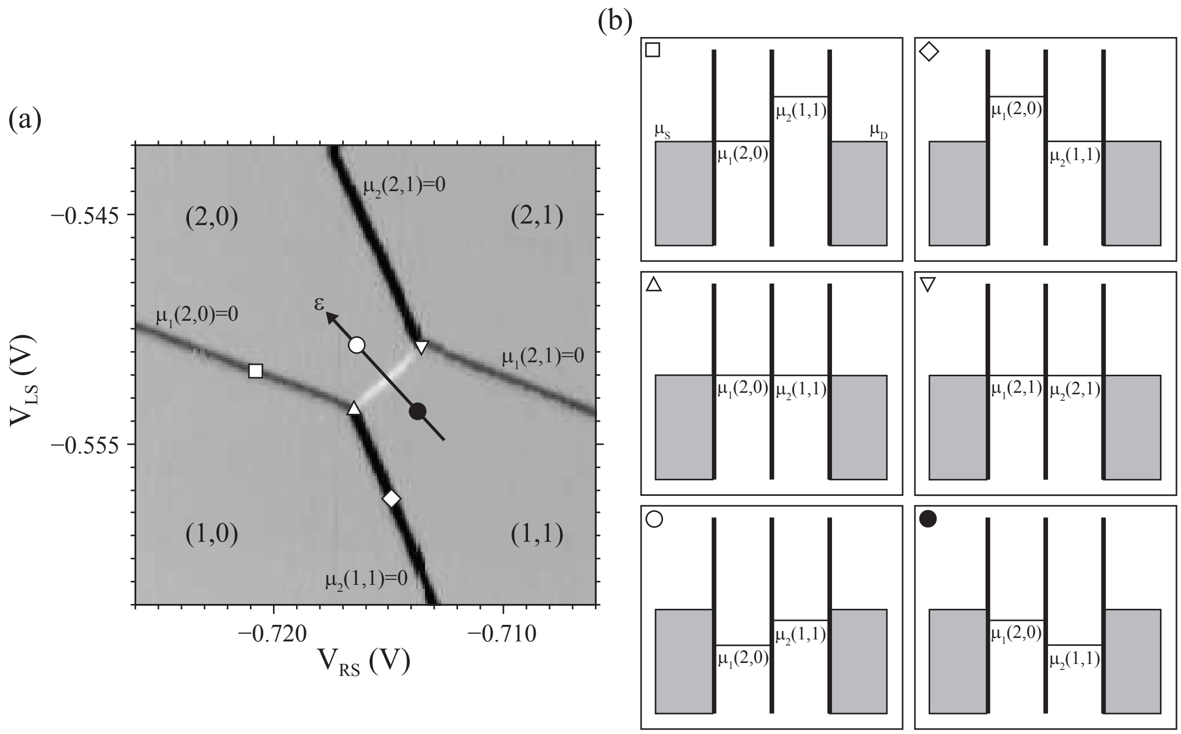

Figure 1.11: (a) DQD stability diagram in the few electron regime. Along the near horizontal dark lines, $\mu_1 = 0$ (□) while along the near vertical dark lines $\mu_2 = 0$ (◇). At the triple points, electron transport from left to right (△) or hole transport from right to left (▽) is possible. The detuning axis is labeled ε. For points on this axis the charge states (2,0) and (1,1) have the same average energy (○,●). (b) Energy level diagrams corresponding to the points labeled in (a).

1.7.1 Bias Triangles

By applying a voltage bias of several hundred microvolts to the source lead while keeping the drain lead grounded, the stability diagram undergoes a significant change in the vicinity of the triple points. A bias of $V_{DQD} = -500\ \mu$V increases $\mu_S = -|e|V_{DQD}$ and results in the stability diagram of Fig. 1.12(a). The nearly vertical addition lines ($\mu_2 = 0$) are in approximately the same positions as in Fig. 1.11(a) but the nearly horizontal addition lines ($\mu_1 = -|e|V_{DQD}$) have moved to more negative values of V_{LS}. This indicates that, relative to the zero bias case, the electrochemical potential of the left dot must be moved upwards in energy by decreasing V_{LS} in order to establish a resonance condition with the source lead. The resulting movement of addition lines creates triangular shaped regions in the stability diagram called bias triangles. The boundaries of these triangles are determined by the inequalities $-|e|V_{DQD} = \mu_S \geq \mu_1$, $\mu_1 \geq \mu_2$, and $\mu_2 \geq \mu_D = 0$.

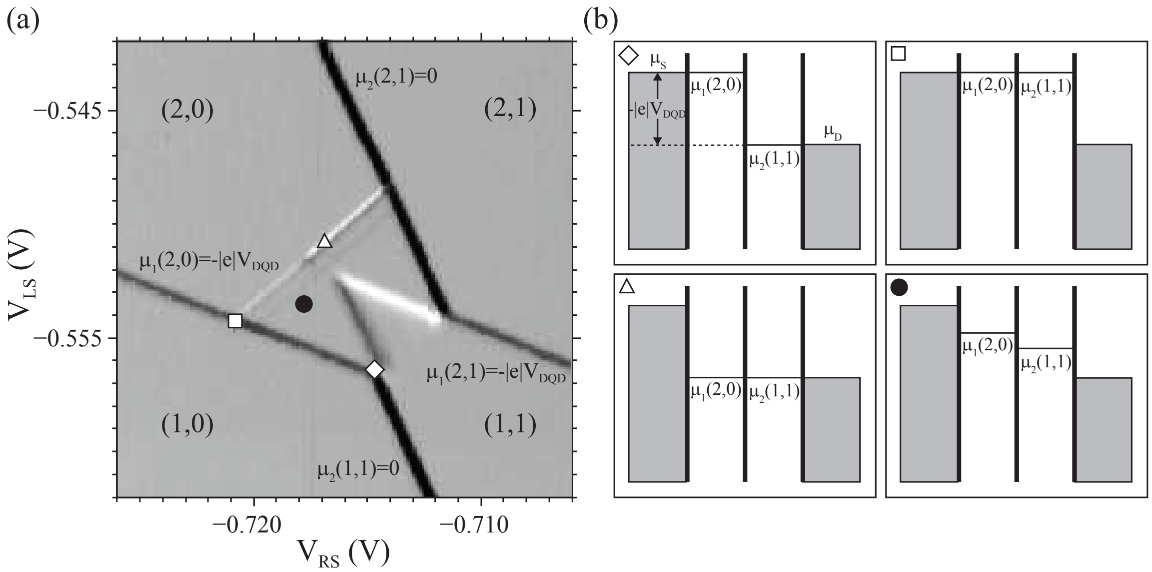

Figure 1.12: (a) DQD stability diagram for the $V_{DQD} = -500$ μV case. With the increase in source lead energy, the near horizontal lines move to more negative values of V_{LS} relative to the zero bias case of Fig. 1.11. This line movement creates electron (lower left) and hole (upper right) bias triangles. (b) Energy level diagrams corresponding to the labeled points in (a).

Electrochemical potential level diagrams at the vertices and within the lower left triangle are shown in Fig. 1.12(b). At point ◇, two addition lines intersect and the dots are in resonance with their respective leads. Moving along the left dot addition line, the energy of the right dot increases (by decreasing V_{RS}) and a resonance involving both dots and the source lead occurs at □. Moving along the base of the triangle (charge transfer line), the dots stay in resonance and together reach the drain at △. At the point labeled ●, the dots are detuned from each other and possess an average energy approximately halfway between the leads. The downward movement in energy from left to right in all of the diagrams indicates that single electron transport is possible within and on the boundaries of the triangle. Due to this transport, the charge state within the bias triangle is an average of the three involved charge states (1,0), (2,0), and (1,1). A similar analysis for the upper right triangle reveals single hole transport within and on its boundaries.

Note that at $\triangle$, the energy configuration of the dots and drain lead are identical to the electron triple point of the zero bias case shown in Fig. 1.11(a) (also marked $\triangle$). The two points are not at the same position in the stability diagram (i.e. different V_{LS} coordinates), however, because the source lead acts as an in-plane gate. That is, applying -500 μV to the source lead also increases the energy of the left dot. An increase in V_{LS} is thus required to lower the energy of the dot and reestablish the resonance condition.

1.7.2 Plunger Gate Lever Arms

To compare data with theory sometimes requires converting a gate voltage axis to energy units. In Section 2.4, such a procedure is required to measure the electron temperature of the device. Since most manipulations of the DQD are performed using plunger gates, the conversion factors relating volts to electron volts, called lever arms, are acquired for the plunger gates in this section. These lever arms can be extracted from bias triangle data. Two stability diagrams acquired at finite bias are displayed in Fig. 1.13. Applying -500 μV to the left lead creates the bias triangles of Fig. 1.13(a) and a voltage of -350 μV results in the bias triangles displayed in (b). The gate voltage ranges in the two diagrams are similar because the side gates (LS and RS) are used to move between the two regions, marked by circles on Fig. 1.10(b). Begin by deriving expressions for the lever arms in terms of parameters that are easily extracted from the finite bias data. The discussion closely follows the development presented in Ref. [39], using similar notation. The coordinate transformations that connect changes in left and right dot energies, $d\mu_L$ and $d\mu_R$, to changes in left and right plunger gate voltages, dV_{LP} and dV_{RP}, are given by

$$\begin{aligned} d\mu_L &= -\alpha_{LP}^{L} dV_{LP} - \alpha_{RP}^{L} dV_{RP} \\ d\mu_R &= -\alpha_{LP}^{R} dV_{LP} - \alpha_{RP}^{R} dV_{RP}, \end{aligned} \tag{1.5}$$

where the coefficients are the lever arms.

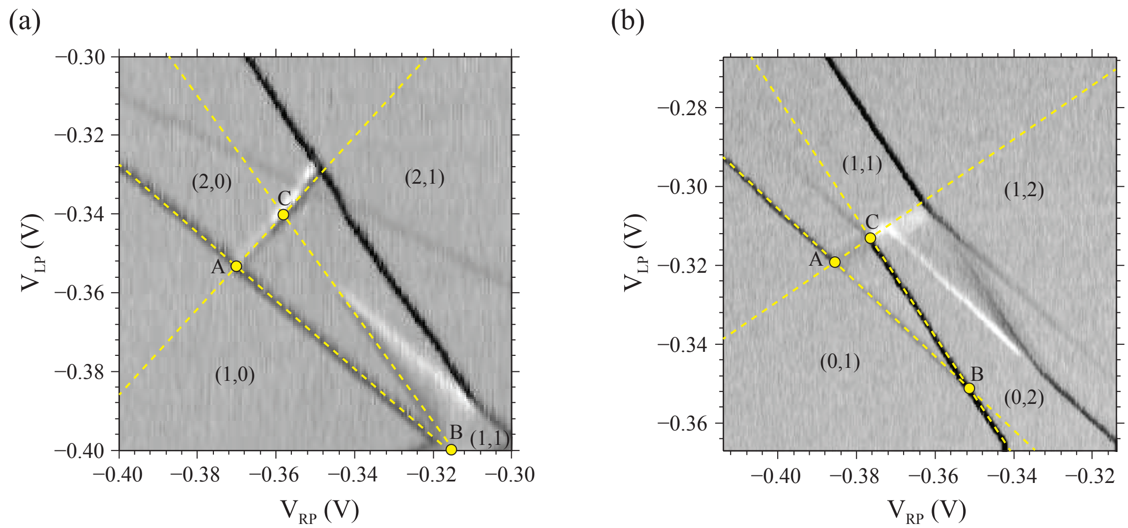

Figure 1.13: (a) Bias triangles near the (1,1)↔(2,0) region created by applying a −500 μV bias to the left lead. (b) Bias triangles near the (1,1)↔(0,2) region resulting from a −350 μV bias on the left lead.

The charge transfer (or charge recombination) line (AC) and the left (AB) and right (BC) addition lines are defined by the conditions $d\mu_L = d\mu_R$, $d\mu_L = 0$, and $d\mu_R = 0$ respectively. The following expressions for the slopes of these lines s_{cr}, s_L, and s_R ($s = dV_{LP}/dV_{RP}$), are derived by combining these definitions with Eq. 1.5:

$$
\begin{aligned}
s_L &= -\frac{\alpha_{RP}^L}{\alpha_{LP}^L} \\
s_R &= -\frac{\alpha_{RP}^R}{\alpha_{LP}^R} \\
s_{cr} &= \frac{\alpha_{RP}^L - \alpha_{RP}^R}{\alpha_{LP}^R - \alpha_{LP}^L}
\end{aligned}
\tag{1.6}
$$

Note that in moving from B to C, the right dot energy does not change but the left dot energy changes by $-|eV_{DQD}|$ ($\diamond \rightarrow \triangle$ in Fig. 1.12). Calling ΔV_{LP} the required change in LP for the transition B → C , substitute $dV_{LP} = \Delta V_{LP}$, $d\mu_R = 0$, and $d\mu_L = -|eV_{DQD}|$

into Eq. 1.5 and eliminate dV_{RP} to produce the expression for α_{LP}^{L} shown below. The other three expressions are derived by rearranging terms in Eq. 1.6.

$$\begin{aligned}
\alpha_{LP}^{L} &= \frac{|eV_{DQD}|}{\Delta V_{LP}} \frac{s_R}{s_R - s_L} \\
\alpha_{LP}^{R} &= \frac{s_{cr} - s_L}{s_{cr} - s_R} \alpha_{LP}^{L} \\
\alpha_{RP}^{L} &= -s_L \alpha_{LP}^{L} \\
\alpha_{RP}^{R} &= -s_R \alpha_{LP}^{R}
\end{aligned}$$

From Fig. 1.13, ΔV_{LP}, s_{cr}, s_L, and s_R are extracted for the two cases. These values and the resulting lever arms are summarized in Table 1.1.

Table 1.1: Summary of charging line slopes and plunger gate lever arms.

	Fig. 1.13(a)	Fig. 1.13(b)
V_{DQD} (μV)	-500	-350
s_R	-1.56	-1.52
s_L	-0.95	-0.94
s_{cr}	1.05	0.68
ΔV_{LP} (mV)	60	38
α_{LP}^{L} (meV/V)	21.3	24.1
α_{RP}^{L} (meV/V)	20.2	22.7
α_{LP}^{R} (meV/V)	16.3	17.7
α_{RP}^{R} (meV/V)	25.4	26.9

1.8 Spin Blockade for a Double Quantum Dot

Electrical transport through a DQD is limited to the bias triangles of the charge stability diagram. In some regimes of the device, however, strong suppression of this single electron current is observed for one polarity of voltage bias [25, 40]. This current rectification phenomenon, known as spin (or Pauli) blockade, results from the conservation of electron spin in interdot tunneling processes and the Pauli exclusion principle.

Spin blockade is observed in several regions of the stability diagram but because of its importance in spin-qubit applications, focus is given to the two-electron regime involving charge states (1,1) and (0,2) [40]. The ground state for the (0,2) charge state is a spin singlet, denoted S(0,2). The excited state triplet T(0,2) is separated from this singlet by an energy, $E_{ST} \approx 600$ μeV [40]. This singlet-triplet splitting arises because one of the electrons in the T(0,2) state must occupy a higher orbital in order for the total two-electron wave function to be antisymmetric [14]. With the electrons separated by the central tunneling barrier, the singlet, S(1,1), and triplet, T(1,1), are nearly degenerate. The energy level diagrams for positive and negative voltage bias are shown in Fig.1.14(b) and (d) respectively. These diagrams are of the standard sort one finds in the literature related to transport involving electron spin states. One electron is always present on the right dot. The levels are labeled S or T depending on whether the addition of an electron to the DQD will form a singlet or a triplet spin state. For the positive bias case of (b), the left lead has a lower energy ($-|e|V_{DQD}$) than the grounded right lead and transport from right to left proceeds by the cycle (0,1) → S(0,2) → S(1,1) → (0,1). Note that this process conserves spin in the transition S(0,2) → S(1,1). For the negative bias case of (d), the left lead has a higher energy than the right lead and transport from left to right can occur via the process (0,1) → S(1,1) → S(0,2) → (0,1), with the step S(1,1) → S(0,2) conserving spin. In this negative bias case, however, an electron can enter the left dot from the left lead to produce T(1,1) instead of S(1,1) in the first step. The transition T(1,1) → S(0,2) does not conserve spin and the transition T(1,1) → T(0,2) cannot occur because T(0,2) is inaccessible due to E_{ST}. Therefore once T(1,1) is occupied, transport is stopped until some mechanism causes the transition T(1,1) → S(1,1) followed by tunneling to S(0,2). Such a process, requiring a spin-flip, can occur via an interaction with the Ga and As spin-3/2 nuclei of the semiconductor heterostructure (Section 4.3). The time constant, T_1, for such a process is on the order of 100 μs leading to a suppression of the single electron current [41].

Examples of charge detection measurements that reveal evidence of spin blockade in a DQD are shown in Fig.1.14(a) and (c). Transconductance of the QPC charge detector is measured to acquire stability diagrams for ± 500 μV bias applied to the left lead with the right lead grounded. A magnetic field of 80 mT is applied in the plane of the 2DEG during the measurements. Consider the resulting electron bias triangle in the $+500$ μV case of (a) that is surrounded by the charge states (0,1), (0,2), and (1,1) (lower left triangle in the solid circle). Transconductance signals forming the three sides indicate that the charge state within the triangle is not (0,1), (0,2) or (1,1). In fact, because of the current flow, the occupancy of the DQD is an average of these three states. Now note the effect of inverting the bias (-500 μV) shown in (c) (dashed circle). A triangle is not observed in this case. The third side that would form the triangle and separate it from the (1,1) region is missing (arrows). This indicates that the time-averaged occupancy is heavily weighted towards the (1,1) state as expected in this spin blockade regime. A similar argument is made for the hole triangle (upper right triangle within the solid and dashed circles) and for the finite bias triangles surrounded by regions (1,0), (2,0), (1,1), and (2,1). Spin blockade (disappearance of a side) is observed for $+500$ μV bias in the latter case as expected. Note that spin blockade is not observed for the finite bias triangles in the (2,1)$\leftrightarrow$(1,2) region (i.e. triangles observed for both bias polarities). This is consistent with transport measurements made by Johnson et al. and a simple theory of Pauli filling of orbital levels which predicts spin blockade for cases involving an even number of electrons and free flowing current in both directions for cases involving an odd number of electrons [40]. There are no triangles in the (1,0)$\leftrightarrow$(0,1) case. This results from the presumably small interdot coupling which forces the system to spend most of its time in (1,0) for the negative bias case and in (0,1) for the positive bias case, again consistent with the measurements reported in Ref. [40].

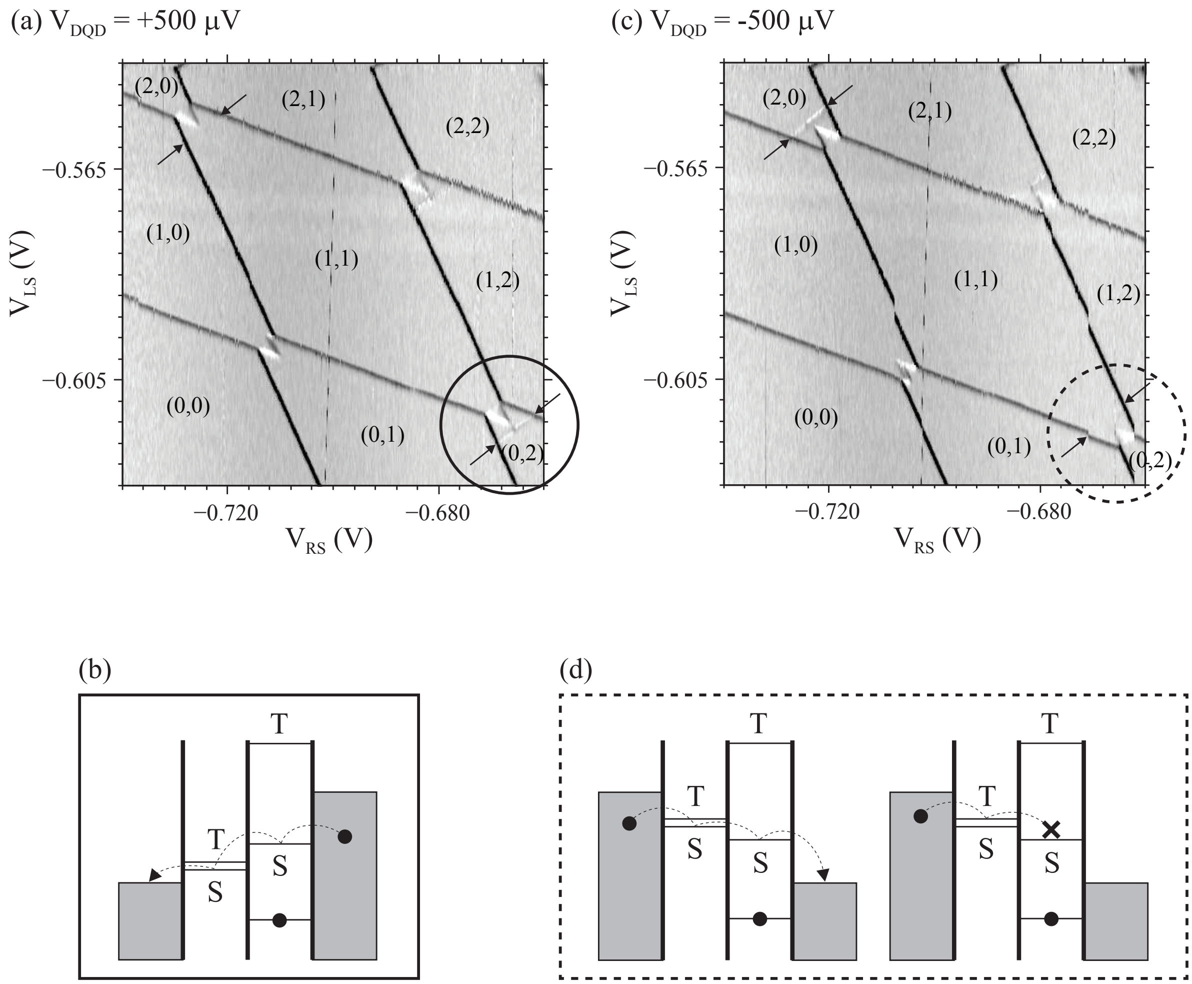

Figure 1.14: (a) Stability diagram for the +500 μV case (in-plane B = 80 mT). (b) Energy level diagram for the electron bias triangle (lower left) located within the solid circle in (a). (c) Stability diagram for the -500 μV case. (d) Energy level diagrams corresponding to the electron bias 'triangle' located within the dashed circle in (c).

1.9 Conclusion

Several simple but necessary quantum dot experiments have been performed. Coulomb blockade of a quantum dot and conductance quantization of a QPC has been observed. Using a QPC based charge detector, control of the charge state of a DQD has been demonstrated and a stability diagram formed. Finite bias measurements in the few electron regime of the DQD reveal the spin blockade phenomenon, necessary for the qubit state readout described in Chapter 4.

Chapter 2

Measurement System

2.1 Introduction

Details related to the development of a measurement system for studying NRC quantum dot devices on a dilution refrigerator are provided in this chapter. The system is centered on the NRC developed sample holder, allowing devices to be easily measured in both the NRC and UW labs. This chapter begins with a discussion of the cryostat shielding and electrical lead filtering necessary to provide a low noise environment for the device. The microwave frequency connections to the plunger gates required for spin-qubit manipulation are also discussed. Finally an analysis of the DC-QPC readout is provided at the end of the chapter.

2.2 Shielding, Grounding, and Wiring

Several types of metal shields help to reduce the coupling of the device to electromagnetic noise in the lab. The Oxford 600 dilution refrigerator is mounted inside a screen room. The walls and ceiling of the room are galvanized steel and the floor is copper. The few pieces of electronics located inside the screen room are battery powered. These include the Ithaco used for transport and charge detection measurements and the radio-frequency (rf) amplifiers used in the RF-QPC readout (Chapter 3). Signals pass into and out of the screen room via SMA bulkheads and 25 pin D-subminiature, low-pass pi filters (Spectrum Control 700 series, 800 kHz cutoff) mounted in a removable copper plate in one of the screen room walls. The magnet power is similarly filtered at this plate. Surrounding the fridge dewar is a μ-metal shield responsible for attenuating low frequency electromagnetic signals, in particular 60 Hz noise. It also allows the Nb inductor of the RF-QPC and the NbTi superconducting magnet to be cooled in a low magnetic field environment. A copper radiation shield at the base temperature stage of the fridge surrounds the device [Fig. 2.1(a)]. With several microwave lines running into the shield for readout and qubit manipulation, there is concern about exciting resonances of this cylindrical cavity. In an attempt to absorb microwave energy within the shield, its inner surface is coated with a mixture 2850FT black epoxy, charcoal, SiO_2 powder, and copper powder.

The power for the measurement electronics is filtered by a 1800 W Tripp-Lite isolation transformer and a filter bank. The ground is not broken at the isolation transformer meaning that the measurement system ground is the building ground. A copper braid runs from the grounding post of the isolation transformer to the screen room where it is attached to the copper electrical feedthrough panel. Inside the screen room, two copper braids run from this panel, along the still pipe, to the top of the fridge. One is clamped to the fridge and the other is attached to a central grounding copper plate. This plate is the grounding point for the battery powered Ithaco and the voltage dividers used for transport and charge detection measurements (Section 1.6).

DACs (Iotech, model DAC488HR/4) controlled by a LabVIEW program apply voltages to the gates and ohmic contacts of the DQD device. Communication between the data acquisition computer and the measurement electronics, including the DACs, is accomplished using an optical isolator. Each DAC produces four floating voltages on 9-pin D-subminiature connectors. The 12 floating voltage lines (4×3 DACs) enter the screen room via the feedthrough panel and run in 25-pin D-subminiature cables to the top of the fridge where they enter a BNC breakout box (non-isolated connectors). This box is connected to the central grounding copper plate. As a result, the DAC voltages become ground referenced along with the dividers and the Ithaco at this location.

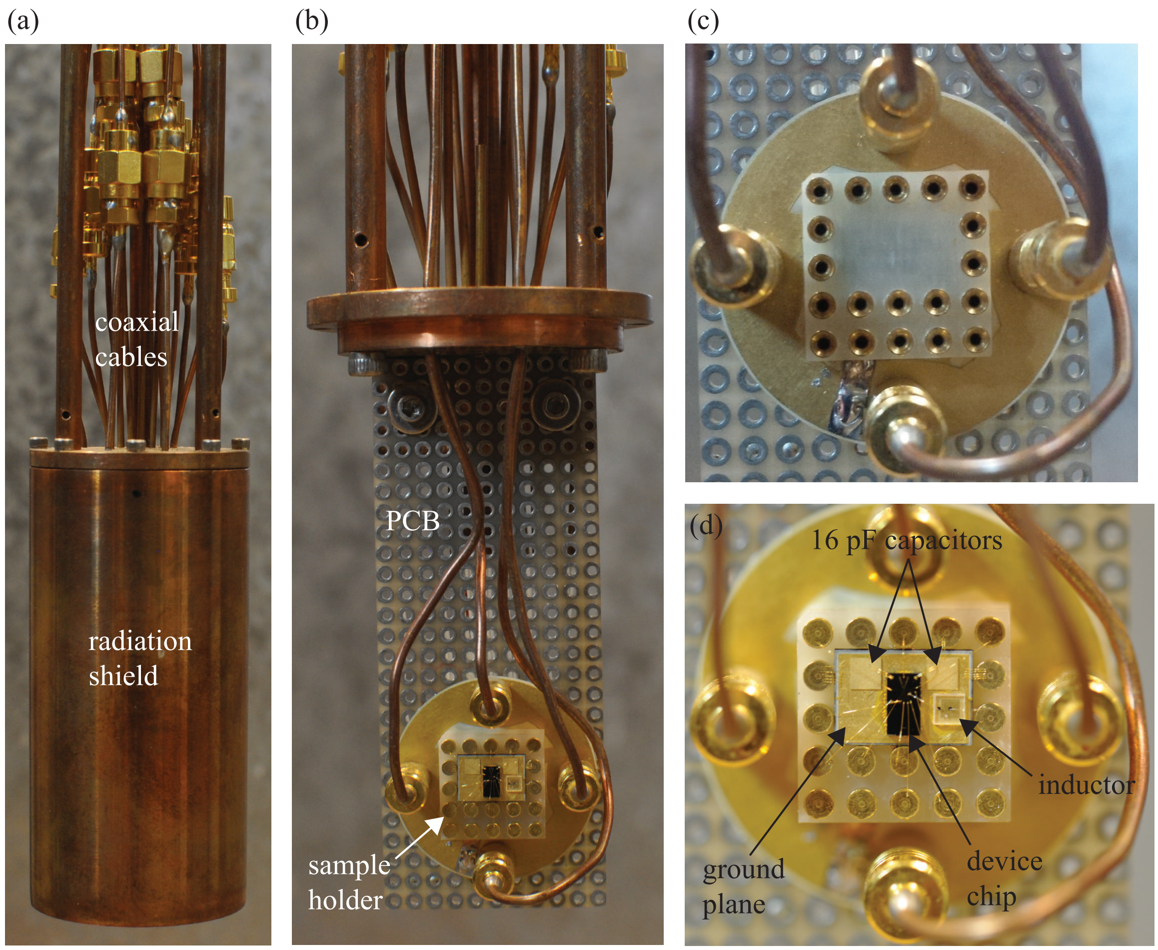

Figure 2.1: (a) Base temperature radiation shield surrounding the device and copper coaxial cables carrying both microwave and low frequency signals. (b) PCB mounted to the lid of the radiation shield and the sample holder mounted to the PCB. (c) 19-pin socket, 4 MCX connectors (and mating coaxial cables), and gold foil covered ceramic board of the NRC sample holder. (d) Quantum dot device chip glued using GE varnish to the gold ground plane of a 19-pin mating connector.

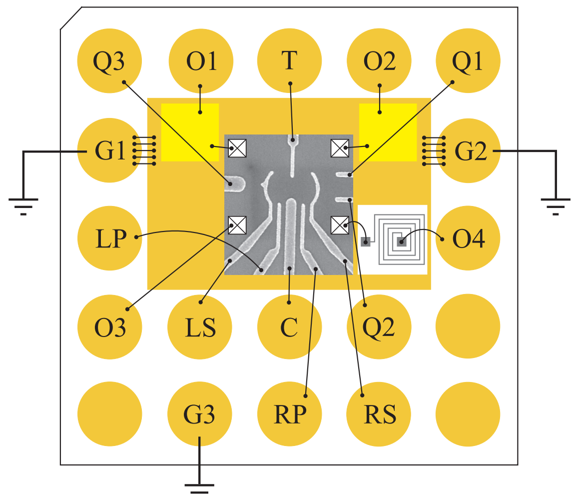

Figure 2.2: Wire bonding configuration for the DQD device showing the pin labeling convention.

Low thermal conductivity wiring (CuNi clad, NbTi below the 1 K pot) runs from a hermetic feedthrough at the top of the dilution refrigerator to the mixing chamber where the DQD device is mounted. This low frequency wiring runs as a ribbon down the fridge. It is heat sunk to the 4.2 K plate, 1 K pot, still, heat exchangers, and mixing chamber by wrapping it around copper posts and fixing it in place with GE varnish. At the mixing chamber, the ribbon is split apart and each wire is connected to the input of an electrical filter. These combination RC, LC, and copper powder filters are described in Section 2.3. To provide shielding from electromagnetic noise, each filtered lead is connected to the center conductor of a UT-47 copper coax. The collection of coaxial cables run down into the tail region of the fridge where they are soldered to the lid of the base temperature radiation shield as shown in Fig. 2.1(a). The sample holder, developed by the NRC group, consists of several parts. The 19-pin socket and high frequency compatible, ceramic board are mounted to a printed circuit board (PCB) as shown in Fig. 2.1(c). This PCB is shown attached to the lid of the radiation shield in Fig. 2.1(b). On the backside of the PCB, the filtered low frequency lines are soldered to the pins of the socket. Fig. 2.1(d) displays a mating 19-pin connector plugged into the socket. A gold ground plane, necessary for transmitting microwave signals to the device chip, and the device chip itself are fixed in place using GE varnish. The gates and most of the ohmic contacts of the device are connected to the surrounding gold pins with 25 μm diameter gold wire bonds. Aluminum wire is used for the RF-QPC ohmic. The wire bonding configuration is shown in Fig. 2.2. The two ground pins in the second to top row (G1 and G2) are wire bonded to the ground plane using gold wire. Using silver epoxy, the corresponding pins on the socket are connected to copper wires which are pressed against the lid of the radiation shield using a stainless steel screw. This high thermal conductivity path from the ground plane to the radiation shield is the prime means of cooling the ground plane and thus the device. Pins T, LP, RP, and O4 are connected to MCX connectors mounted to the ceramic board. Coaxial cables running down the fridge plug into these ports, allowing microwave frequency signals to be transmitted to the device. Pins LP and RP are used for the high bandwidth gates (Section 2.5) and pin O4 is used for the RF-QPC readout (Chapter 3). The Nb inductor (fixed in place using GE varnish) and the low temperature compatible, 16 pF capacitors (fixed in place with silver epoxy) are part of the RF-QPC readout [Fig. 2.1(d)].

2.3 Low-frequency Filtering

Electromagnetic noise produced by control and measurement electronics and resistive elements at higher temperature stages is transmitted to the device via the electrical leads. This noise could lift the Coulomb blockade condition via photon-assisted tunneling, heat the electrons of the 2DEG smearing out features in the stability diagram, and lead to qubit decoherence. In an attempt to avoid these deleterious effects on the device, the electrical leads are heavily filtered. Since filtering is required in a large bandwidth that no single type of filter can cover alone, traditional RC and LC filters covering Hz to GHz are combined with dissipative filters covering from hundreds of MHz to tens of GHz and beyond.

There are several types of dissipative filters, the most common of which are lossy transmission lines and metal powder filters. Attenuation of noise in both cases relies on energy loss via eddy current dissipation in an electrically resistive metal. As frequency increases, the skin depth of the metal, $\delta \propto \omega^{-1/2}$, decreases, effectively increasing the resistance of the metal and therefore increasing dissipation. Introduced to the low temperature device community by Zorin in 1995, Thermocoax is now a widely used lossy transmission line [42]. The 0.5 mm diameter cable is composed of a NiCr core (50 Ω/m) and a stainless steel or Inconel sheath separated by compacted MgO powder. Bladh et al. report attenuation measurements of Thermocoax at 4.2 K. For the stainless steel sheath version, they find that attenuation (in dB) has the $\omega^{1/2}$ dependence predicted by Zorin and an attenuation of approximately 100 dB/m at 8 GHz [43]. Fukushima et al. show that the Inconel version has a frequency dependence that is stronger than $\omega^{1/2}$ at 4.2 K. They report an attenuation of greater than 100 dB/m above 1 GHz at any temperature [44]. Thermocoax thus provides significant noise attenuation for a cable length that could fit fairly easily on a dilution refrigerator. The main disadvantages of Thermocoax are the difficulty soldering to the NiCr and stainless steel conductors and the water absorbing properties of the MgO that lead to leakage currents to ground [44]. The other popular dissipative filter is the metal powder type invented in 1987 by Martinis for Josephson junction experiments [45]. A low frequency (i.e. not 50 Ω) version consists of a signal carrying wire wrapped in a solenoid geometry and surrounded by fine grains of a metal powder. The attenuation of this low-pass filter comes from the resistance of the solenoid wire and the dissipation of eddy currents induced in the grains of the metal powder. The large effective surface area of the powder produces substantial skin-effect damping.

Copper powder filters with manganin solenoids are chosen for the quantum dot measurement system. These filters are shown surrounding the mixing chamber of the dilution refrigerator in Fig. 2.3(c). Each filter consists of a copper shield inside of which is placed a manganin solenoid and the copper powder. A completed shield is shown leftmost in Fig. 2.3(a). To create a shield, a 9/32 inch diameter hole is drilled through a $1/2 \times 1/2$ inch, $3\frac{7}{8}$ inch long, oxygen free copper block. The hole is threaded using a 5/16-24 tap. The block is then turned down to a cylindrical geometry over most of its length (0.39 inch diameter). Four 2-56 threaded holes are drilled and tapped in both ends for mounting SMA connectors. The cylindrical section is then lead plated to provide magnetic shielding for the solenoid. The next step involves making a rod of copper powder and epoxy, an example of which is shown rightmost in Fig. 2.3(a). Copper powder with particles of less than 63 μm diameter (EMD, part no. CX1925-4) is combined with Emerson and Cuming Stycast

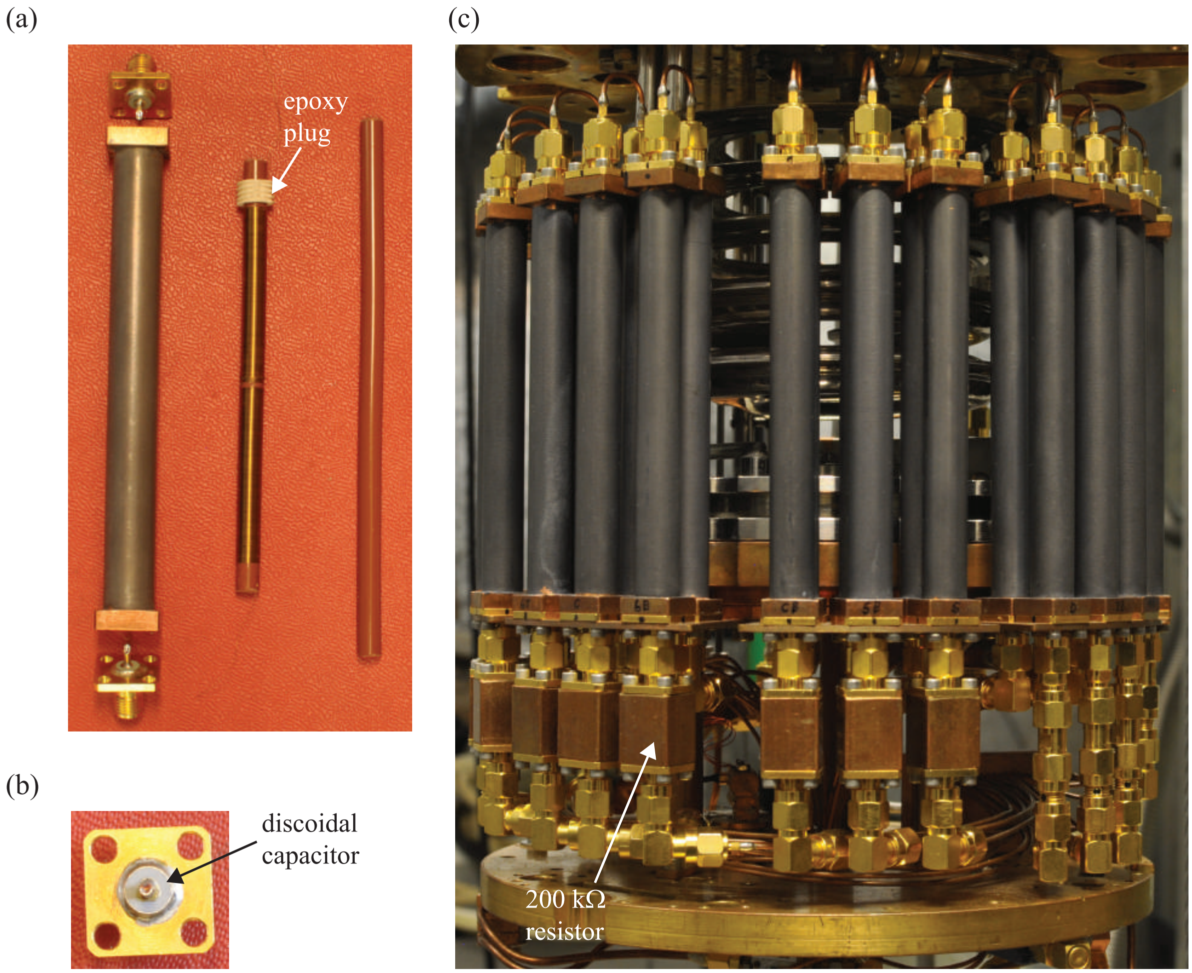

Figure 2.3: (a) Components of the copper powder filter: copper powder rod (right), solenoid wrapped on rod (center), lead plated copper shell and SMA connectors (left). (b) 12 nF discoidal capacitor soldered to an SMA connector. (c) Copper powder filters (and 200 kΩ resistors) mounted around the mixing chamber of the dilution refrigerator.

1266 in a 50/50 by weight mixture. In an attempt to remove air introduced during the stirring process, the mixture is placed in a desiccator and pumped on for approximately two minutes. Using a mechanical pump the mixture is then pulled into 3/16 inch inner diameter flexible tubing (Tygon). After a curing time of approximately 24 hours, the tubing is easily peeled away, leaving the solid powder/epoxy rod. Using a solenoid winding machine, enamel coated manganin wire (0.0025 inch diameter, 49.13 Ω/ft) is wound around the rod as shown in the center of Fig. 2.3(a). The solenoid consists of 900 turns, half of which is counter-wound to reduce the coupling of magnetic field noise into the system [43]. There is no separation between the turns [46] and the total resistance of this coil is approximately 2 kΩ. To facilitate mounting the rod inside the copper shield, an epoxy plug is super-glued to the rod as shown in Fig. 2.3(a). This plug has a 5/16-24 thread on its outside and a 3/16 inch diameter hole down its center to accommodate the powder/epoxy rod. The raw material for the epoxy plug is purchased from McMaster-Carr. A slot for a flat-head screwdriver is made in the end of the rod using a Dremel tool. With the threaded epoxy plug and the threaded hole in the copper block having the same pitch, the rod/solenoid/plug assembly is easily inserted into the copper block. A small amount of five minute epoxy is used to fix the plug/rod in place and seal any leaks before more powder/epoxy mixture is poured into the other end of the block filling the space surrounding the rod and solenoid. This step is taken to increase the attenuation of the filter and also help thermalize the manganin wire to the copper block and thus to the base temperature stage of the dilution refrigerator. An SMA connector is soldered to each end of the solenoid. Finally, these SMA connectors are fixed to the copper block with 2-56 stainless steel hex screws completing the filter.

The frequency dependence of the filter transmission is measured using an Agilent E5071C network analyzer (300 kHz − 20 GHz) and displayed as a red trace (without 12 nF caps) in Fig. 2.4(a). All measurements are performed at room temperature unless otherwise stated. The 2 kΩ resistance of the solenoid produces the 27 dB of attenuation in the lowest frequency region of the spectrum. The transmission level enters the noise floor of the network analyzer at 220 MHz.[1] The filter begins to fail in the GHz range. Peaks emerge out of the noise floor at 4.6 GHz and 12.2 GHz where the attenuation changes

[1]VNA noise floor: -120 dB for 300 kHz to 10 MHz, -130 dB for 10 MHz to 10 GHz, -120 dB for 10 GHz to 20 GHz

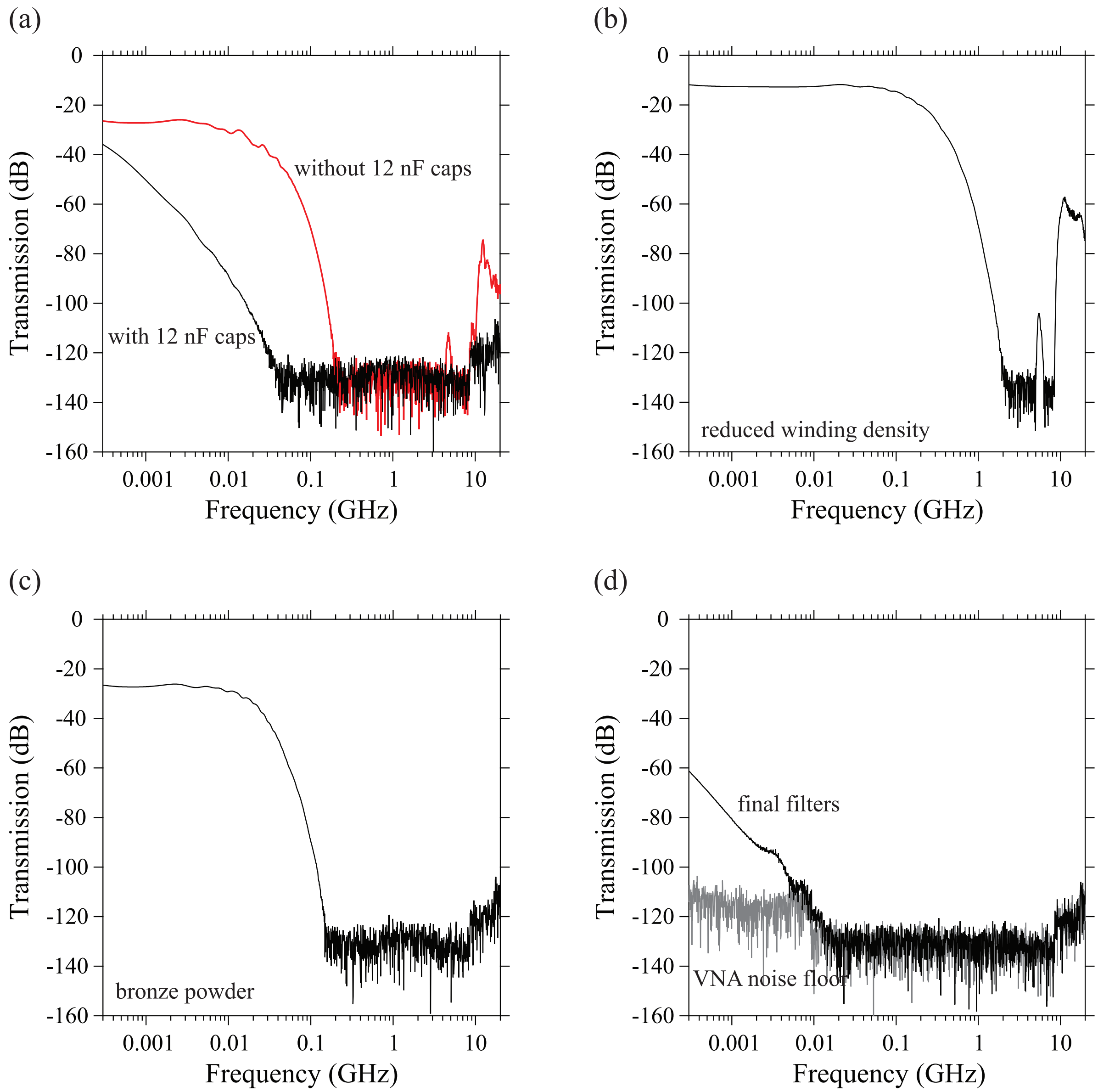

Figure 2.4: (a) Copper powder filters measured at 300 K. (b) Copper powder, reduced (/7) winding density. (c) Bronze powder, high winding density. (d) Transmission of the final filter configuration measured at 4.2 K [filters of (a) connected in series].

to 113 dB and 75 dB respectively. Speculating that these failures are due to inter-turn capacitance in the manganin coil, a filter is constructed with an approximately seven times reduction in turn density. Measurements for this new filter are displayed in Fig. 2.4(b) and reveal that similar problems remain. The peaks in this case are located at 5.5 GHz and 11 GHz. Attenuation in the GHz range can be improved, however, by adding capacitors in parallel with the manganin coil. Following Lukashenko et al., 12 nF, NPO dielectric, discoidal capacitors (Spectrum Control Technology) are soldered to each of the SMA connectors as shown in Fig. 2.3(b) [46]. The data for this filter, displayed as a black trace in Fig. 2.4(a), shows an attenuation level that enters the noise floor at 40 MHz and remains below the noise floor to 20 GHz.

The GHz frequency problems with the powder filter can also be eliminated by substituting copper powder for a more electrically resistive powder such as bronze or stainless steel [44, 46, 47]. To demonstrate this fact, a bronze powder filter without capacitors is constructed. The bronze powder (from Kennametal) is mixed with Stycast 1266 epoxy, 50/50 by weight, and the manganin solenoid is wound with no separation between the turns. The transmission versus frequency data for this bronze powder filter in Fig. 2.4(c) shows that the problems in the GHz frequency range are indeed eliminated.

Concerns about cooling a comparatively low thermal conductivity powder such as bronze (or stainless steel) motivated the choice to instead use two copper powder filters for each electrical lead. For the gates, one of the two filters is of the LC type and the other is a copper powder filter without capacitors [i.e. one of each from Fig. 2.4(a)]. Transmission data for this combination of two filters measured at 4.2 K is displayed in Fig. 2.4(d). The attenuation level stays below the noise floor of the analyzer from 15 MHz to 20 GHz.

Since the electrical leads to the gates do not carry current, the cutoff frequency of the gate leads can be lowered using a resistor without concern about increasing the heat load on the mixing chamber. For all gates except the two high bandwidth plungers, 200 kΩ metal film, thru-hole style resistors are mounted inside copper blocks and connected at the input of the powder filters as shown in Fig. 2.3(c). The complete filter circuit is shown in Fig. 2.5(a). In an attempt to minimize the parasitic capacitance of the resistors, each resistor is mounted inside a hole in the copper block. The diameter of this hole is only slightly larger than the diameter of the resistor. The resistors are thermally connected

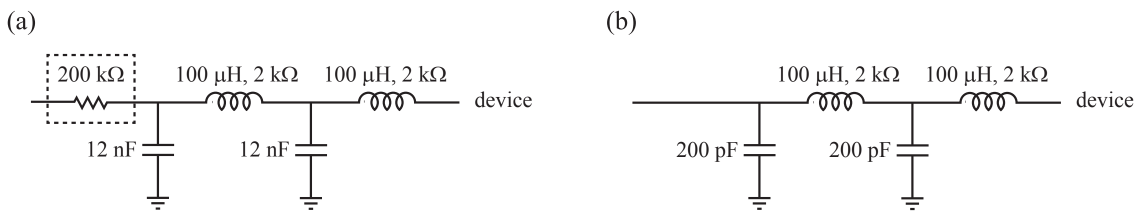

Figure 2.5: (a) Filter circuit for the gates. The 200 kΩ resistor is excluded for the DC lines to the high-bandwidth plunger gates. The inductance of the copper powder filter solenoid is measured at 100 Hz. (b) Filter circuit for the ohmic contacts. Each solenoid has ~200 pF of stray capacitance to the copper shield.

to the copper blocks using vacuum grease. Using a waveform generator and a digital oscilloscope, the 3 dB bandwidth of the complete low frequency gate line is measured to be 30 Hz. Low frequency connections to the plunger gates are made via bias tees as explained in Section 2.5. Since each bias tee contains a 100 kΩ chip resistor, the 200 kΩ resistors in the copper blocks are not necessary for these gates. The corresponding circuit has a bandwidth of approximately 40 Hz (note that the bias tee resistors are on the output side of the powder filters). Due to concerns about charge detection bandwidth and capacitive loading of the Ithaco (see Section 2.6), the electrical leads to each of the four ohmic contacts are filtered using two copper powder filters without capacitors. The solenoid of each copper powder filter has a stray capacitance to ground of about 200 pF. The circuit is shown in Fig. 2.5(b). The bandwidth of the lines to the ohmics is 200 kHz.

2.4 Electron Temperature

In order to observe single electron tunneling phenomena involving a single quantized energy level, the available thermal energy $k_B T$ must be much less than the single particle energy level spacing $\Delta E \approx 100\ \mu\text{eV}$ (i.e. $T \ll 1$ K). This requirement is met by mounting the quantum dot device on the mixing chamber stage of a dilution refrigerator with base temperature $T_b \approx 10$ mK. Instrumentation and thermal noise transmitted to the device via electrical leads, however, can prevent the electron temperature of the 2DEG, T_e, from reaching T_b. Filtering the leads, as described in Section 2.3, is an attempt to keep T_e close to T_b. Electron temperature is therefore an appropriate metric for characterizing the effectiveness of the filters. Attempts to measure electron temperature are described in this section.

The leads of a quantum dot device contain a Fermi-Dirac distribution of electrons at temperature T_e. Any property of a quantum dot system that involves exchange of electrons with the leads therefore depends on T_e through the Fermi function. For example, T_e can be extracted from a single dot conductance resonance peak [48, 49]. Beenakker [48] provides an expression for the dot conductance

$$G = \frac{e^2}{4k_B T_e} \frac{\Gamma_S \Gamma_D}{\Gamma_S + \Gamma_D} \cosh^{-2}\left(\frac{\alpha \Delta V_G}{2k_B T_e}\right), \tag{2.1}$$

where Γ_S and Γ_D are the tunnel rates to the source and drain leads, ΔV_G is the change in the gate voltage V_G (gate C of Fig. 2.2) required to sweep out the resonance, and $\alpha = 80$ meV/V is the lever arm for the gate extracted from a Coulomb diamond measurement. Eq. 2.1 is derived assuming the resonance is thermally broadened, not tunnel rate broadened ($h\Gamma \ll k_B T_e$), and only a single energy level participates in transport ($k_B T_e \ll \Delta E$). Fig. 2.6(a) shows measurements of G as a function of ΔV_G for fifteen fridge temperatures. Temperature dependence in the peak shape is observed down to the lowest fridge temperature. This data is acquired by an AC resistance measurement. A lock-in amplifier applies a 1 μV_{rms}, 12 Hz sine wave to the source lead and the Ithaco is connected to the drain lead (10^{-9} A/V setting). The lock-in measures the output of the Ithaco. Attempts at curve fitting several peaks of (a) using Eq. 2.1 are shown in (b). Two parameters are extracted from the fitting procedure, electron temperature and the tunnel rate dependent prefactor. Unfortunately, as noted in the figure, the values of T_e are larger than the fridge temperature in all cases. To gain insight into this discrepancy, the full-width at half-maximum (FWHM) of the conductance peak is plotted as a function of fridge temperature in (c). The peak width seems to decrease steadily until about 50 mK where a distinct change in slope is evident. The dashed line is the theoretical prediction of Eq. 2.1 [32]. The data for fridge temperatures above 50 mK lies near a line (solid) that runs parallel to this dashed line. The data appears shifted vertically upward due to some broadening mechanism that is not considered in the model that produces Eq. 2.1. So even

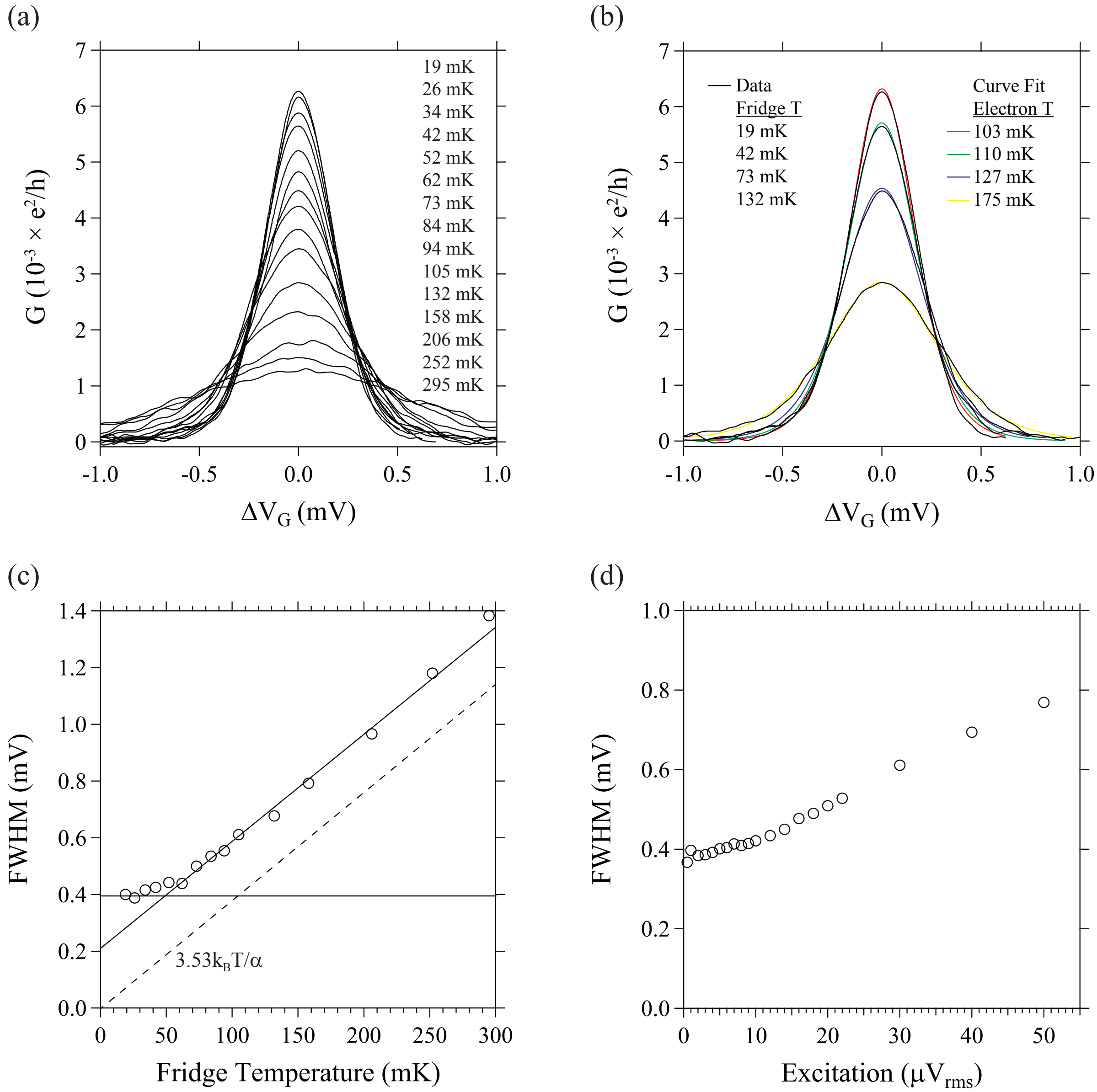

Figure 2.6: (a) Conductance resonances at several fridge temperatures. (b) Conductance resonance and associated curve fits using Eq. 2.1. (c) FWHM of a conductance peak as a function of fridge temperature. Dashed line: theoretical prediction. (d) FWHM of a peak as a function of source-drain AC excitation.

though there is temperature dependence in the FWHM for fridge temperatures down to 50 mK, the curve fit at the lowest fridge temperature of 19 mK produces $T_e \approx 100$ mK. Essentially the T_e extracted from the fit characterizes the effect of all peak broadening mechanisms, not just temperature. The loss of temperature dependence in the FWHM below 50 mK is not understood.

The excitation could produce broadening but $V_{SD} = 1\ \mu\mathrm{V_{rms}}$ is chosen to avoid this possibility. That is, $eV_{SD}/k_B \approx 11$ mK. A plot of FWHM as a function of excitation voltage is shown in (d). Excitation dependence into the few microvolt range is observed. Unintended DC voltages from the Ithaco and thermocouples at solder joints in the wiring could also contribute to broadening the peak since they increase the bias window (Section 1.4). An attempt is made to mitigate this problem by applying a canceling DC voltage across the dot in addition to the AC excitation. The voltage required is determined from a Coulomb blockade diamond measurement (Section 1.4.1). Essentially the voltage that minimizes the FWHM of a peak (all other parameters remaining the same) is chosen. For these measurements approximately, 25 μV is required. Another possibility is 60 Hz noise on the wiring to the device which could produce broadening during the several minute long scan required to sweep out a peak. Lastly, the tunnel rates to the leads could be the source of the broadening. Whatever the source, it is found to be influenced by this dot-to-lead coupling. Decreasing the tunnel coupling decreases the FWHM of a conductance resonance. Fig. 2.7 displays the best effort to minimize the FWHM. The data corresponds to a fridge temperature of 19 mK. The same 1 $\mu\mathrm{V_{rms}}$ excitation is employed and the Ithaco gain is increased to the 10^{-10} A/V setting. A curve fit using Eq. 2.1 gives an electron temperature of 70 mK. It should be noted, however, that even with this better upper bound for the electron temperature, the regime of pure thermal broadening [dashed line of Fig. 2.6(c)] could not be reached.

DiCarlo et al. suggest an alternative technique for determining T_e, one that does not involve the coupling of the dots to the leads but also depends on the Fermi function [50]. They note that a detuning sweep crossing a charge transfer line produces a step in QPC conductance with a shape that depends on T_e [50, 51]. An example sweep trajectory, shown as a black arrow in the stability diagram of the lower left inset of Fig. 2.8, crosses the charge transfer line separating the (1,1) and (0,2) regions. Raw QPC conductance

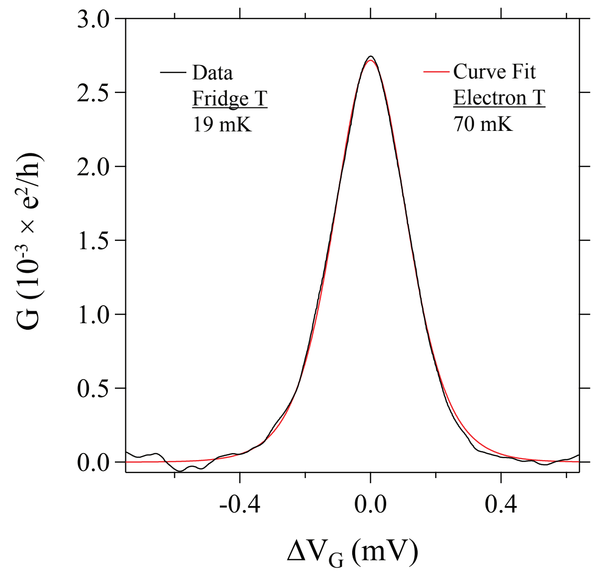

Figure 2.7: Minimum width conductance resonance. Conductance resonance measured at a fridge temperature of 19 mK and the corresponding curve fit. The electron temperature extracted from the fit is 70 mK.

data corresponding to a refrigerator temperature of 105 mK is displayed in the upper right inset. It shows the step associated with the charge transfer and the background slope due to the direct coupling of the plunger gates to the QPC (Q1, RS). It is acquired using the AC resistance technique discussed above (50 μV_{rms} excitation). Following DiCarlo et al., the data is plotted in units of left dot charge, M, in the main figure after a best-fit line is subtracted to remove the background slope. Note that $M = 1$ for (1,1), $M = 0$ for (0,2), and $0 < M < 1$ in the charge transfer region. The gate voltage axis is converted to ε in units of μeV using the lever arms calculated in Section 1.7.2 and displayed in Table 1.1. The charge transfer line corresponds to $\varepsilon = 0$. Data for 12 mK, 34 mK, 52 mK, and 105 mK are displayed. It appears the filtering is sufficient to observe temperature dependence in the $0 \to 1$ transition width below 34 mK.

An expression for $M(\varepsilon)$ is found by modeling the DQD as a two-level system with basis kets $|1, 1\rangle$ and $|0, 2\rangle$ corresponding to charge states (1,1) and (0,2) respectively. The

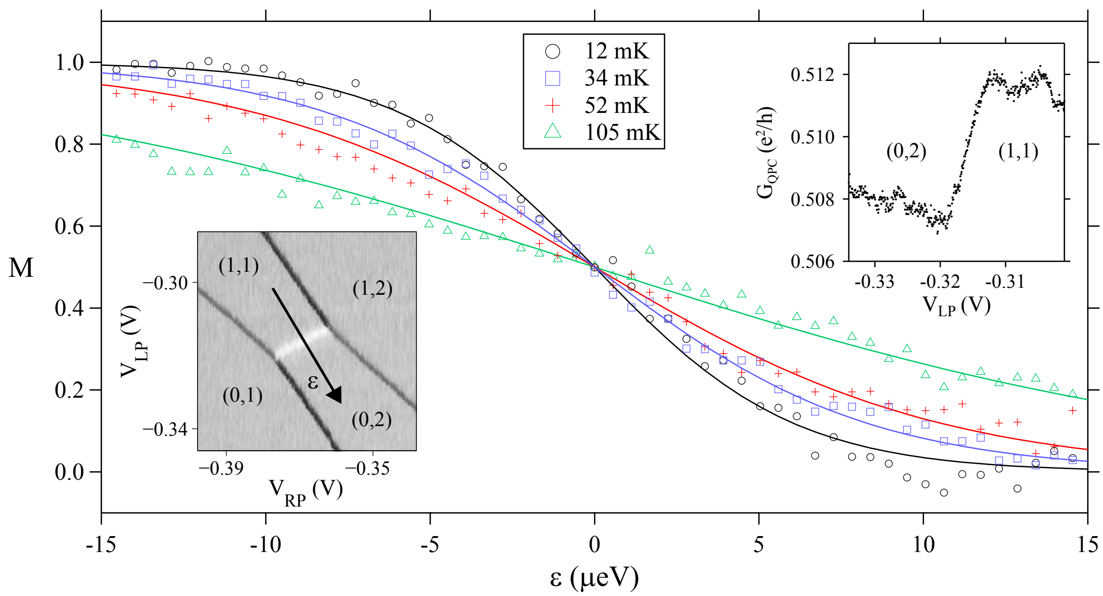

Figure 2.8: Probability of finding an electron on the left dot as a function of detuning for several fridge temperatures. Solid lines are fits to the data assuming $t = 0$. Lower left inset: Stability diagram showing the detuning trajectory (arrow) used to acquire the data of the main figure. Upper right inset: Raw QPC conductance data for the 105 mK case.

interdot tunnel coupling t mixes these states producing eigenstates

$$|a\rangle = \cos\frac{\theta}{2}e^{-i\phi/2}\,|1,1\rangle + \sin\frac{\theta}{2}e^{i\phi/2}\,|0,2\rangle$$
$$|b\rangle = -\sin\frac{\theta}{2}e^{-i\phi/2}\,|1,1\rangle + \cos\frac{\theta}{2}e^{i\phi/2}\,|0,2\rangle$$

where $\tan\theta = 2t/\varepsilon$. The corresponding eigenvalues are $E_a = E_m + \Omega/2$ and $E_b = E_m - \Omega/2$, where $E_m = \frac{1}{2}(E_{1,1} + E_{0,2})$ is the average energy of the unperturbed states and $\Omega = \sqrt{\varepsilon^2 + 4t^2}$ (see Appendix B). Since $E_a - E_b = \Omega$, $|a\rangle$ is the excited state and $|b\rangle$ is the ground state. The excited state is thermally occupied with average occupation given by the Fermi function $f(\Omega) = 1/[1 + \exp(-\Omega/k_B T_e)]$. This is the source of T_e dependence in the data. With only two states, the ground state has average occupation $1 - f(\Omega)$. Since the average left dot charge, M, is equivalent to the average occupation of the (1,1) state, the first step in producing an expression for M is calculating the probability of finding the DQD in (1,1) for each of the eigenstates. When the system is in the ground state, the DQD is found in (1,1) with probability $|\langle 1,1|b\rangle|^2$. A calculation of this probability proceeds as follows:[2]

$$\begin{aligned}
|\langle 1,1|b\rangle|^2 &= \sin^2\frac{\theta}{2} \\
&= \frac{1}{2}\left(1-\sqrt{\frac{1}{\tan^2\theta+1}}\right) \\
&= \frac{1}{2}(1-\varepsilon/\Omega)
\end{aligned}$$

A similar collection of steps gives $|\langle 1,1|a\rangle|^2 = \frac{1}{2}(1+\varepsilon/\Omega)$.[3] A calculation of M can now proceed as follows:

$$\begin{aligned}
M &= f(\Omega)(|\langle 1,1|a\rangle|^2) + [1-f(\Omega)](|\langle 1,1|b\rangle|^2) \\
&= \left(\frac{1}{1+\exp(-\Omega/k_BT_e)}\right)\left(\frac{1}{2}+\frac{\varepsilon}{2\Omega}\right)\left(1-\frac{1}{1+\exp(-\Omega/k_BT_e)}\right)\left(\frac{1}{2}-\frac{\varepsilon}{2\Omega}\right) \\
&= \frac{1}{2}\left[1-\frac{\varepsilon}{\Omega}\left(\frac{\exp(-\Omega/k_BT_e)-1}{\exp(-\Omega/k_BT_e)+1}\right)\right] \\
&= \frac{1}{2}\left[1-\frac{\varepsilon}{\Omega}\tanh\left(\frac{\Omega}{2k_BT_e}\right)\right]
\end{aligned}$$

The solid lines in Fig. 2.8 are fits to the data using this expression and assuming $t = 0$ (i.e. in the limit $t \ll k_BT_e$). They are simply meant as guides to the eye. Incidentally the $t = 0$ curve fit for the 12 mK (base temperature) case gives $T_e = 35$ mK (95% confidence bounds: 32-38 mK). Of course this overestimates T_e since with $t = 0$, T_e solely determines the transition width. It is not understood why this technique produces a lower value for T_e than the conductance resonance technique. Perhaps the tunnel coupling to the leads is weaker for this configuration of the device.

---

[2]Required trigonometric identities: $\sin^2\frac{\theta}{2} = (1-\cos\theta)/2$, $\tan^2\theta+1 = 1/\cos^2\theta$

[3]Required trigonometric identities: $\cos^2\frac{\theta}{2} = (1+\cos\theta)/2$, $\tan^2\theta+1 = 1/\cos^2\theta$

2.5 High-bandwidth Gates

Observation of Landau-Zener-Stückelberg (LZS) oscillations of the DQD two-electron spin qubit (Chapter 4) involves transmitting Gaussian shaped pulses with rise times of 1-20 ns from a Tektronix AWG7122B arbitrary waveform generator (AWG) to the plunger gates of the device via semi-rigid coaxial cables. Each of the two high-bandwidth lines consists of several coaxial cables of different electrical and thermal conductivities connected together (Fig. 2.9). Copper cables (UT-141) run from the AWG to hermetic SMA bulkheads at the top of the dilution refrigerator. Beryllium copper cables (UT-85, silvered inner conductor) are used from room temperature to the 1 K pot (1.5 K) where they are thermally anchored using the copper clamp shown in Fig. 2.10(a). Due to their low thermal conductivity, superconducting NbTi cables run from the 1 K pot to the mixing chamber. They are heat sunk to the still plate (700 mK) and the mixing chamber using the copper clamps shown in Fig. 2.10(a) and (b) respectively.[4] Copper coax is used on the mixing chamber stage to connect to the bias tees and ultimately to the MCX connectors on the NRC microwave frequency compatible ceramic board. To attenuate noise produced by the AWG, a 10 dB attenuator is attached to each of the two hermetic SMA bulkheads at the top of the fridge. To further attenuate instrumentation noise and also room temperature thermal noise, 26 dB of attenuation (XMA Corporation) is placed in each line at the 1 K pot stage [Fig. 2.10(a)]. Note that an attenuation level of 23 dB is required to attenuate 300 K radiation down to 1.5 K, the temperature of the 1 K pot. (i.e. $10\log_{10}(300/1.5) = 23$ dB). This fact guided the choice of the slightly larger value of 26 dB.

The bias tees for the high bandwidth gates are mounted on the mixing chamber plate as shown in Fig. 2.10(c). They are modified versions of model BT-0018 made by Marki Microwave. The circuit connecting the DC input port to the RF + DC output port is removed and replaced by a 100 kΩ metal film chip resistor. The RF part of the circuit is unchanged. It contains a 1 μF capacitor made with an X5R dielectric (Venkel, part no. C0402X5R100-105KNP) in parallel with a 100 nF capacitor made with an X7R dielectric (American Technical Ceramics, part no. 545L104KCA10). These dielectrics are highly

[4] Importantly the clamp is connected directly to the mixing chamber rather than the mixing chamber plate where the device is heat sunk.

temperature dependent. The total capacitance is 38 nF at 4.2 K. A schematic of the simple bias tee circuit is shown in Fig. 2.9.

To test the coaxial cables, attenuators, and bias tees, the two lines are connected together at the output of the bias tees and the frequency response at room temperature is measured using a network analyzer. The result is divided by two and displayed in Fig. 2.11(c) - no sample holder. At 1 GHz, the attenuation of one line is 41 dB, 5 dB beyond the 36 dB of fixed attenuation mentioned above. Approximately 2 dB is due to the 5.5 m copper coax in the room and another 1 dB comes from the 1.5 m BeCu coax. The remaining 2 dB of the attenuation is due to cabling below the 1 K pot. Of course, this latter contribution may decrease when the fridge is cold.

Fig. 2.11(a) shows the ceramic board and 19-pin socket. The middle pin of each side of the socket is connected to the center pin of a neighboring MCX connector. Even though there are four MCX connectors on the board, only the left and right ones (LP, O4) are designed to communicate microwave frequency signals to the device [Fig. 2.11(b)]. This is accomplished by running a ground pin (G1, G2) beside the signal pin. A neighboring ground pin for the top and bottom MCX jacks is not part of the design. With the left MCX jack used for the left plunger gate (LP) and the right MCX jack used for the RF-QPC readout (O4), a modification is made to the sample holder to allow transmission of microwave signals to the right plunger gate (RP) via the bottom MCX jack. The simple change involves creating a neighboring ground pin (G3) by soldering copper foil from the ground (gold) of the ceramic board to the pin second from the left in the bottom row as shown in Fig. 2.11(a). To test the high bandwidth connections for the plunger gates including the sample holder, a 19-pin mating connector with short pieces of coax soldered to the appropriate pins is plugged into the 19-pin socket. The shields of the coaxial cables are soldered to the ground pins. Transmission as a function of frequency measured at room temperature from the output of the AWG to one of these coaxial cables is shown in Fig. 2.11(c) - with sample holder. Similar behavior is observed for both plunger gate lines. The synchronization of the two lines is also tested. Pulses from the AWG are sent to the sample holder and displayed on a digital oscilloscope. The difference in electrical length is easily corrected by placing two male-to-female SMA adapters on the left plunger (LP) output of the AWG.

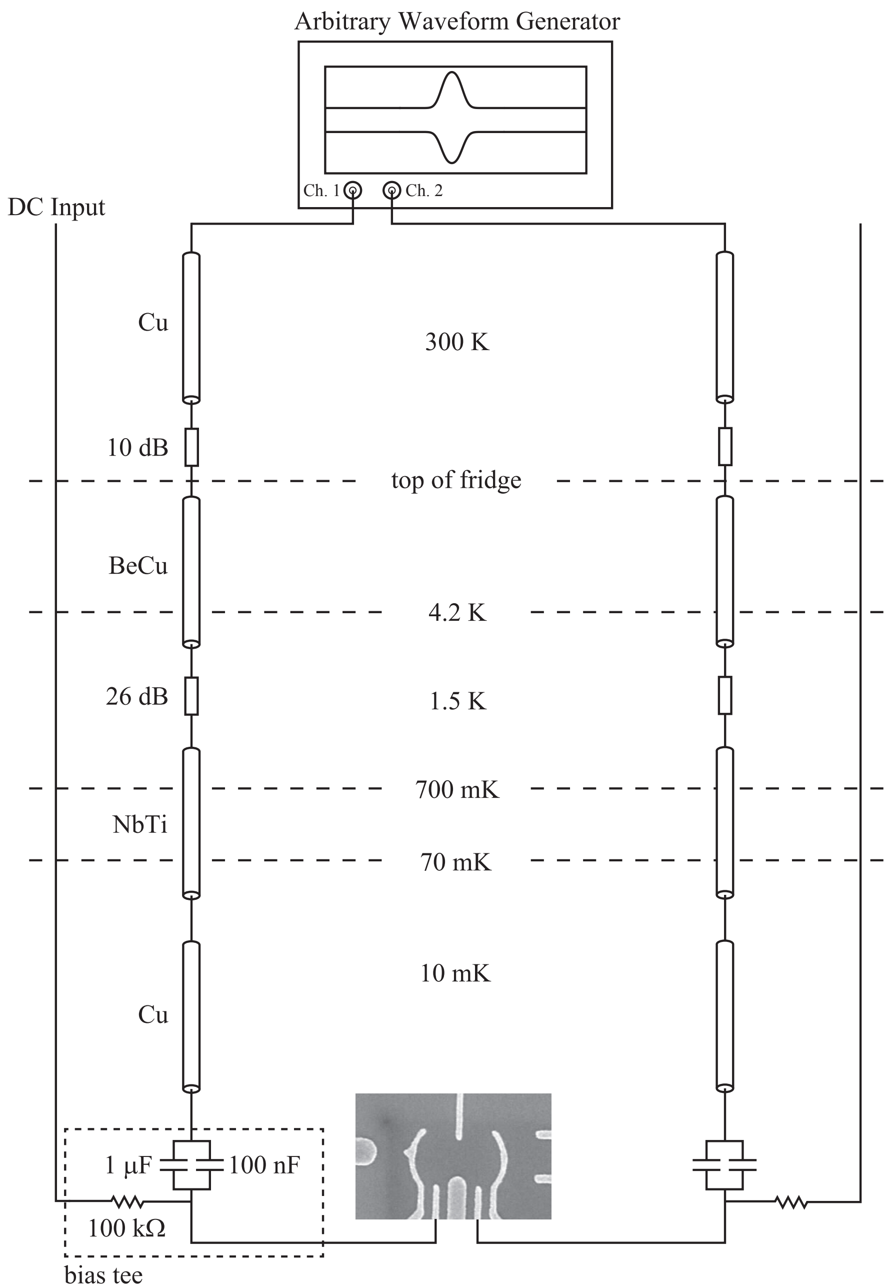

Figure 2.9: Schematic of the high bandwidth gate lines. Microwave frequency signals are communicated to the plunger gates via semi-rigid coaxial cables and bias tees.

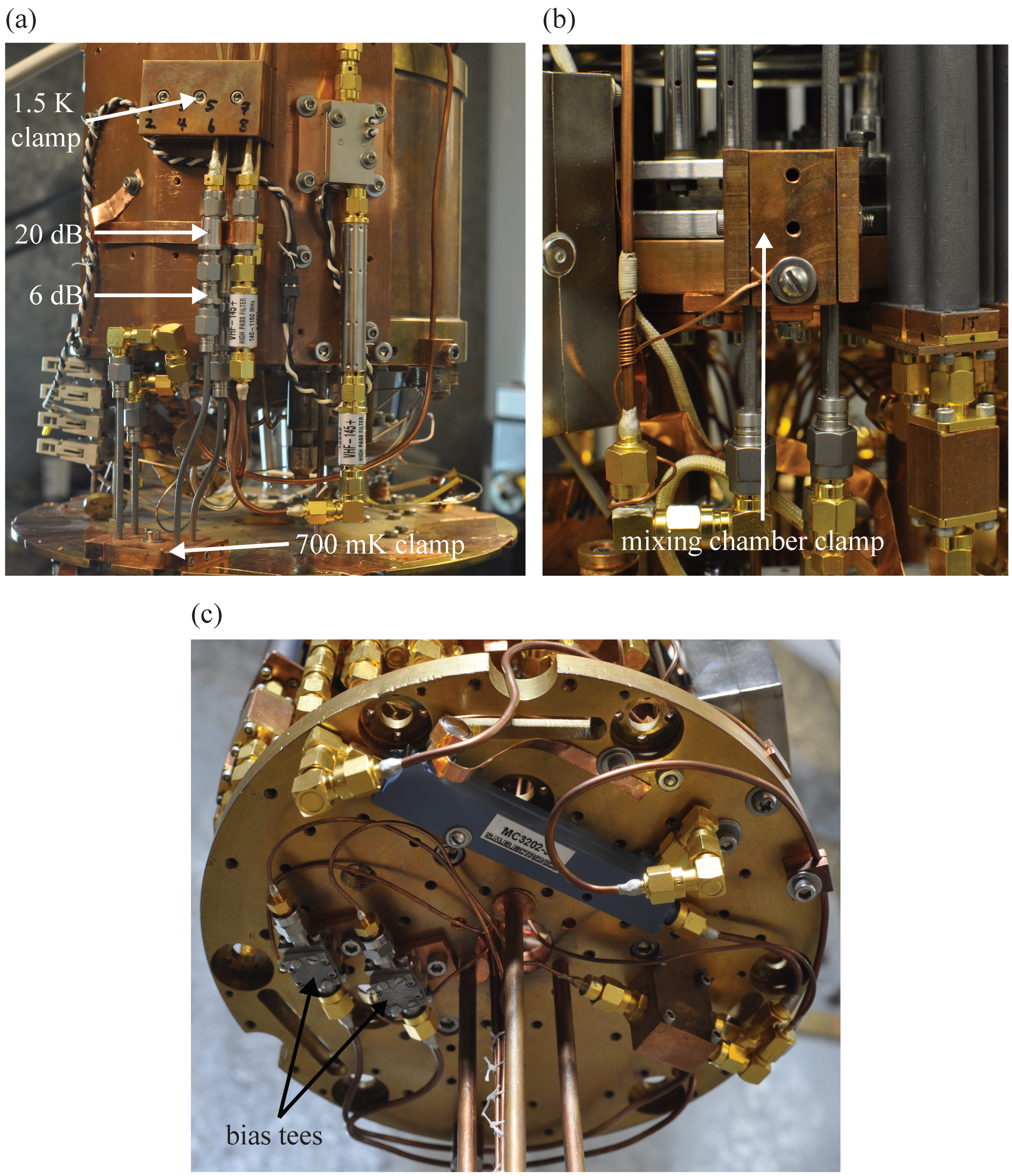

Figure 2.10: (a) Attenuators on the 1 K pot. Heat sinking clamps for the semi-rigid coaxial cables on the 1 K pot and still plate. (b) Coax heat sinking clamp on the mixing chamber. (c) Bias tees for the high-bandwidth gates heat sunk to the mixing chamber plate.

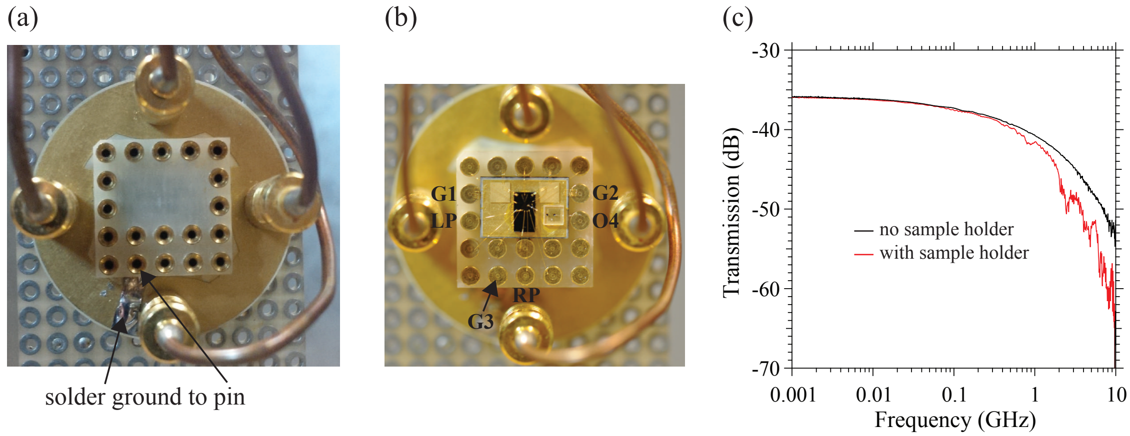

Figure 2.11: (a) Modified NRC sample holder. To make the bottom middle pin (RP) compatible with high bandwidth operation, a solder connection is made between a neighboring pin and the ground on the ceramic board. (b) Device mounted to a 19-pin connector. High bandwidth pins LP and RP are connected to the left and right plunger gates respectively. Pin O4 is connected to the inductor used in the RF-QPC readout. (c) Frequency response of the high bandwidth gate lines including attenuators (10 dB at 300 K, 26 dB at 1.5 K) and bias tees (on mixing the chamber).

The high bandwidth gates are calibrated using the technique described in Ref. [52]. A stability diagram in the few electron regime of the DQD is displayed in Fig. 2.12(a). The calibration procedure involves using the AWG to apply a 10 kHz, 158 $\mathrm{mV_{pp}}$ square wave to gate RP during the acquisition of a stability diagram. The result is shown in Fig. 2.12(b). Because the dot-to-dot and dot-to-lead tunnel rates exceed the square wave frequency, two overlapping stability diagrams are created (one for the maximum amplitude, one for the minimum amplitude of the square wave). Measuring ΔV_{RP} separating the two electron triple points indicates that 158 $\mathrm{mV_{pp}}$ at the AWG is converted to 5 $\mathrm{mV_{pp}}$ at the device as expected (158 $\mathrm{mV_{pp}} \div 63 \times 2 = 5$ $\mathrm{mV_{pp}}$; the factor of 63 coming from the 36 dB of attenuation and the factor of 2 from the fact that the gates present an open circuit, not a 50 Ω impedance, to the AWG). Repeating the procedure for gate LP results in a vertical splitting of the stability diagram as shown in Fig. 2.12(c). In this case, the 158 $\mathrm{mV_{pp}}$ wave produced by the AWG is converted to a $\Delta V_{LP} = 6$ $\mathrm{mV_{pp}}$ wave at the device, slightly different than expected.

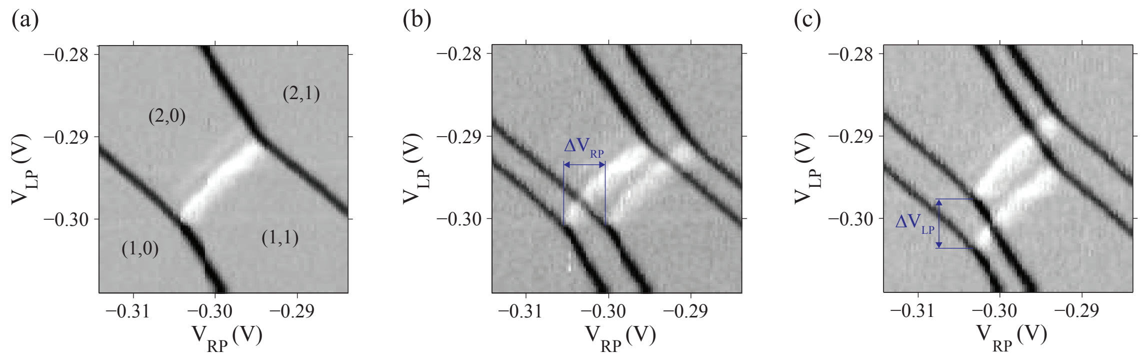

Figure 2.12: Calibration of the high bandwidth gates. (a) Stability diagram in the few electron regime. (b) Stability diagram acquired in the presence of a 158 $\mathrm{mV_{pp}}$ (5 $\mathrm{mV_{pp}}$ at gates), 10 kHz square wave on gate RP. (c) Repeat with a similar square wave on gate LP.

In some cases, the high bandwidth gates are used to measure tunnel rates. Consider a vertical 1D sweep through the stability diagram of Fig. 2.13(a) from $V_{LP} = -0.418$ V to -0.398 V measured at $V_{RP} = -0.434$ V (vertical line near the V_{LP}-axis). Similar to the gate calibration, if a square wave with frequency less than the left dot-to-lead tunnel rate is applied to gate LP during the sweep, a doubling of the addition line is observed. Using a MATLAB script to change the square wave frequency between consecutive sweeps produces the data displayed in Fig. 2.13(b). The amplitude of the wave is 12 $\mathrm{mV_{pp}}$ at gate LP. The horizontal axis is the sweep number, i, related to the square wave frequency by the expression

$$f = f_{start}\left(\frac{f_{end}}{f_{start}}\right)^{\frac{i}{n}}.$$

For the data in Fig. 2.13, there are 100 steps from $i = 0$ giving $f = f_{start} = 200$ Hz to $i = 99 = n$ giving $f = f_{end} = 200$ MHz. Below 500 Hz, the lines are broadened indicating that the low frequency cutoff of the bias tees is approximately 500 Hz. This cutoff is similar to what is expected from the RC time constant of the bias tee components. For $R = 100$ kΩ and $C = 38$ pF (4.2 K), the time constant is ~4 ms (250 Hz).

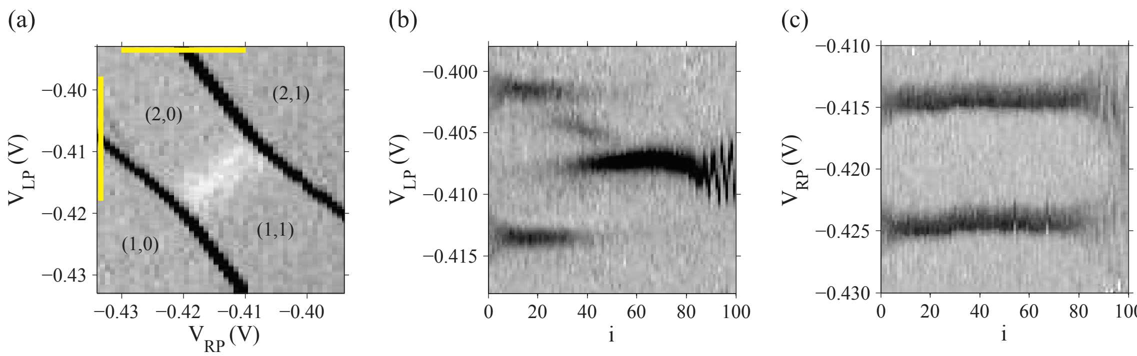

Figure 2.13: Dot-to-lead tunnel rate measurements. (a) Stability diagram. (b) Left dot-to-lead tunnel rate measurement: repeatedly sweep along the vertical line in (a) while applying a square wave to gate LP. The emergence of the single line at i = 28 indicates a tunnel rate of 10 kHz. (c) Attempt to measure the right dot-to-lead tunnel rate [horizontal line in (a)]. The tunnel rate exceeds the 20 MHz limit of this technique.

As the frequency increases, the two lines fade and at 10 kHz (i = 28) they are replaced by a single line. Above 10 kHz, an electron cannot tunnel between the left dot and the left lead in response to the square wave. The left dot-to-lead tunnel rate is thus approximately 10 kHz. Fig. 2.13(c) shows data for a horizontal sweep from $V_{RP} = -0.43$ V to -0.41 V at $V_{LP} = -0.393$ V through a right dot addition line [horizontal line in (a)] acquired in the presence of a 10 $\mathrm{mV_{pp}}$ square wave applied to gate RP. In this case, the doubling of the addition line is observed up to 20 MHz ($i \approx 83$). At 20 MHz, both lines start to broaden. The smearing between the lines may be the result of gate bandwidth limitations since the rise and fall of the square wave contains frequency components in the GHz range. The source of the smearing above the top line and bellow the bottom line is not understood. For this configuration of the device, the right dot-to-lead tunnel rate is simply too large to measure using this method. Clearly the technique is only appropriate for measuring tunnel rates in the 500 Hz to 20 MHz range.

2.6 DC-QPC Readout Sensitivity

The DC-QPC charge detector introduced in Section 1.6 is analyzed in greater detail here. The sensitivity and bandwidth of this readout technique are summarized in Fig. 2.14. As in Section 1.6, charge state changes of the DQD are detected using the QPC formed between gates Q1 and RS. The sensitivity of the QPC to the electrostatic environment is found to be highest at $0.22 \times 2e^2/h$. This working point is labeled with a black circle in the conductance data shown in Fig. 2.14(a). A stability diagram in the few-electron regime of the DQD, acquired by measuring the QPC transconductance, is displayed in Fig. 2.14(b). With R_{QPC} = 60 kΩ, a bias voltage of V_{QPC} = 200 μV produces a QPC current of I_{QPC} = 3 nA. Sweeping V_{LS} along the trajectory represented by the vertical dashed line in Fig. 2.14(b) produces the trace of I_{QPC} in Fig. 2.14(c). Moving from right to left towards more negative values of V_{LS}, an electron is ejected from the right dot at $V_{LS} = -0.6325$ V changing the charge state from (2,1) to (2,0) and increasing I_{QPC} by 50 pA. Reducing V_{LS} further, an electron is removed from the left dot at $V_{LS} = -0.644$ V in the transition (2,0) → (1,0) increasing I_{QPC} by another 24 pA. Parasitic gating of the QPC by gate LS is compensated by moving V_{Q1} more positive during the sweep. This procedure maintains I_{QPC} at an approximately constant value for a fixed DQD charge state. The single electron transitions of the DQD charge state change I_{QPC} by 1.6% in the right dot case and 0.8% for the left dot case, similar to the 1% change reported by the Delft group in their version of the charge detection technique summarized in Ref. [38].

The system noise spectrum measured at the output of the battery powered Ithaco (10^{-7} A/V gain, min. rise time setting) is shown in Fig. 2.14(d). For comparison, the noise spectrum of the preamplifier with an open circuit input is also displayed in the figure. In both cases, the increase in the noise floor in the low frequency end of the spectrum is the result of 60 Hz harmonics. The roll-off starting at 25 kHz is consistent with the bandwidth specification for the preamplifier in the 10^{-7} A/V setting. In the open circuit case, the current noise floor $I_A = 60$ fA/$\sqrt{\text{Hz}}$ between 400 Hz and 25 kHz is also consistent with the specifications. The system noise, however, clearly exceeds this lower bound. The dominant source of noise is the preamplifier input voltage noise, V_A. It is converted to a current noise flowing from the preamplifier input to ground through the parallel combination of R_{QPC}

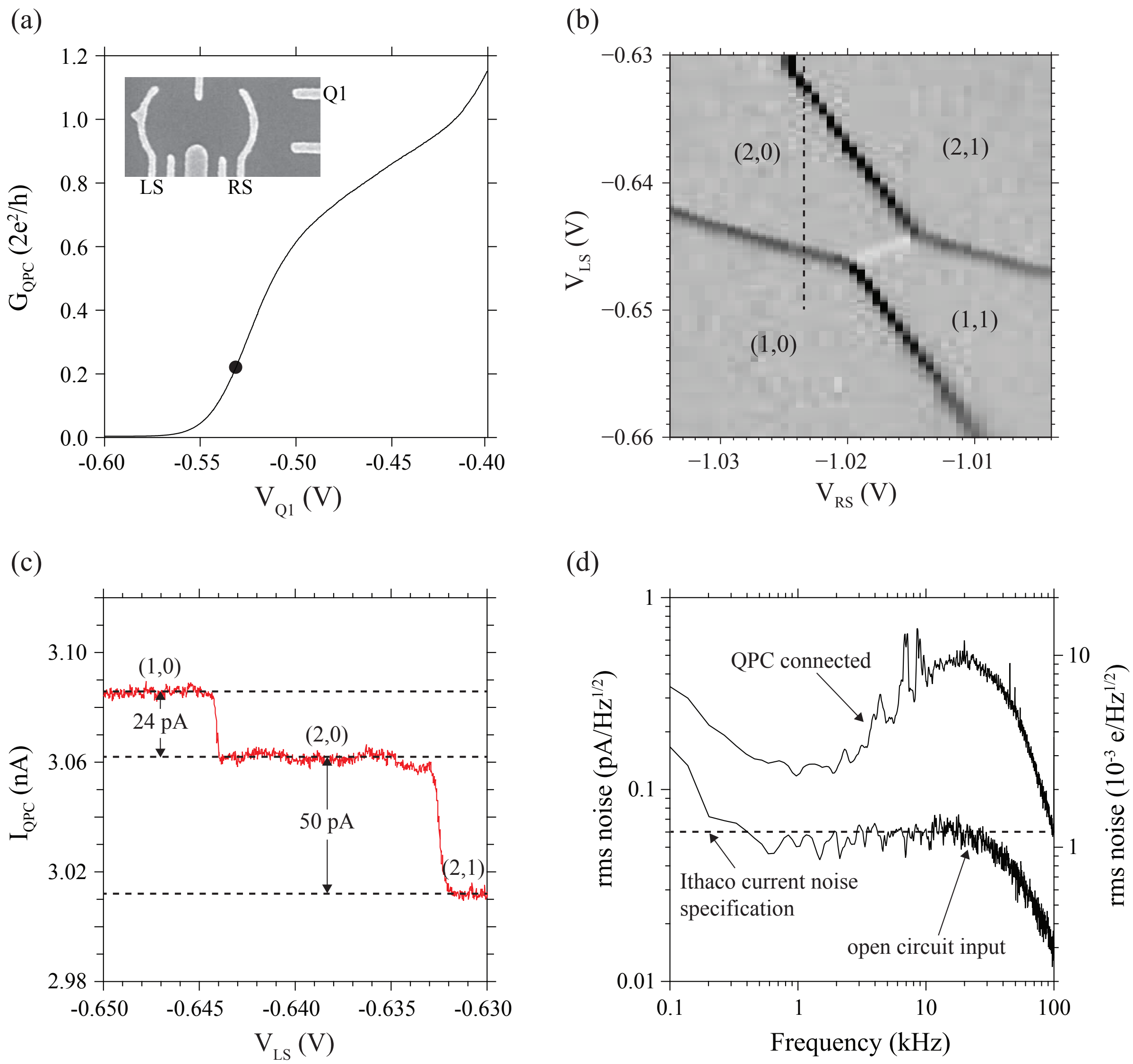

Figure 2.14: (a) QPC conductance ($0.22 \times 2e^2/h$ working point). (b) Stability diagram. (c) I_{QPC} measured along dashed line in (b). (d) Top trace: Ithaco output with the input connected to the QPC through electrical leads and filters. Bottom trace: Ithaco output with open circuit input, 10^{-7} A/V gain [right axis = (left axis)÷(50 pA/e)].

and the capacitance of the lines and filters, C_L. As noted by the Delft group, this current noise, I_{NA}, is simply V_A divided by the impedance of this load. It is given by the following expression:

$$I_{NA} = V_A(1 + j2\pi f R_{QPC} C_L)/R_{QPC}. \tag{2.2}$$

The observed frequency dependence of the system noise is due to the frequency dependent impedance of C_L. The total capacitance of the two copper powder filters is approximately 400 pF (the contribution of the fridge wiring to C_L is unknown). To produce the right axis of Fig. 2.14(d) in units of $e/\sqrt{\text{Hz}}$ (typical units for discussions of charge detector sensitivity), the current noise in units of $\text{pA}/\sqrt{\text{Hz}}$ is divided by 50 pA/e (for an electron leaving the right dot).

The increase in I_{NA} with frequency combines with the 25 kHz roll-off to produce the peak at 20 kHz. Clearly the sensitivity of the readout could be improved by lowering the filter capacitance though perhaps at the expense of an increase in electron temperature. Noise spectrum data from the Delft group is shown in Fig. 2.15 [38]. The current noise is similar to that shown in Fig. 2.14(d). They have better charge sensitivity but note that they use I_{QPC} = 30 nA (i.e. ten times the current bias).

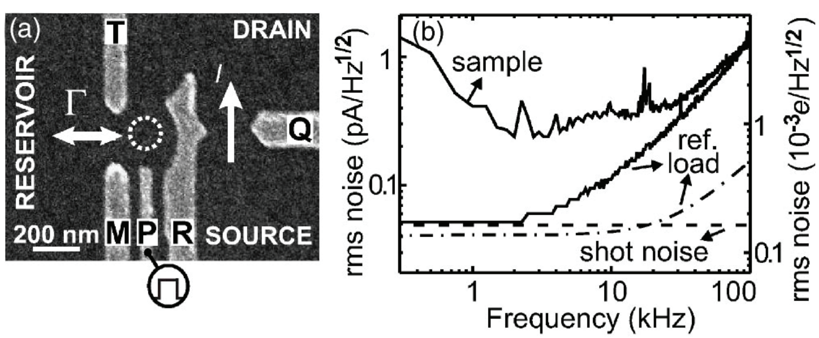

Figure 2.15: Delft device and DC-QPC noise spectrum. (a) Right half of a DQD device operated as a single dot with a QPC charge detector (gate Q, current I). (b) DC-QPC noise spectrum. Sample trace: current preamplifier connected to the device. Ref. load: current preamplifier connector to a 300 pF reference load (both theory and experimental data are shown). Reprinted from Applied Physics Letters **85**, 4394 (2004), with the permission of AIP Publishing.

2.7 Conclusion

Transport measurements of a single dot show that the shielding of the device and the filtering of fridge wiring is sufficient for the electron temperature of the 2DEG to reach 70 mK. Gate noise is low enough that phenomena not involving coupling to the leads display temperature dependence for fridge temperatures below 34 mK. A slight modification to the NRC sample holder allows GHz connections to the plunger gates of the device, necessary for the manipulation of the spin qubit (Chapter 4). The DC-QPC readout has a sensitivity on the order of 10^{-3} $e/\sqrt{\mathrm{Hz}}$ when using a 3 nA bias current.

Chapter 3

RF-QPC Charge Detector

3.1 Principle of Operation

The time constant created by the QPC resistance and the capacitance of the fridge wiring limits the bandwidth of a DC-QPC readout to tens of kHz. By using a cryogenic amplifier mounted on the dilution refrigerator and thus closer to the sample, the Delft group lowers the capacitance of the wiring and improves the bandwidth of the readout to 1 MHz [53]. Increasing the bandwidth further, into the several MHz to tens of MHz range, comes with the demonstration of the radio-frequency quantum point contact (RF-QPC) [26, 27].

Similar to the radio-frequency single electron transistor (RF-SET) [54], the RF-QPC technique uses a matching circuit to transform R_{QPC} down to near $Z_0 = 50\ \Omega$, allowing the QPC to be incorporated into an rf circuit involving coaxial cables and a cryogenic rf amplifier. Typically a simple matching circuit composed of two reactive components, called an L-network, is employed in the RF-QPC readout. Since $R_{QPC} > Z_0$, this L-network takes one of the two forms displayed in Fig. 3.1(a) and (b). Usually circuit (a) is employed although the ETH group uses circuit (b) [55]. Very simply, matching with circuit (a) is accomplished by choosing a shunt capacitance C that satisfies the conditions $\mathrm{Re}(R_{QPC}||C) = Z_0$ and $\mathrm{Im}(R_{QPC}||C) = -j\omega L$. The series inductance with impedance $j\omega L$, of course, cancels the imaginary component leaving the desired Z_0. Since the impedance of L and C are frequency dependent, the matching condition is only satisfied at one frequency. This is certainly a limitation of the L-network technique but it is acceptable in the readout case.

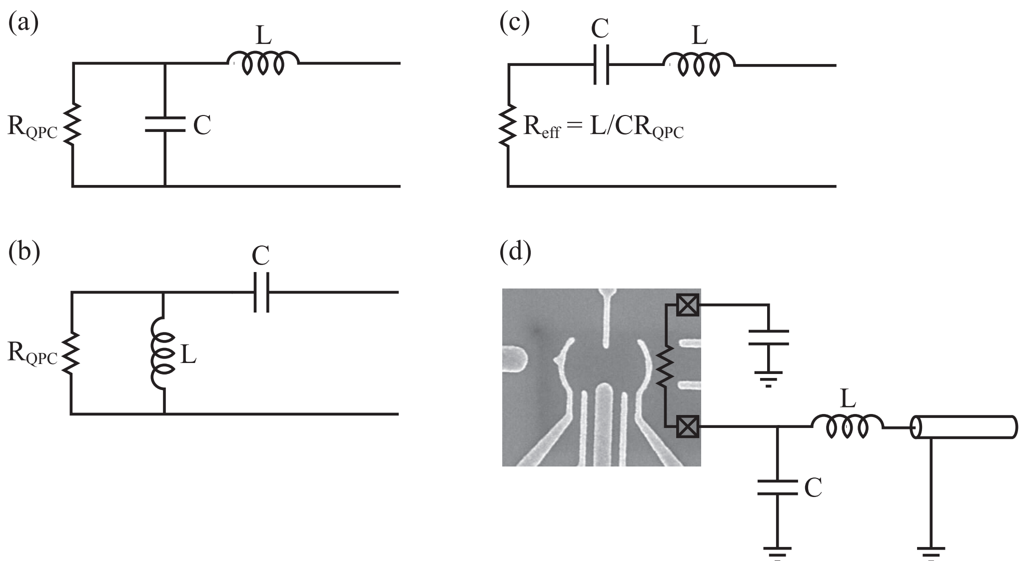

Figure 3.1: (a) and (b) LC matching circuits used to transform the QPC resistance to near 50 Ω. (c) Equivalent circuit for the circuit shown in (a). (d) Matching circuit of (a) connected between a coax and the QPC charge detector of the DQD device. The capacitor connected to the top ohmic contact is used to establish an rf ground.

A detailed analysis of the matching network for an RF-SET is found in the theses of Julie Love [56] and John Teufel [57] from the Schoelkopf group at Yale. The following discussion, also applicable to the RF-QPC case, closely follows their analysis. The input impedance of circuit (a) is

$$Z_{in}(\omega) = j\omega L + \frac{R_{QPC}}{j\omega C R_{QPC} + 1}. \tag{3.1}$$

Setting the imaginary component of $Z_{in}(\omega)$ to zero defines the angular resonance frequency

$$\omega_0 = \sqrt{\frac{1}{LC} - \frac{1}{(CR_{QPC})^2}}.$$

Typically the second term can be ignored, giving the familiar definition of resonance frequency

$$\omega_0 \approx \frac{1}{\sqrt{LC}}. \tag{3.2}$$

The remaining impedance of the circuit on resonance is real and given by

$$Z_{in}(\omega = \omega_0) = \frac{L}{CR_{QPC}}. \tag{3.3}$$

Since the reactance of L and C are equal for $\omega = \omega_0 = 2\pi f_0$, it is typical to define a parameter called the characteristic impedance of the transformer

$$Z_T = \sqrt{\frac{L}{C}} = \omega_0 L = \frac{1}{\omega_0 C}.$$

The input impedance can then be written as

$$Z_{in}(\omega = \omega_0) = \frac{Z_T^2}{R_{QPC}}$$

and the matching condition, $Z_{in} = Z_0$, as

$$Z_0 = \frac{Z_T^2}{R_{QPC}}, \tag{3.4}$$

or equivalently

$$Z_T = \sqrt{Z_0 R_{QPC}}. \tag{3.5}$$

This shows that the design goal for the impedance matching network is one of choosing L and C such that Eq. 3.5 is satisfied for the value of R_{QPC} that maximizes the sensitivity of the charge detector.

The quality factor of a resonant circuit, Q, is defined as the ratio of stored energy to energy lost in one cycle of oscillation. In this case the unloaded quality factor, which characterizes the matching network dampened by only Z_0, is given by

$$Q = \frac{Z_T}{Z_0}, \tag{3.6}$$

and the matching condition of Eq. 3.4 can be written as

$$R_{QPC} = Q^2 Z_0, \tag{3.7}$$

A useful alternative perspective on the matching circuit, developed by Roschier et al. in Ref. [58], again begins with Eq. 3.1. Rationalizing the denominator gives

$$Z = j\omega L + \frac{R_{QPC} - j\omega C R_{QPC}^2}{(\omega C R_{QPC})^2 + 1}.$$

Typically R_{QPC} is tens of kΩ, the resonance frequency is in the range 0.1-2 GHz, and $C \approx 0.5$ pF. Thus $\omega CR \gg 1$, and the 1 in the denominator is ignored producing

$$Z = R_{\text{eff}} + j\omega L + \frac{1}{j\omega C}, \tag{3.8}$$

where $\omega \approx 1/\sqrt{LC}$ and $R_{\text{eff}} = L/CR_{QPC}$ is known as the effective resistance. Eq. 3.8 motivates the construction of the equivalent circuit shown in Fig. 3.1(c). On resonance, the impedance of L and C cancel leaving an input impedance $Z_{in} = R_{\text{eff}}$ as in Eq. 3.3.

The RF-QPC readout is a time-domain reflectometry circuit. The basic principle of the technique is explained with reference to Fig. 3.1(d) which shows the RLC circuit terminating a coaxial cable. Simply, a signal of amplitude V_0^+ and frequency f_0 is sent down the coax and the reflected voltage wave is measured. The amplitude of this reflected wave is $V_0^- = \Gamma V_0^+$, where $\Gamma = (Z_{in} - Z_0)/(Z_{in} + Z_0)$ is the reflection coefficient of the circuit [59]. Similar to the DC-QPC case in which each DQD charge state corresponds to a unique value of R_{QPC} and thus I_{QPC}, the RF-QPC readout maps each charge state to a unique value of R_{QPC}, Z_{in}, Γ, and thus V_0^-.

3.2 Superconducting Matching Network

The matching network for an RF-QPC or RF-SET readout consists of an inductor, L, and its parasitic capacitance to ground, C_p. It is common to employ a commercial (eg. Coilcraft) copper wire chip inductor to make the matching network. Typically these inductors lead to values of C_p in the range 0.4-1 pF [26, 27]. The resulting resonance frequencies are hundreds of MHz and the readout bandwidths are MHz to tens of MHz. For example, Reilly et al. describe an RF-QPC readout based on a chip inductor that has a resonance frequency of 220 MHz and a bandwidth of 8 MHz [26].

To increase the bandwidth, for a given Q, requires increasing f_0 by decreasing either L or C_p or both [60]. Decreasing C_p is preferable because it produces an increase in $Z_T = \sqrt{L/C_p}$ and thus improves impedance matching at the higher f_0. To reduce C_p for their RF-SET, Xue et al. fabricate a lithographically patterned on-chip superconducting aluminum inductor [60]. They are able to achieve $C_p \approx 0.17$ pF and match an SET resistance of 19.2 kΩ at 942 MHz. They report a bandwidth of 50 MHz. In addition to reducing C_p, these inductors, being superconducting, have negligible loss at radio frequencies. By contrast, a normal metal inductor has loss terms associated with dissipation in L and C_p. Reducing these losses by using a superconducting LC circuit should make the reflection coefficient more sensitive to dissipation in the transformed impedance L/C_pR_{QPC} and thus to changes in R_{QPC}, leading to a more sensitive readout.

Primarily motivated by the possibility of improved sensitivity, a lithographically patterned niobium inductor is fabricated for the RF-QPC readout. The planar inductor of Xue et al. is a 14-turn circular spiral with 20 μm turn spacing and 3 μm linewidth. The circular bonding pad in the center of the spiral is 100 μm in diameter. The inductor for the RF-QPC readout also has 20 μm turn spacing but the linewidth is increased to 5 μm due to resolution limitations of the optical lithography process [Fig. 3.4(c)]. It is a square geometry of 18 turns patterned on 500 μm thick sapphire substrate resulting in a matching network with a 522 MHz resonance frequency. The square bonding pads are 200 μm × 200 μm, about four times the area of the Xue et al. design. This larger area is chosen to allow for two wire bonds per pad. The inductor is fixed in place beside the quantum dot device chip using GE varnish as shown in Fig. 3.6(d). Aluminum wire bonds (25 μm diameter) are used to connect the inductor to both the ohmic contact of the device and the high bandwidth gold pin (O4) of the sample holder. To create an rf ground, the ohmic contact on the other side of the QPC is connected to one of the plates of a 16 pF, NPO dielectric capacitor (American Technical Ceramics, P/N 116YCA160D100TT) using 25 μm diameter, gold wire bonds. The other plate is connected to the gold ground plane using silver epoxy (EPO-TEK H20E). This capacitor, also shown schematically in Fig 3.1(d), presents an impedance of 19 Ω to ground at 522 MHz.

Fig. 3.2(a) displays the S_{11} scattering parameter data for the RLC circuit composed

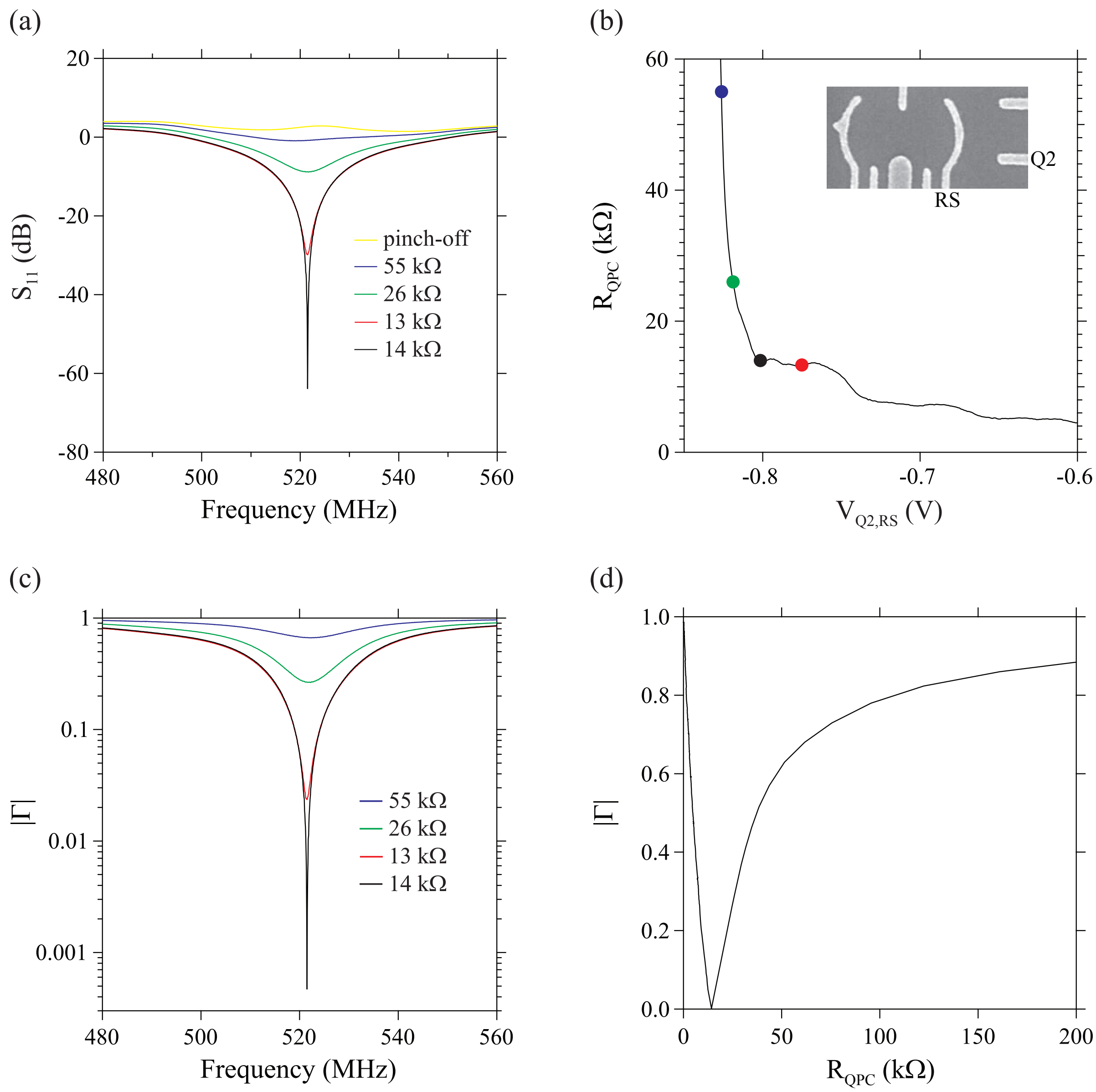

Figure 3.2: (a) S_{11} as a function of frequency for several values of R_{QPC}. (b) R_{QPC} as a function of QPC gate voltage (Q2, RS). Colored dots indicate the resistance values corresponding to the curves in (a) and (c). (c) Reflection coefficient as a function of frequency for several values of R_{QPC}. (d) Reflection coefficient at the resonance frequency as a function of R_{QPC}.

of the lithographic inductor, its parasitic capacitance, and R_{QPC}.[1] The QPC is formed by gates Q2 and RS. Curves for several values of R_{QPC} are displayed. The corresponding points are shown on the plot of R_{QPC} versus (Q2, RS) gate voltage in Fig. 3.2(b). Following Xue et al., the S_{11} curve corresponding to QPC pinch-off (i.e. insulating state) is considered a reference for which $\Gamma = 1$. The difference between each of the curves of Fig. 3.2(a) and this reference produce the curves displayed in Fig. 3.2(c), showing Γ as a function of frequency. At 522 MHz, the minimum in $\Gamma(R_{QPC})$ occurs for $R_{QPC} = 14$ kΩ. Ideally this optimal R_{QPC}, near where $d|\Gamma|/dR_{QPC}$ has a maximum [Fig. 3.2(d)], would occur at the same R_{QPC} that corresponds to the maximum slope of the QPC resistance curve, $dR_{QPC}/dV_{Q2,RS}$. Unfortunately this slope typically has its maximum at a higher resistance, 30-100 kΩ.

Calculation of L and C_p for the current design requires data from one of the curves in Fig. 3.2(c) and the following two equations:

$$L/C_p = R_{QPC} Z_0 (1+\Gamma)/(1-\Gamma) \tag{3.9}$$

$$LC_p = 1/(2\pi f_0)^2 \tag{3.10}$$

Eq. 3.9 is produced by substituting $Z_{in} = L/C_p R_{QPC}$ into $Z_{in} = Z_0(1+\Gamma)/(1-\Gamma)$ and Eq. 3.10 is simply a rearrangement of the expression for the resonance frequency, Eq. 3.2. Extracting $f_0 = 522$ MHz, $\Gamma = 4.7 \times 10^{-4}$, and $R_{QPC} = 14$ kΩ from Fig. 3.2(c), substituting into the above equations, and solving the system produces $L = 255$ nH and $C_p = 0.36$ pF. The inductance, parasitic capacitance, resulting resonance frequency, and circuit bandwidth (measured in Section 3.6) are displayed in Table 3.1 along with values from Reilly et al. [26], Cassidy et al. [27] (copper chip inductors), and Xue et al. [60] (lithographic superconducting inductor). Note that the value of L for the chip inductors is the nominal value, not the value in the context of the matching network.

Several changes to the inductor design could reduce C_p and thus increase the value of R_{QPC} corresponding to optimal match. Decreasing turn spacing, etching the sapphire

[1] Similar to Γ, S_{11} is defined as the amplitude of the reflected voltage wave divided by the amplitude of the incident voltage wave [59]. Following the readout literature, S_{11} is used for the raw reflectometry data.

Table 3.1: Summary of the inductance, capacitance, resonance frequency, and bandwidth of several matching networks.

	This work	Reilly et al [26].	Cassidy et al. [27]	Xue et al. [60]
L	255 nH	820 nH	490 nH	170 nH
C_p	0.36 pF	0.63 pF	0.47 pF	0.17 pF
f_0	522 MHz	220 MHz	332 MHz	942 MHz
BW	15 MHz	8 MHz	21 MHz	50 MHz

between turns, and moving the inductor onto the device chip (eliminating the stray capacitance of the wire bonds) may lower C_p. Perhaps machining away the portion of the ground plane where the inductor is to be placed would also lower C_p.

As noted above, one of the advantages of superconducting inductors is their low loss relative to normal metal coils. Losses in a matching network are evaluated by performing a reflection measurement with the QPC in the pinch-off state. Note that rf power incident on the RLC circuit is either absorbed by the QPC (K), reflected back to the source ($|\Gamma|^2$) or dissipated in the matching network (N). Normalizing to the incident signal power, this conservation of energy relationship produces the following equation:

$$|\Gamma|^2 + K + N = 1$$

In the pinch-off regime, no power is absorbed by the QPC and thus $K = 0$. All incident power is either absorbed by the matching network or reflected back to the source. The data in Fig. 3.2(a) reveals that there is no dip in S_{11} at the 522 MHz resonance frequency with the QPC in the pinch-off state. All of the power is reflected back to the source ($\Gamma = 1$). No power is dissipated in the matching network ($N = 0$). If instead of a superconducting inductor, a copper chip inductor is employed, a dip at the resonance frequency is typically observed with the QPC in the pinch-off regime. The data from Reilly et al. [26] shown in Fig. 3.3(a), for example, reveals a ~20 dB deep dip at the 220 MHz resonance frequency for the pinch-off case ($g_{QPC} = 0$). This 20 dB return loss implies $|\Gamma| = 0.1$ and $|\Gamma|^2 = 0.01$.[2] Only 1% of the power is reflected while the other 99% is dissipated in the matching network.

[2]Return loss in decibels is $RL(dB) = -20\log_{10}|\Gamma|$.

The data from Cassidy et al. [27] is displayed in (b), showing a 15 dB dip with the QPC in the pinch-off regime.

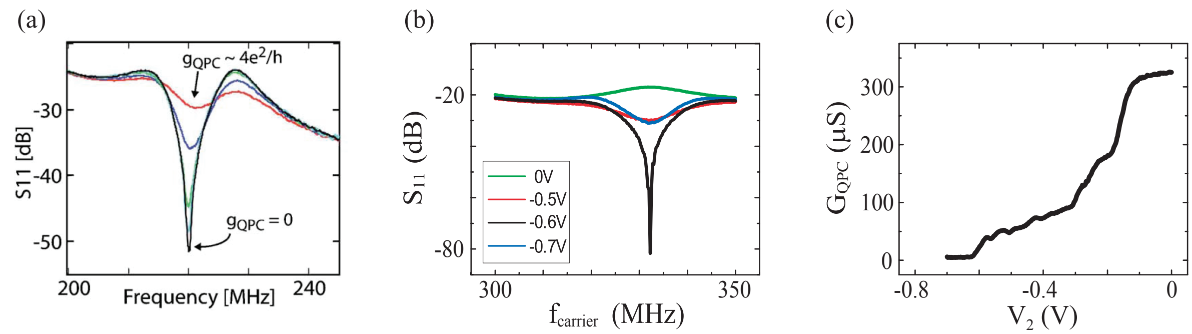

Figure 3.3: S_{11} versus frequency data from (a) Reilly et al. [26] and (b) Cassidy et al. [27]. (c) Conductance curve for the QPC described in Ref. [27]. At the resonance frequency, the curves in (b) from top to bottom correspond to G_{QPC} values of 325, 50, 0, and 30 μS (i.e. 3 kΩ, 20 kΩ, > 1 MΩ, and 33 kΩ). Reprinted from Applied Physics Letters **91**, 162101 (2007) and Applied Physics Letters **91**, 222104 (2007), with the permission of AIP Publishing.

The planar niobium spiral inductor is fabricated by optical lithography. Square pieces (2.5 cm $\times$ 2.5 cm) of 500 μm thick sapphire substrate (Valley Design Corporation) are cleaned in baths of acetone, isopropanol, and deionized water using an ultrasonic cleaner. Baking in a convection oven at 180 °C for 30 minutes dehydrates the substrate. To simplify the lift-off process, the double layer resist technique, shown schematically in Fig. 3.4(a), is employed. A 500 nm thick lift-off resist layer (Microchem LOR 5A) is spun onto the substrate (5000 RPM for 30 seconds) and baked at 180 °C for 15 minutes. After the substrate cools to room temperature, a 1.3 μm thick layer of photoresist (Shipley 1813) is spun (5000 RPM for 30 seconds) on top of the lift-off resist and baked for 30 minutes at 115 °C. This photoresist layer is exposed for 6 s using a Karl Suss MJB3 mask aligner, developed in MF-319, washed in deionized water, and finally blown dry using nitrogen gas. The development time varies but is typically a few minutes. Fig. 3.4(b) shows a false color photograph of the exposed substrate and remaining resist layers at this stage in the process. The bright borders indicate that the lift-off resist has dissolved at the edges of the exposed regions creating an undercut [Fig. 3.4(a)]. A 180 nm niobium film

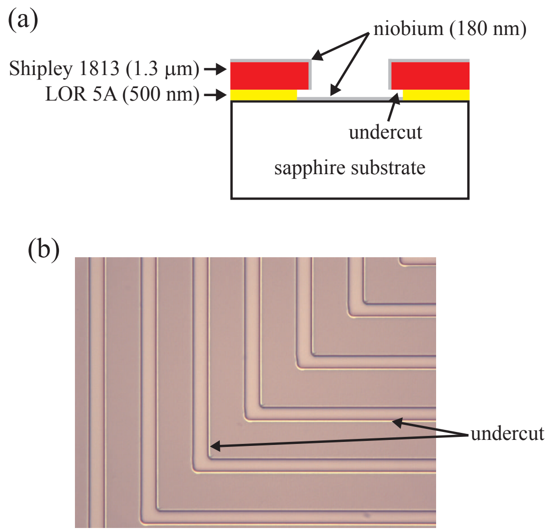

Figure 3.4: (a) Schematic cross-section after the niobium sputtering process. Proper choice of development time creates the desired undercut below the photoresist layer. (b) False color microscope image of the resist after the development process. This case of slight over development clearly shows the undercut regions (bright borders). (c) An example of a niobium inductor after the lift-off process.

is now sputtered onto the exposed sapphire (DC sputter, 280 V, 0.5 A, 2 minutes). The resist lift-off process involves immersing the sample is a 65-70 ˚C bath of Nano Remover PG. The niobium covered resist is removed within a few minutes. The sample is rinsed in isopropanol and deionized water and blown dry using nitrogen gas. Fig. 3.4(c) shows the inductor after sputtering and lift-off. A layer of photoresist is then spun onto the niobium inductor to protect it during the wafer dicing process. A 2 mm × 2 mm square chip containing the inductor is cut using a dicing saw. The chip is immersed in acetone to remove the photoresist, rinsed in deionized water, blown dry, and finally glued beside the DQD device chip.

3.3 Readout Circuit

The RF-QPC reflectometry circuit is shown in Fig. 3.5. A 520 MHz carrier sine wave is produced by a signal generator (Agilent E8241A) and launched towards the device via semi-rigid coaxial cables. For both the input and output rf lines, copper coaxial cables are employed at room temperature, beryllium copper to the 1 K pot, superconducting niobium titanium from the 1 K pot to the mixing chamber and finally copper to the device. They run beside the high bandwidth gate coaxial cables and are heat sunk similarly (Section 2.5). To absorb thermal noise produced at higher temperatures, the input line contains 20 dB attenuators (XMA, P/N 2082-6418-20) heat sunk to the 1 K pot and the still plate. A 145 MHz cutoff, high-pass filter (Mini-Circuits, model VHF-145) is located at the 1 K pot stage to attenuate instrumentation noise, in particular 60 Hz harmonics [Fig. 3.6(a)]. At base temperature, the carrier signal and input noise is further attenuated by 30 dB in a directional coupler (S.M. Electronics[3], model MC3202-30) and sent via a homemade bias tee to the device. The bias tee consists of a 51 pF, NPO dielectric capacitor (American Technical Ceramics, 700A series) and a 1.2 μH conical inductor (Coilcraft, model BCS-122JL). The directional coupler and bias tee are shown heat sunk to the mixing chamber plate in Fig. 3.6(c). Copper coax connects the output of the bias tee to the MCX jack on the right side of the NRC sample holder shown in Fig. 3.6(d).

A room temperature measurement of the input line attenuation to the end of the bias tee is displayed in Fig. 3.7(a). The fixed attenuators and directional coupler collectively contribute 70 dB at 520 MHz. The 5.5 m copper coax (UT-141) in the room and the 1.5 m beryllium copper line (UT-85, silvered inner conductor) to the 1 K pot together contribute another 2 dB. The remaining 3 dB of attenuation is due to filters and coax at and below the 1 K pot stage.

Depending on the DQD charge state, some fraction of the carrier signal is reflected from the *RLC* circuit formed by the matching network and QPC resistance. This signal passes through the bias tee and directional coupler ($<$ 1 dB insertion loss) to the input of a μ-metal shielded circulator mounted on the mixing chamber as shown in Fig. 3.6(b). The circulator is a non-reciprocal device that allows signals reflected by the *RLC* circuit

[3] Fairview Microwave

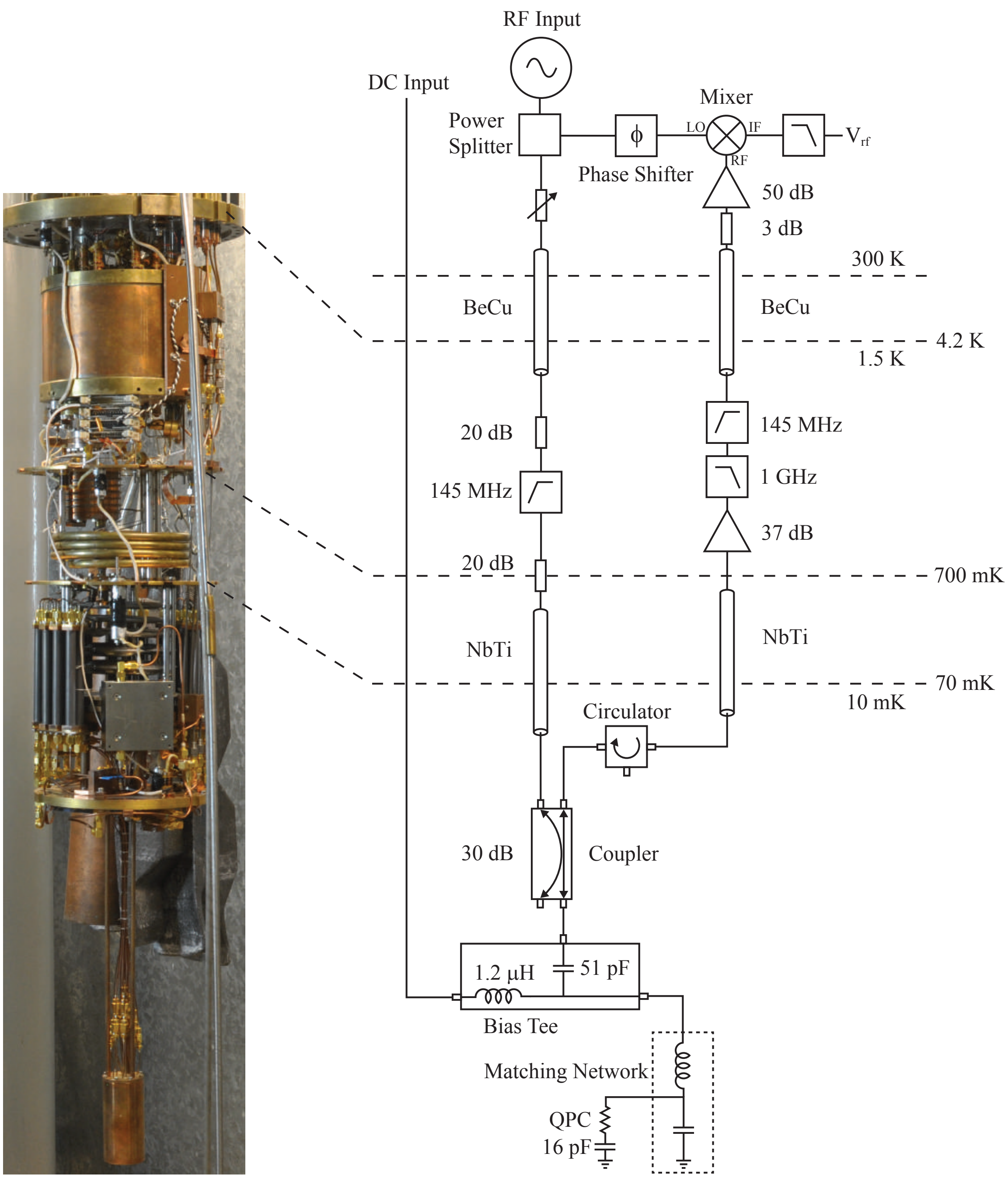

Figure 3.5: RF-QPC readout circuit on the Oxford 600 dilution refrigerator.

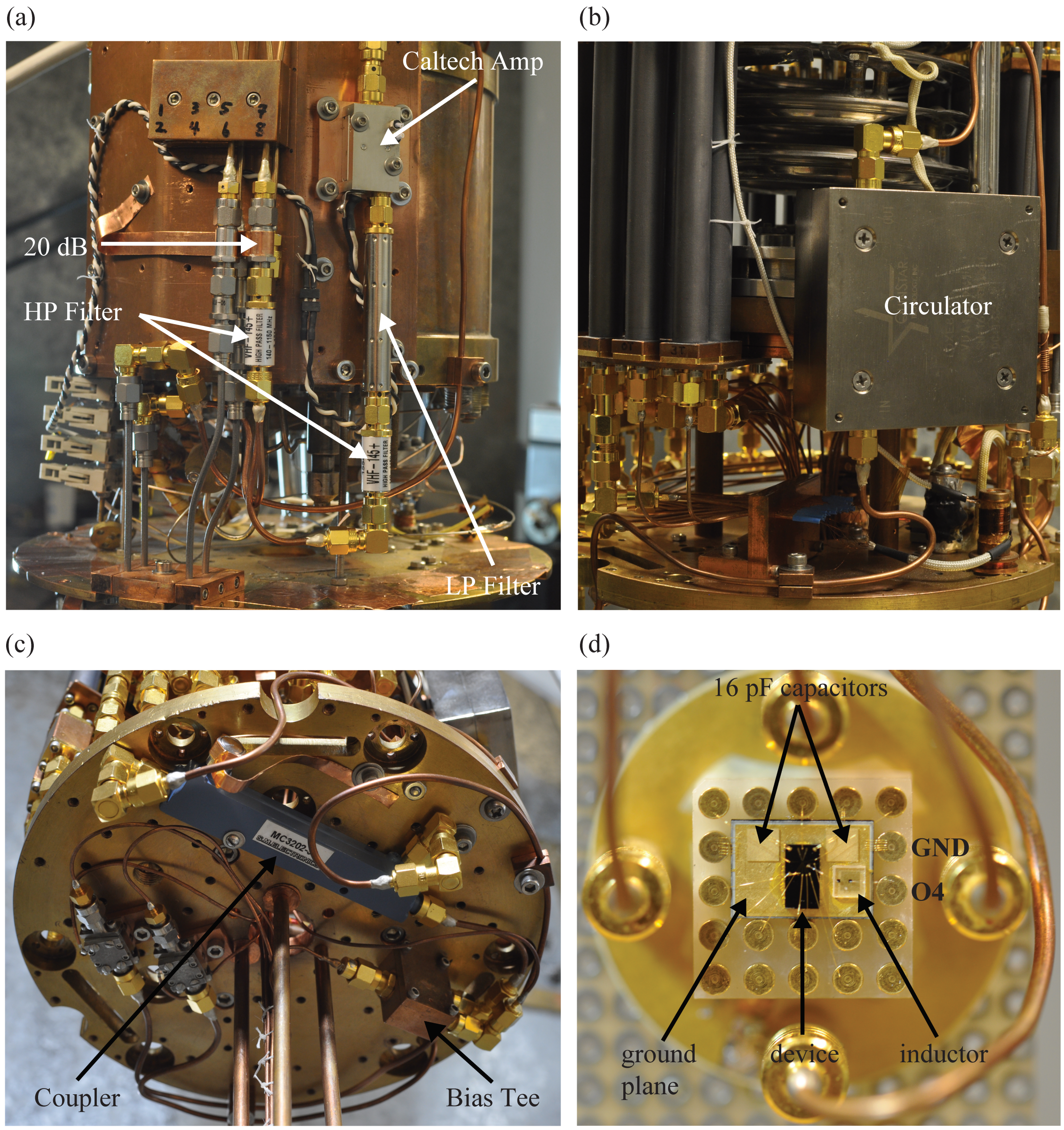

Figure 3.6: (a) Components on the 1 K pot. Input line attenuator and filter; output line filters and Caltech amplifier. (b) Circulator connected to the mixing chamber. (c) Directional coupler and homemade bias tee on mixing chamber plate. (d) Niobium inductor mounted beside the DQD device chip.

to pass essentially unattenuated (insertion loss ≈ 1 dB) to the the input of the cryogenic low noise amplifier (LNA). Signals traveling in the opposite direction, however, are attenuated by approximately 20 dB. Noise produced by the cryogenic LNA is therefore strongly attenuated before reaching the DQD device. The specifications sheet for the circulator (Quinstar, model VDA1129KIS) lists 1 dB maximum insertion loss and 20 dB minimum isolation in a 450-550 MHz frequency range (measured at 2 K). Fig. 3.7(b) shows network analyzer measurements of the circulator on a pulse tube refrigerator at 2.8 K.

Made in the Sander Weinreb group at Caltech, the cryogenic LNA is based on SiGe field effect transistors. According to the specification sheet, the amplifier has a noise temperature of 2.3 K and a gain of 37 dB at 520 MHz. This cryogenic LNA is mounted to the 1 K pot (1.5 K) as shown in Fig. 3.6(a) and followed by an amplifier stage located at the top of the fridge (i.e. inside the screen room). The room temperature post amplifier has a gain of 50 dB and a noise temperature of 50.7 K in the 0.1-1 GHz frequency range (Miteq, model AMF-3F-00100100-07-10P).[4] A 145 MHz cutoff high-pass filter and a 1350 MHz low-pass filter are placed at the 1 K pot stage between the two amplifiers (Mini-Circuits, models VHF-145 and VLFX-1350). They are shown in Fig. 3.6(a). Together they form a band-pass filter that reflects noise produced by the Miteq amplifier and other room temperature instrumentation that would otherwise feed through the Caltech amplifier (i.e. output to input) and down to the device. Fig. 3.7(c) and (d) show transmission as a function frequency for these filters measured in a helium dewar at 4.2 K.

To extract the envelope of the reflected signal, a homodyne receiver is employed. The output of the Miteq amplifier is connected to the RF input of a mixer (Macom, model M2BC). Using a power splitter (Mini-Circuits, model ZFSC-2-5-S+), the required +13 dBm, 520 MHz linear oscillator (LO) signal is produced by the same signal generator used to create the original carrier signal. In addition to the envelope, the intermediate frequency (IF) output of the mixer also contains several components around 2×520 MHz = 1040 MHz. These components are filtered away using a Mini-Circuits low-pass filter. Between the splitter and the LO input of the mixer is placed a passive phase shifter in the form of an adjustable line (874-LA). The phase difference between the RF and LO signals is tuned by changing the length of this line until a maximum envelope signal amplitude is achieved.

[4] Occasionally replaced by two Mini-Circuits ZRL-700+ amplifiers (gain = 60 dB, noise T = 170 K)

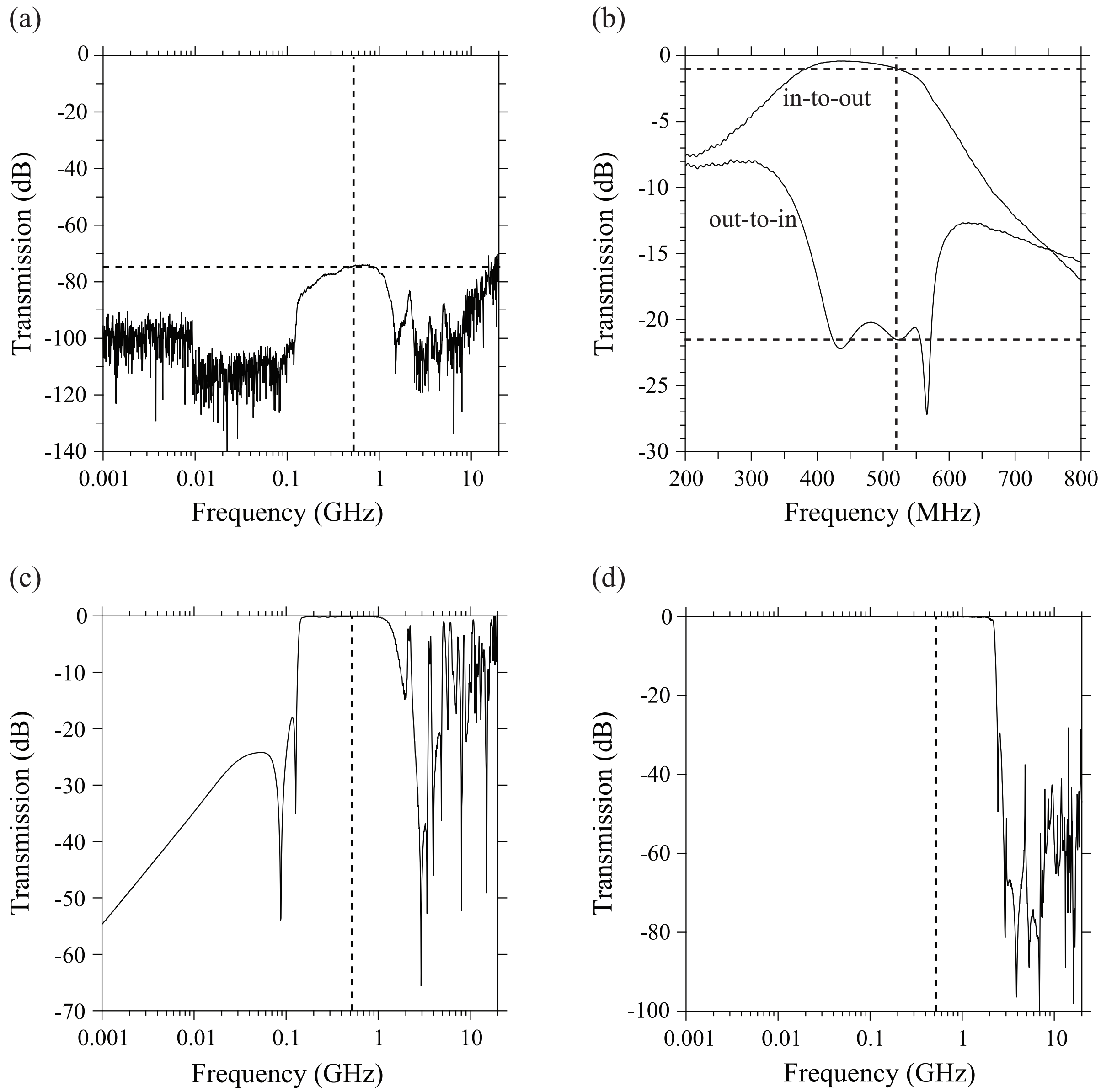

Figure 3.7: (a) Transmission of the RF-QPC circuit input line measured at room temperature. (b) Frequency response of the circulator measured at 2.8 K. (c)[(d)] Transmission of Mini-Circuits VHF-145 high-pass [VLFX-1350 low-pass] filter measured at 4.2 K.

3.4 Noise Temperature

In addition to amplifying both the signal and noise at their input, each amplifier stage also contributes noise and thus degrades the signal-to-noise ratio. The amplifier stages are the dominant noise sources and thus in part determine the sensitivity of the readout. The ultimate goal of this section is to characterize the noise of the RF-QPC readout.

3.4.1 Noise Temperature Definition

Noise temperature is a convenient metric for characterizing an amplifier that produces white (i.e. frequency independent) noise. Its definition is based on modeling the amplifier, for noise analysis purposes, as a resistor producing thermal noise. Recall that the rms voltage noise produced by a resistor R at temperature T in a bandwidth B is $v_n = \sqrt{4k_BTBR}$. It is sometimes convenient to replace R by a circuit composed of a noiseless resistor R and a voltage source v_n. This equivalent circuit is shown connected to a matched load R in Fig. 3.8. The noise current is $i_n = v_n/2R$ and the noise power delivered to the load resistor is therefore $P_n = i_n^2 R = k_BTB$.

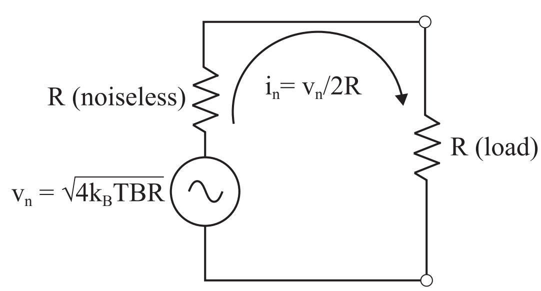

Figure 3.8: For noise analysis, the Thévenin equivalent circuit of a resistor R consists of a source producing an rms voltage $v_n = \sqrt{4k_BTBR}$ in series with a noiseless resistor R.

Consider the situation depicted in Fig. 3.9(a) which shows an amplifier of power gain A with source and load resistors R at temperature T. The total noise power delivered to the load resistor is $P_a = Ak_BTB + N_A$. It is composed of the noise from the source resistor amplified by the gain A and the noise power added by the amplifier itself, N_A. Now consider two special cases of this setup shown in (b) and (c). In part (b), the source resistor is at the hypothetical temperature $T = 0\ K$ and the noise power P_b delivered to the load is N_A. In part (c), the amplifier is considered noiseless and the output noise, $P_c = Ak_BTB$, is the amplified thermal noise of the source resistor. Now note that if the temperature of the source resistor in (c) is set to $T_e = N_A / Ak_BB$, then $P_c = P_b = N_A$. That is, the source resistor in (c) at temperature T_e produces the same noise as the amplifier in (b). This scenario is shown in (d). The amplifier can thus be modeled as a resistor R at temperature T_e, called the equivalent noise temperature and the total noise power in (a) can be written as $P_a = Ak_B(T + T_e)B$.

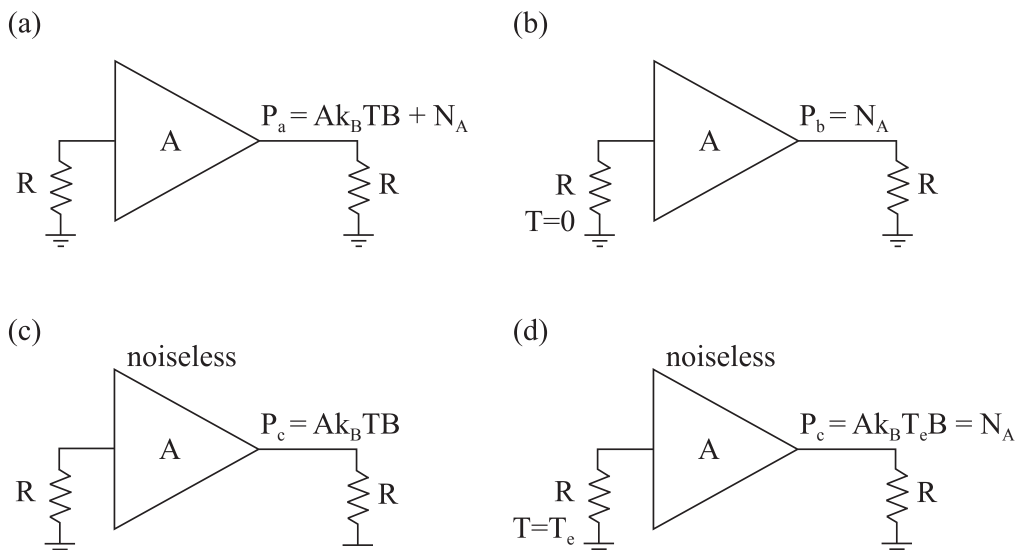

Figure 3.9: Schematics used to explain the concept of noise temperature.

3.4.2 Noise Temperature of an Amplifier Cascade

The readout contains two semiconductor amplifier stages. It also contains several lossy components between the device and the cryogenic amplifier that are collectively treated as an amplifier with gain $A < 1$ (Section 3.4.3). An expression for the noise temperature of such a cascade of three amplifier stages is derived in this section. Consider the schematic of Fig. 3.10 which shows three stages with gains A_1, A_2, A_3 and noise temperatures T_{n1}, T_{n2}, T_{n3} connected to matched source and load resistors R at temperature T. The problem is divided into pieces by calculating the noise powers P_{n1}, P_{n2}, and P_{n3} at the outputs of the corresponding stages. The noise at the output of the first stage is the amplified noise of the source resistor added to the noise power contributed by the first stage amplifier

$$P_{n1} = A_1 k_B T B + A_1 k_B T_{n1} B = A_1 k_B (T_s + T_{n1}) B.$$

Multiply this by A_2 and add the noise contributed by the second amplifier to produce an expression for the noise power at the output of the second stage

$$P_{n2} = A_2 P_{n1} + A_2 k_B T_{n2} B = A_1 A_2 k_B (T + T_{n1}) B + A_2 k_B T_{n2} B.$$

Combining the first two amplifiers into one stage of gain $A_1 A_2$ and noise temperature T_{n12} gives the alternative expression

$$P_{n2} = A_1 A_2 k_B (T + T_{n12}) B.$$

Equating these two expressions for P_{n2} gives

$$T_{n12} = T_{n1} + \frac{T_{n2}}{A_1}.$$

Following similar arguments, the noise power at the output of the third stage is given by

$$P_{n3} = A_3 P_{n2} + A_3 k_B T_{n3} B = A_1 A_2 A_3 k_B (T + T_{n12}) B + A_3 k_B T_{n3} B$$

or combining the three amplifiers into a single stage of noise temperature T_{n123}

$$P_{n3} = A_1 A_2 A_3 k_B (T + T_{n123}).$$

Equating these expressions gives the final expression for the noise temperature of the cascade of three amplifiers

$$T_{n123} = T_{n1} + \frac{T_{n2}}{A_1} + \frac{T_{n3}}{A_1 A_2}.$$

Note that if the gain of the first stage is sufficiently large, the system noise temperature will be dominated by the noise temperature of the first stage.

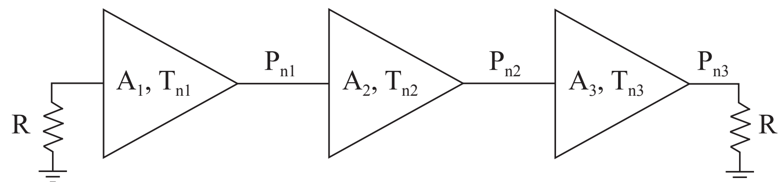

Figure 3.10: A cascade of three amplifier stages with gains A_1, A_2, A_3 and noise temperatures T_{n1}, T_{n2}, T_{n3}. The noise power delivered to the load resistor consists of the amplified noise of the source resistor and the noise added by each amplifier stage.

3.4.3 Noise Temperature of a Lossy Transmission Line

Between the device and the cryogenic amplifier, there is a directional coupler, bias tee, circulator, and approximately one meter of coaxial cable. For the purposes of noise analysis, they are collectively viewed as a lossy transmission line that forms the first stage in the cascade described above. Calculate the noise temperature of the lossy line by modeling it as an amplifier with gain $A < 1$ [59]. Fig. 3.11(a) shows a lossy line terminated with matched source and load resistors R.

Because the characteristic impedance of the line is $Z_0 = R$, the line and source resistor collectively look like a resistor R when looking into the circuit from the load side. The noise power delivered to the load resistor is therefore $P_n = k_B T B$. Equivalently the noise contributions of the source resistor and the line can be taken separately. Similar to the arguments associated with the amplifier cascade, the output noise can be viewed as the attenuated noise of the source resistor added to the contribution of the line itself. Calling

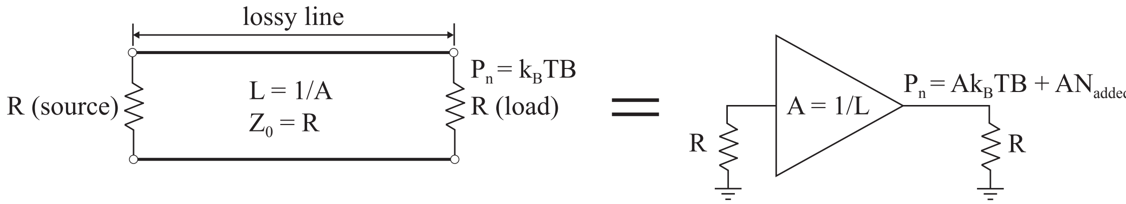

Figure 3.11: A source resistor delivers noise power to a load resistor via a matched, lossy transmission line. The equivalent noise temperature of the lossy line is $(L-1)T$, where L is its linear loss factor.

this latter contribution N_{added}, gives $P_n = Ak_BTB + AN_{added}$, where N_{added} is referred to the input of the line. Equating the two expressions for P_n shows that

$$N_{added} = \frac{1-A}{A}k_BTB = (L-1)k_BTB,$$

where the loss factor L is defined as $L = 1/A$. The noise temperature of the lossy line is therefore

$$T_e = \frac{N_{added}}{k_BB} = (L-1)T.$$

3.4.4 RF-QPC Noise Temperature Measurement

This section describes how a shot noise measurement is used to evaluate the readout noise temperature [27, 61]. Recall the well known Schottky expression for the spectral density of shot noise [62]

$$S_I^c = 2eI.$$

This classical result describes fluctuations in the flow of electrons between a source and drain lead due to a sample which randomly transmits/reflects electrons. It is derived under the assumptions that the flow of electrons is uncorrelated and the tunneling attempts at the sample are independent events (Poissonian statistics). In the quantum treatment of Martin and Landauer, the leads are described by Fermi-Dirac distributions and the electrons are modeled as wavepackets occupied according to the Pauli principle [63]. In the specific case of a QPC sample with conductance, $G = \mathcal{T}G_Q$, between pinch-off and the first plateau ($0 \le \mathcal{T} \le 1$), the spectral density takes the following form at $T = 0$ [64, 65]

$$S_I^q(T=0) = 2eI(1-\mathcal{T}). \tag{3.11}$$

The Fermi-Dirac statistics correlates the flow of electrons and as a result suppresses the shot noise relative to the Poissonian value. The noise in this case is called subpoissonian and is characterized by the Fano factor $\eta = S_I^q(T=0)/S_I^c = 1-\mathcal{T}$. Generalizing the quantum result to also include the noise associated with the emission of electrons from the leads at finite temperature, the spectral density of shot noise is given by

$$S_I^q(T) = 2eI(1-\mathcal{T})\left[\coth\left(\frac{eV_{SD}}{2k_BT}\right) - \frac{2k_BT}{eV_{SD}}\right], \tag{3.12}$$

where V_{SD} is the voltage bias applied between the source and drain leads [66, 67].

To measure the system noise temperature, the readout is used to measure the shot noise of the QPC as function of V_{SD}. The noise power of the readout before the detection circuit (i.e. mixer) is given by

$$P = ABk_B(T_N + T_{QPC}), \tag{3.13}$$

where A is the system gain (DQD device to mixer input) and B is bandwidth. The readout noise temperature, T_N, characterizes the noise contributions of both semiconductor amplifiers and the passive components including the coaxial cables, circulator, directional coupler, and bias tee. The shot noise associated with the QPC is characterized by the noise temperature T_{QPC}. To produce an expression for T_{QPC}, note that the thermal noise of a resistor of conductance G at temperature T is described by the spectral density $S_I^{th} = 4k_BTG$. This motivates a definition of noise temperature $T_{QPC} = S_I/4Gk_B$, where S_I is given by Eq. 3.12. Kumar et al. note that for $eV_{SD}/2k_B \gg T$, the shot noise power varies linearly with V_{SD} and noise temperature is given by $T_{QPC} = \eta eV_{SD}/2k_B$ [66]. Substitute this expression into Eq. 3.13 and rearrange the terms to produce an expression for noise power in a unit bandwidth [27]

$$P/B = Ak_BT_N + \frac{1}{2}e\eta A|V_{SD}|. \tag{3.14}$$

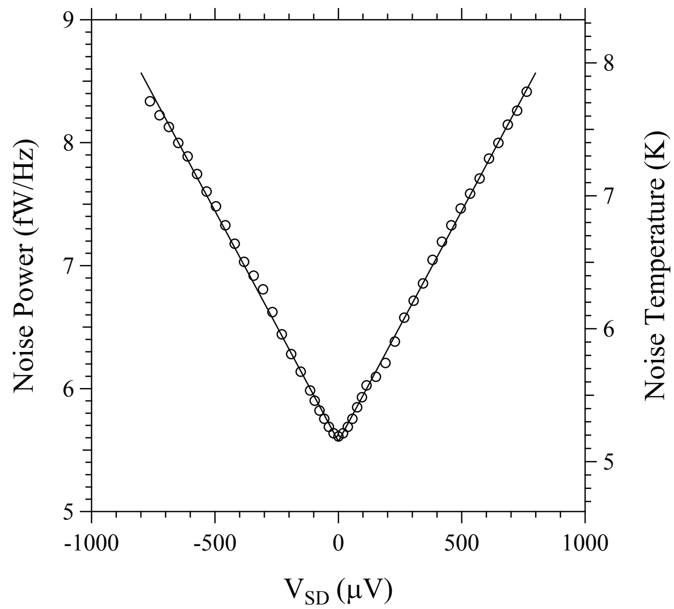

Figure 3.12: Noise power per unit bandwidth measured at the output of the room temperature Miteq amplifier stage as a function of the DC voltage applied across the QPC. The QPC conductance is set to $0.4 \times 2e^2/h$. Open circles are data points, solid lines show a $y = b + a|x|$ fit to the data. The extracted slope and intercept give a system noise temperature of 5.2 K (i.e. at $V_{SD} = 0$).

Measurements of P/B at the readout resonance frequency for positive and negative values of V_{SD} (hence the absolute value) are performed using a spectrum analyzer and displayed in Fig. 3.12. Note that Eq. 3.14 has the form $y = b + a|x|$, where $y = P/B$, $|x| = |V_{SD}|$, the intercept is $b = Ak_BT_N$, and the slope is $a = \frac{1}{2}e\eta A$. A curve fit to the data (solid black lines), gives $a = 3.76 \times 10^{-12}$ and $b = 5.57 \times 10^{-15}$. With a QPC conductance of $G = 0.4G_Q$, $\eta = 1 - \mathcal{T} = 0.6$, and the slope gives $A = 7.83 \times 10^7$. This corresponds to 79 dB gain as expected from the following collection of components: room temperature Miteq amplifier (50 dB), cryogenic Caltech amplifier (37 dB), fixed attenutor on Miteq input (−3 dB), beryllium copper and copper coax of the output line (−2 dB), coax and passive rf components on the fridge (−3 dB). Using the value of A calculated from the fit, the intercept yields the noise temperature $T_N = 5.2$ K (right-axis of Fig. 3.12).

Viewing the readout as composed of a three stage amplifier cascade, a value for T_N can be calculated using the following expression:

$$T_N = (L-1)T + LT_{n2} + \frac{LT_{n3}}{A_2}. \tag{3.15}$$

The first stage is due to the attenuation of the passive components between the QPC and the cryogenic amplifier. This attenuation has a linear loss factor $L = 1.58$ (2 dB). The second stage is the cryogenic amplifier. For 23 K ambient temperature and 2.5 V supply voltage, this Caltech CITLF2 SiGe amplifier has a noise temperature of $T_{n2} =$ 2.3 K and a gain $A_2 = 5012$ (37 dB) at 520 MHz (from specification sheet). The Miteq room temperature amplifier with a noise temperature of $T_{n3} = 50.7$ K is the third stage. Substituting these values into Eq. 3.15 gives $T_N = 3.6$ K. This is a lower bound because the first term of Eq. 3.15 is ignored. The higher T_N acquired from the shot noise measurement may also be due to the potentially noisy supplies used to power the amplifiers. Eventually these supplies are replaced with voltage regulators and batteries.

3.5 Sensitivity Theory

Roschier et al. analyze the RF-SET readout and produce an expression for sensitivity which is also applicable to the RF-QPC case [58]. A review of their derivation, using similar notation, is performed in this section. Fig. 3.13 shows the rf source, homodyne detection circuit, and the associated signals at several stages. A carrier signal $s_c = v_0 \cos(\omega_0 t)$, shown at the output of the source, is launched towards the QPC. Depending on R_{QPC}, some fraction of this voltage wave is reflected and becomes the input signal to the detection circuit (i.e. mixer). With the QPC in an initially static electric field environment, this reflected voltage wave is simply $v_0 \Gamma_0 \cos(\omega_0 t)$, where $\Gamma = \Gamma_0$ is the reflection coefficient at the value of R_{QPC} chosen to maximize readout sensitivity. Choice of this optimal working point is related to a combination of two factors: the sensitivity of Γ to changes in R_{QPC} and the sensitivity of R_{QPC} to changes in electric field. Consider now the effect of a sinusoidal oscillation of electric field at the QPC produced by a voltage oscillation on a gate. The resulting oscillation in the reflection coefficient, $\Gamma_m(t) = \Delta\Gamma \cos(\omega_m t)$, about the working point Γ_0 gives a new total reflection coefficient of $\Gamma(t) = \Gamma_0 + \Gamma_m(t)$ and the following form for the amplitude modulated reflected signal $[\Gamma(t) \times s_c]$:

$$s_{RF} = v_0[\Gamma_0 + \Delta\Gamma \cos(\omega_m t)] \cos(\omega_0 t).$$

The product of cosines is converted to a sum of cosines using the trigonometric identity $\cos(A + B) + \cos(A - B) = 2 \cos A \cos B$ and the reflected signal becomes

$$s_{RF} = v_0\Gamma_0\left\{\cos(\omega_0 t) + \frac{\Delta\Gamma}{2\Gamma_0}\{\cos[(\omega_0 - \omega_m)t] + \cos[(\omega_0 + \omega_m)t]\}\right\}. \tag{3.16}$$

An example spectrum of such a signal is shown at the RF input to the mixer in Fig. 3.13. The peak at 519.3 MHz (ω_0) is the carrier. The amplitude modulation produced by a 1 $\mathrm{mV_{rms}}$, 1 MHz oscillation on right plunger gate RP gives the sidebands at frequencies 518.3 MHz ($\omega_0 - \omega_m$) and 520.3 MHz ($\omega_0 + \omega_m$).

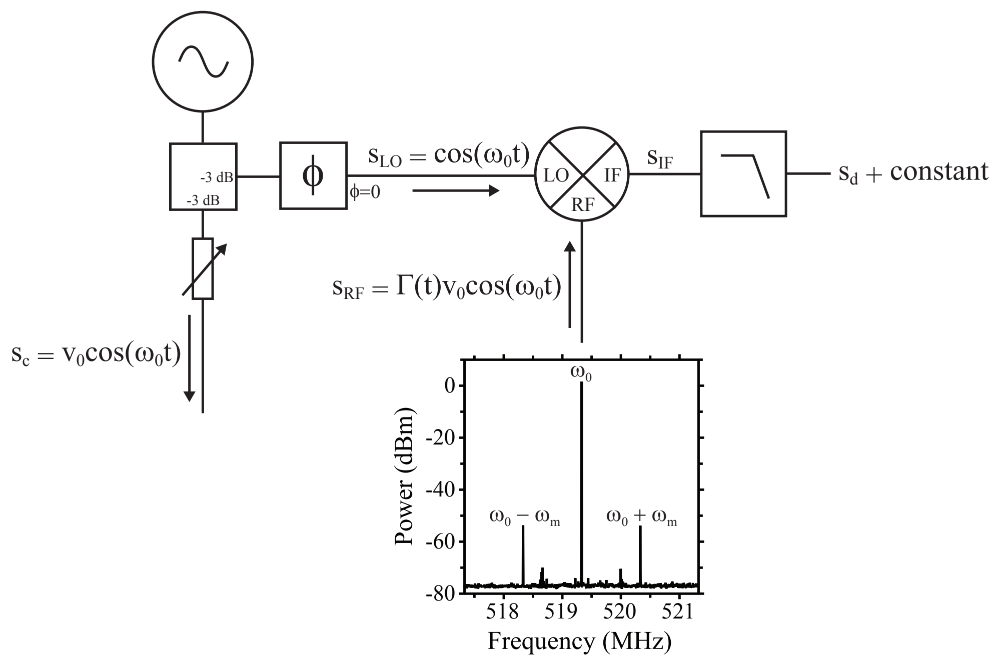

Figure 3.13: RF source and amplitude demodulation (i.e. detection) circuit of the RF-QPC readout.

Amplitude demodulation of the reflected signal is performed with the mixer and the low-pass filter. The mixer multiplies the reflected signal by the LO signal, $s_{LO} = \cos(\omega_0 t)$, to produce, using the above mentioned trigonometric identity, the following result at the IF port:

$$s_{IF} = v_0\Gamma_0\left\{\frac{1}{2}[\cos(2\omega_0 t) + 1] + \frac{\Delta\Gamma}{4\Gamma_0}\{\cos[(2\omega_0 - \omega_m)t] + \cos(-\omega_m t) \right.$$
$$\left. + \cos[(2\omega_0 + \omega_m)t] + \cos(\omega_m t)\}\right\}.$$

If $\omega_m \ll \omega_0$, a low-pass filter can be chosen to eliminate the $2\omega_0$, $2\omega_0 - \omega_m$, and $2\omega_0 + \omega_m$ terms leaving a constant and the ω_m terms. Eliminating the constant with a differential post amplifier leaves the following signal at the output of the detection circuit:

$$s_d = v_0\frac{\Delta\Gamma}{2}\cos(\omega_m t).$$

The root-mean-square (rms) signal is given by

$$\sqrt{S_d} = \sqrt{\langle s_d^2\rangle} = \sqrt{v_0^2\frac{\Delta\Gamma^2}{4} \times \frac{1}{T}\int_0^T dt\cos^2(\omega_m t)} = v_0\frac{\Delta\Gamma}{\sqrt{8}}. \tag{3.17}$$

Development of an expression for readout sensitivity requires a calculation of the system signal-to-noise ratio. A noise theory for the readout begins with the introduction of a voltage noise term, $n(t)$, added to the amplitude modulated signal, s_{RF} (Eq. 3.16), at the RF input to the mixer. In the mixer, $n(t)$ is multiplied by the LO signal to produce the following noise expression at the IF port:

$$y(t) = n(t)\cos(\omega_0 t). \tag{3.18}$$

Comparison of noise with signal requires calculating the power spectral density of $y(t)$, $S_y(\omega)$. Because $y(t)$ and $n(t)$ are related by Eq. 3.18, S_y is related to the power spectral density of voltage fluctuations associated with $n(t)$, S_V. Haykin in Ref. [68] performs a calculation that reveals the relationship between these two spectral densities

$$S_y(\omega) = \frac{1}{4}[S_V(\omega - \omega_0) + S_V(\omega - \omega_0)]. \tag{3.19}$$

The system noise includes contributions from thermal noise, instrumentation noise, and gate voltage noise but is typically dominated by the noise of the cryogenic amplifier. As explained is Section 3.4, these sources are collectively characterized by a noise temperature $T_N = P_n/k_B B$, where P_n is noise power in units of Watts and B is bandwidth in Hz. Very simply, the power spectral density of noise can be written as $P_n/B = S_V/Z_0$, where S_V is in units of V^2/Hz and $Z_0 = 50\ \Omega$ is the impedance of the rf system. Following Roschier et al., combine this definition with the above expression for T_N to produce $S_V = k_B T_N Z_0$. Substitute this frequency independent result into Eq. 3.19 to arrive at an expression for the rms noise in units of $V/\sqrt{\text{Hz}}$

$$\sqrt{S_y} = \sqrt{\frac{k_B T_N Z_0}{2}}. \tag{3.20}$$

Divide Eq. 3.17 by Eq. 3.20 to produce the signal-to-noise ratio in units of $\sqrt{\text{Hz}}$

$$\frac{S}{N} = \sqrt{\frac{S_d}{S_y}} = \frac{v_0 \Delta\Gamma}{\sqrt{4 k_B T_N Z_0}}. \tag{3.21}$$

In order to eliminate $\Delta\Gamma$ from this expression, note that the oscillation of the electric field at the QPC results from varying the charge, q, on the gate. The goal of this sensitivity analysis is to determine how small of a change in gate charge, δq, can be detected by the readout. Since δq produces $\Delta\Gamma$, these parameters have the simple relationship (in rms units)

$$\Delta\Gamma = \sqrt{2}\Delta\Gamma_{rms} = \frac{\partial|\Gamma|}{\partial q}\sqrt{2}\delta q_{rms}.$$

Substituting this result into Eq. 3.21 replaces $\Delta\Gamma$ with charge sensitivity, δq_{rms}. Setting $S/N = 1$, and rearranging produces an expression for charge sensitivity in units of $e/\sqrt{\text{Hz}}$ (remember that S/N has units of $\sqrt{\text{Hz}}$)

$$\delta q_{rms} = \frac{\sqrt{2 k_B T_N Z_0}}{v_0 \dfrac{\partial|\Gamma|}{\partial q}}. \tag{3.22}$$

As a last step, note that some fraction, K, of the incident signal power, $P_i = v_0^2/2Z_0$, is dissipated in the QPC. With the dissipated power being given by $P_{QPC} = v_{QPC}^2/2R_{QPC}$, setting $P_{QPC} = KP_i$ and solving for v_0 produces the expression

$$v_0 = v_{QPC}\sqrt{\frac{Z_0}{R_{QPC}K}},$$

where v_{QPC} is the amplitude of the voltage across the QPC. Substitute this and $\partial|\Gamma|/\partial q = (\partial|\Gamma|/\partial R_{QPC})(\partial R_{QPC}/\partial q)$ into Eq. 3.22 to give the final expression for charge sensitivity

$$\delta q = \frac{\sqrt{2k_B T_N R_{QPC} K}}{v_{QPC}\,\dfrac{\partial|\Gamma|}{\partial R_{QPC}}\,\dfrac{\partial R_{QPC}}{\partial q}} \tag{3.23}$$

where rms units are understood and the corresponding label is dropped. Although the electric field at the QPC is produced by a gate in this model, Eq. 3.23 is equally applicable to the case of an electric field produced by charges on a nearby DQD where δq and the amplitude modulation of the carrier signal ($\Delta\Gamma$) result from electrons moving to/from the leads or between dots.

3.6 Sensitivity and Bandwidth Measurements

Bandwidth and sensitivity measurements of the RF-QPC readout are described in this section. As in the DC-QPC case of Section 1.6, the (Q1, RS) QPC is employed in the rf readout. Tuning for maximum electric field sensitivity involves applying an oscillation (eg. 1 $\mathrm{mV_{rms}}$, 11 Hz) to the left plunger gate LP and measuring the signal at the output of the detection circuit, V_{rf}, with a lock-in amplifier while sweeping V_{Q1}. The maximum lock-in amplifier response and thus highest sensitivity occurs at the value of V_{Q1} corresponding to $R_{QPC} = 70$ kΩ. This working point is indicated by a black circle on the $|\Gamma|$ versus R_{QPC} and R_{QPC} versus V_{Q1} plots shown in Fig. 3.14(a). [5] The working point seems largely determined by $\partial R_{QPC}/\partial V_{Q1}$, as in the DC case, since clearly the maximum in $\partial|\Gamma|/\partial R_{QPC}$ does not occur near $R_{QPC} = 70$ kΩ. Note in particular that $\partial|\Gamma|/\partial R_{QPC} = 2$ μS at $R_{QPC} = 70$

[5] The $|\Gamma| = 1$ reference corresponds to the smallest value of R_{QPC}. A similar convention is followed in most rf readout literature although not by Xue et al. as discussed in Section 3.2 [60].

kΩ while at R_{QPC} = 30 kΩ, the slope increases to 9.5 μS. As discussed in Section 3.2, improvements in sensitivity may be achieved by redesigning the matching network to push the maximum slope to a higher value of R_{QPC}. A carrier power of $P_{\mathrm{rf}} = -85$ dBm at the device is used for the optimization procedure.

After choosing the working point, V_{rf} is measured as V_{LS} is swept along the trajectory indicated by the vertical dashed line in the stability diagram of Fig. 3.14(b). Moving from right to left on the V_{LS} axis of Fig. 3.14(c), an electron is ejected from the right dot at $V_{LS} = -0.633$ V changing the charge state from (2,1) to (2,0) and increasing V_{rf} by 225 μV. An electron is then removed from the left dot at $V_{LS} = -0.644$ V in the transition (2,0)$\rightarrow$(1,0) increasing V_{rf} by another 150 μV. The readout signal is maintained at an approximately constant value in regions of constant DQD charge state by also sweeping V_{Q1} during the V_{LS} sweep. The system noise spectrum measured at the output of the detection circuit is displayed in Fig. 3.14(d). The left vertical axis is in units of $\mu\mathrm{V_{rms}}/\sqrt{\mathrm{Hz}}$ and using 225 μV/e, the right axis shows the noise in units of $e/\sqrt{\mathrm{Hz}}$. The noise floor above 1 kHz is 0.4 $\mu\mathrm{V}/\sqrt{\mathrm{Hz}}$ or 1.8×10^{-3} $e/\sqrt{\mathrm{Hz}}$ (i.e. 0.4/225). Note that the DC offset inherent in the detected signal (Section 3.5) is (mostly) removed using a differential (channel A $-$ channel B) voltage amplifier (PAR 113) and a DC voltage supply. The readout signal is input to channel A and the supply to channel B. The supply voltage is tuned in an attempt to remove the DC offset from the preamplifier output signal so that the following instrument (i.e. voltmeter or oscilloscope) can run in its highest sensitivity range. The remaining -44 mV offset [Fig. 3.14(c)] is thus arbitrary and percent changes in V_{rf} associated with DQD charge state changes are meaningless.

The (Q1, RS) QPC is used in the rf readout because it is closer to where the dots form than the (Q2, RS) QPC. To use the (Q1, RS) QPC, however, requires setting V_{Q2} to approximately -0.25 V (after a +0.25 V bias cooling [69]). If Q2 is left grounded, no change in Γ at the resonance frequency is observed as R_{QPC} is swept from its lowest value to the pinch-off regime. Apparently Q2 acts like an rf ground that is capacitively coupled to the 2DEG. This capacitance is a low impedance for signals at the carrier frequency when Q2 is grounded. This impedance, however, can be increased by depleting the electrons under Q2. Although not investigated in detail, for this particular device, varying V_{Q2} from -0.2 V to -0.3 V allows some tuning of the resonance frequency and $\Gamma(R_{QPC})$, similar

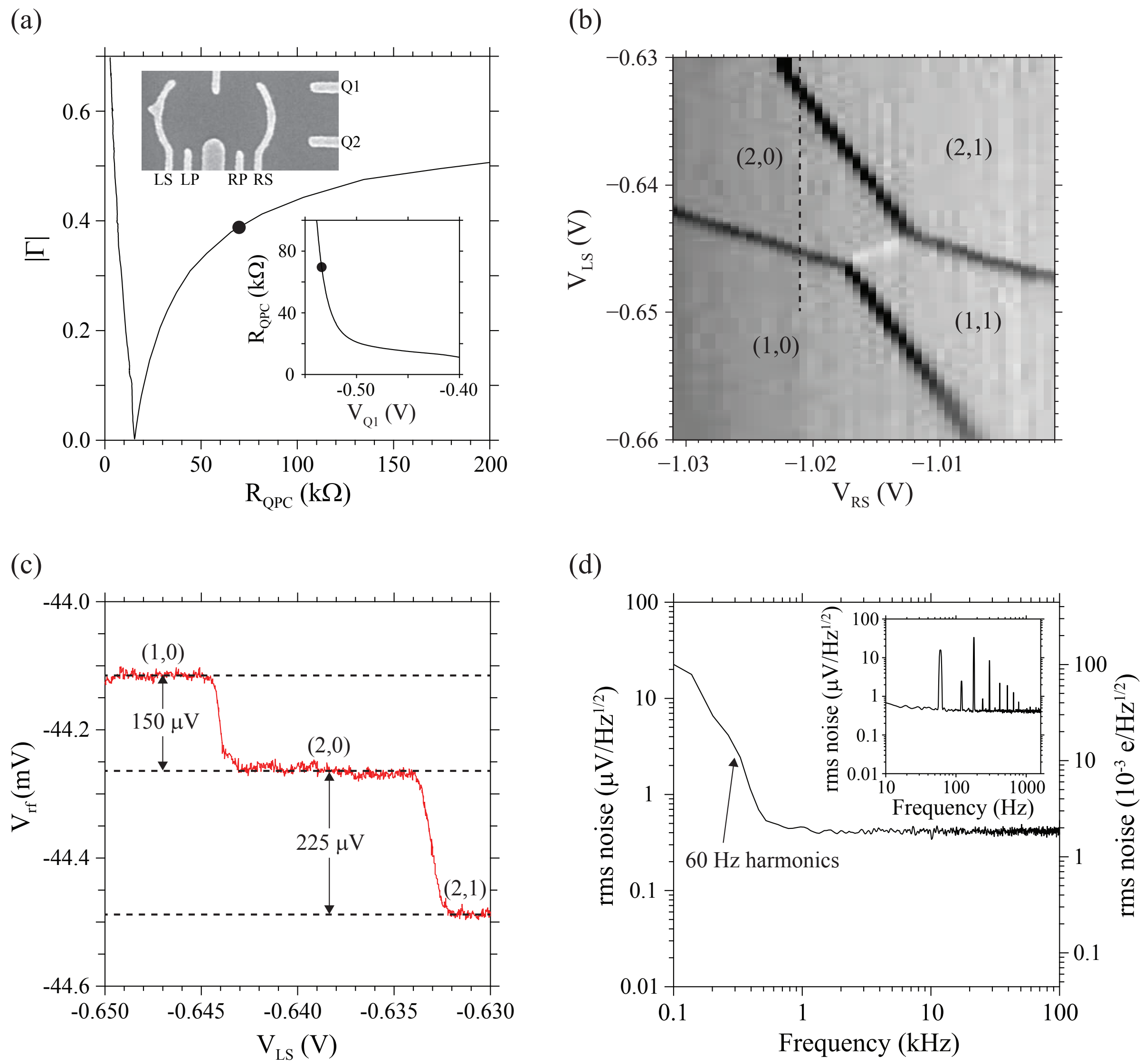

Figure 3.14: (a) $|\Gamma|$ as a function of R_{QPC} with $V_{Q2} = -0.25$ V (black dot indicates the working point). (b) Stability diagram acquired using the RF-QPC. (c) $V_{\rm rf}$ measured along the dashed line in (b); 300 Hz bandwidth set by a PAR 113 voltage amplifier. (d) Voltage noise measured at the output of the detection circuit [right axis = (left axis)÷(225 μV/e)]. Inset: 60 Hz harmonics.

to the use of a varactor diode as a voltage controlled capacitor in the matching network of the ETH group [70]. This capacitance issue is the reason the resonance frequency has varied slightly throughout the chapter, from 519 to 522 MHz. It is also the reason that $|\Gamma|$ approaches approximately 0.5 instead of 1 for large R_{QPC} in Fig. 3.14(a). There is a power divider effect involving the (Q1, RS) QPC and the Q2 gate that was not understood at the time of these measurements. The desired $|\Gamma| \to 1$ behavior described in Section 3.2 can be achieved with proper tuning of Q2.

The RF-QPC bandwidth measurement involves applying a 1 $\mathrm{mV_{rms}}$ oscillation at various frequencies to the right plunger gate RP. The signal spectrum resulting from a 1 MHz oscillation is measured at the output of the room temperature amplifier and displayed in Fig. 3.15(a). Plotting the signal-to-noise ratio (SNR) of the lower sideband (LSB) as a function of the gate oscillation frequency produces the data displayed in (b). The 3 dB bandwidth of the readout is 15 MHz.

Note that the above sensitivity and bandwidth measurements are performed using a −85 dBm carrier. According to Eq. 3.23, the sensitivity could be improved by simply increasing P_{rf} (i.e. increasing v_{QPC}). Fig. 3.15(c) shows the SNR of the LSB of a signal spectrum as a function of P_{rf}. The LSB is produced with a 1 mV_{rms}, 1 MHz sine wave applied to gate RP. The solid line indicates a 1 dB increase in LSB signal for every 1 dB increase in P_{rf} starting at −90 dBm. The noise floor in the band containing the carrier and sideband frequencies is carrier power independent in the measured range. The SNR approximately follows the straight line to about −75 dBm where is begins to deviate possibly due to heating which distorts the QPC resistance curve [70]. Several groups use $P_{\mathrm{rf}} \approx -75$ dBm for charge detection measurements [26, 27, 70]. Unfortunately during this cooldown, for powers higher than about −80 dBm, traces similar to that shown in Fig. 3.14(c) contain telegraph noise perhaps due to the activation of charge traps. This problem may be solved by simply thermally cycling the device.

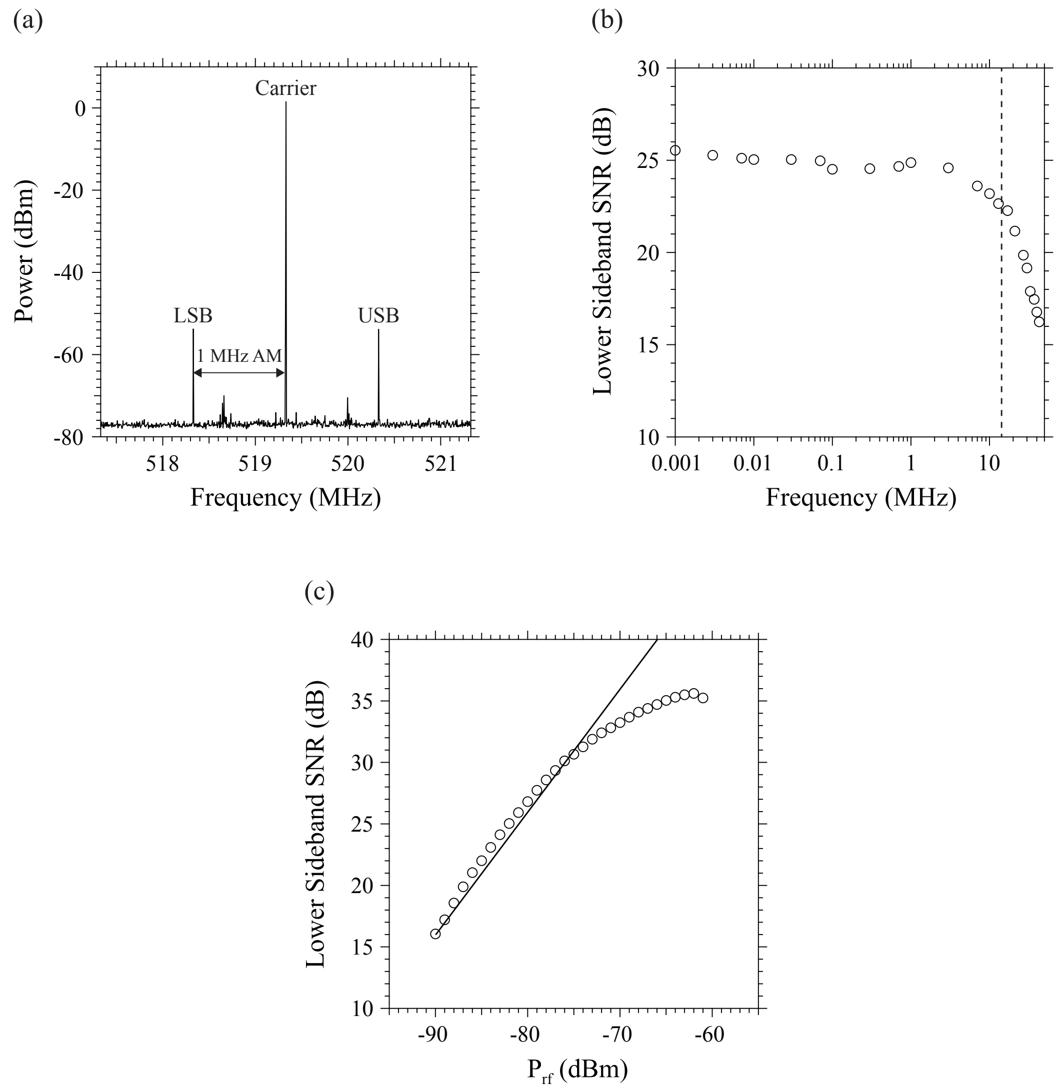

Figure 3.15: (a) Spectrum measured at the output of room temperature amplifiers (Mini-Circuits amps: 60 dB gain). The resolution bandwidth is 300 Hz and the video bandwidth is 10 Hz. (b) SNR of the LSB as a function of modulation frequency. (c) SNR of the LSB as a function of P_{rf}. The SNR of the -85 dBm point (22 dB) should agree with the 1 MHz point of (b) (25 dB). The two data set were acquired on different days, two weeks apart. The device drift made it difficult to choose the same working point on the two days.

3.7 Comparison

In this section, a simple comparison is made between the RF-QPC of this work and those of Reilly et al. [26] and Cassidy et al. [27]. The expression for charge sensitivity (Eq. 3.23) derived in Section 3.5 is shown here for convenience [58]

$$\delta q = \frac{\sqrt{2k_B T_N R_{QPC} K}}{v_{QPC} \dfrac{\partial |\Gamma|}{\partial R_{QPC}} \dfrac{\partial R_{QPC}}{\partial q}}. \tag{3.24}$$

Table 3.2 shows the charge sensitivity of each readout and a list of some of the parameters relevant to a calculation of δq. The better sensitivity shown in columns two and three is largely due to the higher carrier power (i.e. v_{QPC}) in both cases and also the better coupling (i.e. $\partial R_{QPC}/\partial q$) in the Cassidy et al. case. A larger value of $\partial|\Gamma|/\partial R_{QPC}$ may also contribute to a better sensitivity in the Cassidy et al. case, but there is not enough data in Ref. [27] to confidently produce the function $\Gamma(R_{QPC})$ and extract the required derivative.

Table 3.2: Parameters relevant to the RF-QPC measurements and the corresponding charge sensitivity.

	This work	Reilly et al [26].	Cassidy et al. [27]
R_{QPC}	70 kΩ	86 kΩ	25.8 kΩ
$\partial R_{QPC}/\partial q$	1 kΩ/e	0.85 kΩ/e	2 kΩ/e
P_{rf}	−85 dBm	−75 dBm	−73 dBm
T_N	5.2 K	3.5 K	< 5.8 K
δq	$2 \times 10^{-3}\ e/\sqrt{\mathrm{Hz}}$	$10^{-3}\ e/\sqrt{\mathrm{Hz}}$	$2 \times 10^{-4}\ e/\sqrt{\mathrm{Hz}}$

3.8 Other Charge State Readout Techniques

There are several other radio-frequency charge detection techniques that use the same reflectometry circuit as the RF-QPC. Two such techniques are briefly reviewed here. The first involves the radio-frequency single electron transistor (RF-SET). Similar to the RF-QPC, it converts a quantum dot charge state to a detector resistance that modulates the amplitude of the reflected signal. The second type is a dispersive readout that converts changes in the quantum capacitance of a DQD to a phase shift of the reflected signal.

3.8.1 Radio-frequency Single Electron Transistor

There are at least two flavors of the RF-SET. The version described in Ref. [71] is also called a radio-frequency sensor quantum dot (RF-SQD). A SQD can be formed with gates RS, Q1, and Q1 as shown in Fig. 3.16(a). The dashed white circle shows the approximate position of the SQD. Barthel et al. show that their RF-SQD achieves a signal-to-noise ratio three times that of their RF-QPC (using 10 dB lower incident rf power) [71].

The other version of the RF-SET is shown schematically in Fig. 3.16(b). The SEM image is extracted from Ref. [72]. The source and drain leads are connected to the aluminum SET island through AlO_x tunnel barriers. The electrical transport through the SET exhibits Coulomb blockade oscillations similar to a quantum dot. The G_{SET} gate allows tuning to a point of maximum sensitivity (i.e. maximum slope on the Coulomb blockade oscillation curve). The SET island is in the shape of a 'T' that extends through a break in the side gate to a region above the dots. This is done in an attempt to maximize the capacitive coupling between the SET and the dots. Typically SETs are described by a charge sensitivity metric similar to the QPC. Lu et al. report an RF-SET coupled to a GaAs single dot with a charge sensitivity $\delta q \approx 2.4 \times 10^{-5}\ e/\sqrt{\text{Hz}}$ [73]. Note, however, that this value is referenced to the SET island itself. In an actual charge detection measurement, a change by one electron in the quantum dot charge state changes the offset charge of the SET island by ~$0.1e$. The charge sensitivity referenced to the quantum dot is thus on the order of ~$10^{-4}\ e/\sqrt{\text{Hz}}$, similar to the RF-QPC. Yuan et al. describe charge detection measurements of a Si/SiGe DQD using an RF-SET. They report a charge sensitivity of

~$10^{-4}\ e/\sqrt{\mathrm{Hz}}$ referenced to the DQD [72].

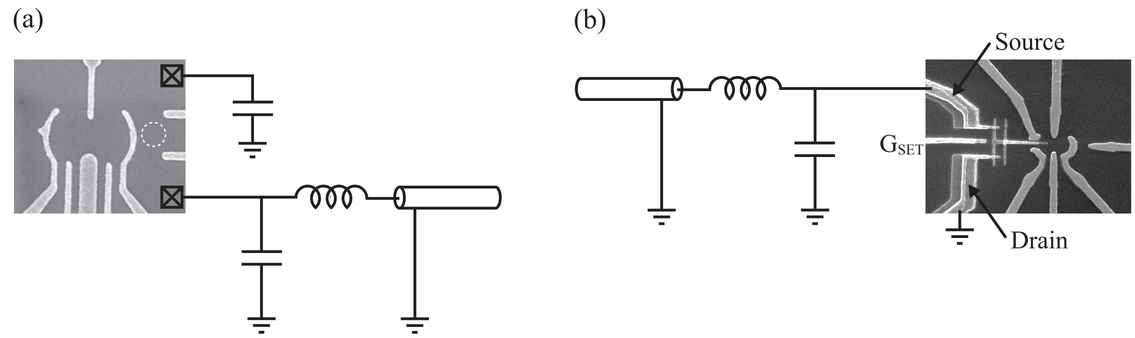

Figure 3.16: Charge detection technique using an RF-SET capacitively coupled to the DQD. An LC circuit is used to transform the resistance of a sensor quantum dot (white dash) in (a) and a superconducting single electron transistor in (b). SEM image in (b) reprinted from Applied Physics Letters **101**, 142103 (2012), with the permission of AIP Publishing.

3.8.2 Quantum Capacitance Detectors

Transport through a DQD is characterized by a complex admittance, consisting of a real component to describe resistance and a complex component related to electron tunneling. The latter component is called quantum capacitance, defined by

$$C_Q = (e\kappa)^2 \frac{\partial^2 E}{\partial \varepsilon^2}, \tag{3.25}$$

where E is the energy of the relevant DQD state, ε is detuning, and κ is a coupling constant that relates the voltage of the LC circuit to detuning energy [74]. Note that C_Q is non-zero only at the charging lines of a stability diagram where tunnel coupling produces hybridized charge states and bonding and antibonding energy levels. As an example, the energy levels of the superposition states formed near the (1,0)↔(0,1) charge transfer line ($\varepsilon = 0$) is shown in Fig. 3.17(a). There are several types of readout techniques based on the quantum capacitance of a DQD, two of which are mentioned here. In both cases, the reflectometry circuit is identical to that of the RF-QPC except for the particular connections to the device. Fig. 3.17(a) shows the LC circuit connected to an ohmic contact of the DQD. At charging lines, when electrons tunnel in response to the incident rf signal, C_Q changes. This shifts the total capacitance of the LC circuit, changing its resonance frequency and thus the phase of the reflected signal. By measuring such phase shifts at charging lines of a stability diagram, Petersson et al. construct a readout that requires an integration time of 4 ms to achieve a signal-to-noise ratio of one [74]. Their readout has a bandwidth of 24 MHz.

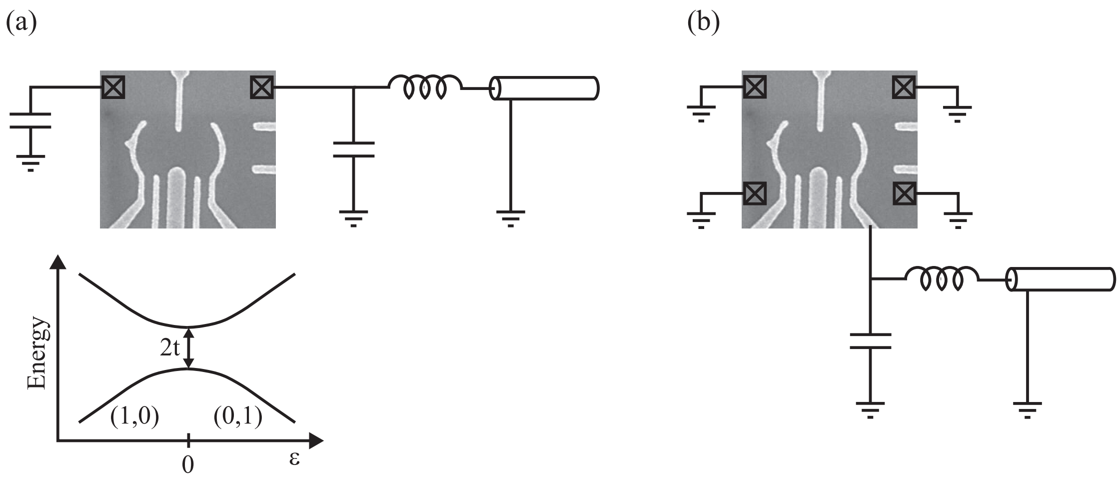

Figure 3.17: Detect transitions between charge states by measuring the quantum capacitance of the DQD. (a) The energy levels of the superposition states formed at the (1,0)↔(0,1) charge transfer line. The DQD quantum capacitance is non-zero near $\varepsilon = 0$. Connect the LC circuit to an ohmic contact in (a) or a depletion gate in (b). In both cases, changes in quantum capacitance shift the resonance frequency of the LC circuit producing a phase shift of the reflected signal.

Fig. 3.17(b) shows the connections to the DQD device for another technique that relies on C_Q. In this case, the LC circuit is connected to one of the gates that define the DQD. Electron tunneling due to the rf signal applied to the gate produces a change in C_Q and a phase shift of the reflected signal. Colless et al. show that such a dispersive gate sensor (DGS) can produce a 10 MHz bandwidth readout with a charge sensitivity of $6.3 \times 10^{-3}\ e/\sqrt{\text{Hz}}$ [75]. Note that unlike the RF-QPC, the DGS does not require compensation for parasitic gating. It also maintains sensitivity at elevated temperatures where the QPC sensitivity is suppressed due to thermal broadening of the conductance curve.

3.9 Conclusions and Future Work

The RF-QPC achieves a charge sensitivity similar to that of other groups. Certainly being able to increase P_{rf} from -85 dBm to a more typical value of -75 dBm would help improve the sensitivity of the readout. Hopefully after thermally cycling the device, this will be possible. The superconducting inductor does not seem to improve readout sensitivity relative to an RF-QPC based on a normal metal inductor. The improvement one might expect, primarily from an increase in $\partial|\Gamma|/\partial R_{QPC}$, is not observed in the current device because the working point for charge detection, determined by the slope of the QPC resistance curve, is at $R_{QPC} \approx 70$ kΩ instead of near $h/e^2 \approx 25.8$ kΩ as in Ref. [27]. Perhaps machining the ground plane would lower the parasitic capacitance of the inductor and increase the value of R_{QPC} corresponding to optimal match. Increasing the charge sensitivity should be possible by changing from the QPC to the SQD charge detector.

Chapter 4

S-T$_+$ Spin Qubit

4.1 Introduction

The building block of classical information theory is the Boolean bit which takes two distinct values, 0 and 1. Analogously, quantum information theory is based on quantum two-level systems called quantum bits or qubits which are abstractly represented by basis states $|0\rangle$ and $|1\rangle$. Being composed of quantum states, the qubit however, unlike the classical bit, can take on a continuum of values $a\,|0\rangle + b\,|1\rangle$, where $|a|^2 + |b|^2 = 1$. Manipulation of these linear superpositions is the source of the greater efficiency of quantum computing algorithms relative to their classical counterparts [76]. Qubits have been realized in a variety of physical systems. For example, qubits based on spin states of a spin-1/2 nucleus [77, 78], flux states of a Superconducting QUantum Interference Device (SQUID) [79], and energy levels of atoms in a optical dipole trap [80] have all been demonstrated. There are also several ways to realize qubits in lateral quantum dot devices [4]. Qubits based on the charge or spin of the electron have been proposed and implemented in single [81, 82], double [11, 83], and triple quantum dot devices [22, 84]. This chapter focuses on one flavor of spin-qubit formed by two-electron spin states in a DQD. The basis states are the singlet, S, and $m = +1$ triplet, T_+. This S-T_+ qubit was first demonstrated by Jason Petta in Ref. [20].

4.2 Landau-Zener Effect

The operation of several of these qubits relies on a phenomenon known as the Landau-Zener effect. It describes nonadiabatic transitions at an avoided crossing of the energy levels of a quantum system [85, 86, 87]. In the context of quantum computing, it is employed to form and manipulate superpositions of the qubit basis states. This section is devoted to a general description of the phenomenon. The physics of two-level systems required for this discussion is reviewed in Appendix B and summarized in Fig. 4.1(a). The qubit basis states $|0\rangle$ and $|1\rangle$ have energies E_0 and E_1 respectively. By definition, these energies cross when plotted as a function of detuning, $\varepsilon = E_1 - E_0$. For $\varepsilon > 0$, $|0\rangle$ is the ground state and $|1\rangle$ is the excited state. For $\varepsilon < 0$, the situation is reversed. Introducing off-diagonal coupling, Δ, connecting the basis states, creates new eigenstates $|a\rangle$ and $|b\rangle$, both superpositions of $|0\rangle$ and $|1\rangle$ with expansion coefficients that depend on ε. The corresponding energy eigenvalues E_a and E_b exhibit an anticrossing when plotted as functions of ε, with minimum separation $2|\Delta|$ occurring at $\varepsilon = 0$.

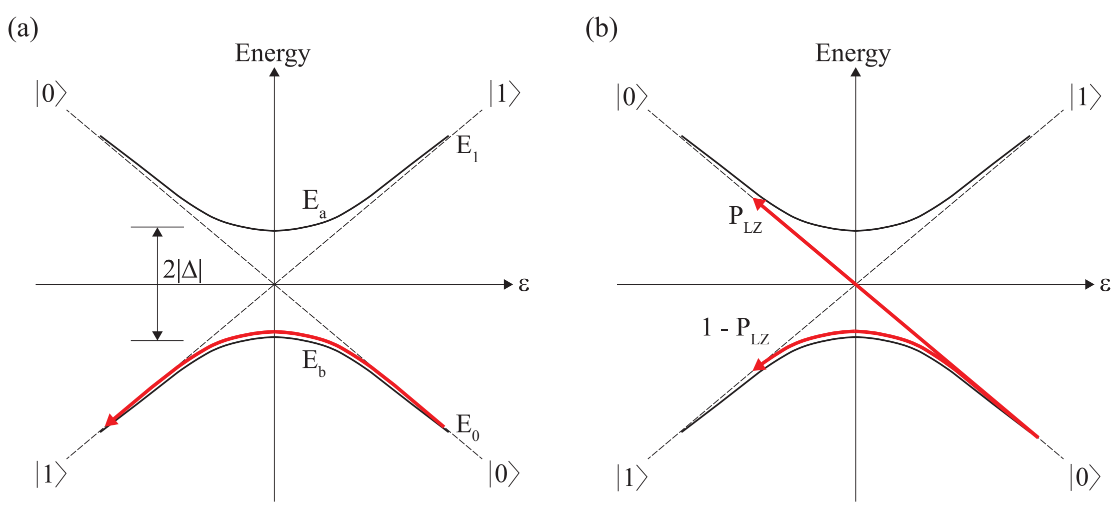

Figure 4.1: (a) Off-diagonal coupling of two states turns an energy level crossing into an anticrossing. (b) The analysis of Landau and Zener shows that during a detuning sweep through the anticrossing, the system can transition between the branches.

Begin with the system in the ground state $|0\rangle$ at $\varepsilon \gg 0$, away from the anticrossing. Consider the effect of executing the detuning sweep represented by the curved arrow in Fig. 4.1(a). In the vicinity of the anticrossing, $|b\rangle$ is formed. As ε decreases, the weight of $|1\rangle$ in the superposition state $|b\rangle$ increases and the weight of $|0\rangle$ decreases. At $\varepsilon = 0$, the weight of the two basis states is equal. This process continues until at $\varepsilon \ll 0$, the system is found in the new ground state $|1\rangle$. Note that this description does not consider the speed of the sweep or more specifically the time rate of change of the energy difference $E_1 - E_0$. Landau and Zener, with their fully time-dependent analysis, show that during a detuning sweep, with an energy level velocity $\nu = |d(E_1 - E_0)/dt|$, it is possible for the system to transition between $|b\rangle$ and $|a\rangle$ at the anticrossing and finish in the excited state $|0\rangle$ instead of the ground state $|1\rangle$ for $\varepsilon \ll 0$. In the case that ν is a linear function of time, the probability of such a transition is $P_{LZ} = \exp\left(-\frac{2\pi\Delta^2}{\hbar\nu}\right)$, called the Landau-Zener probability. With only two possibilities, the system remains on the ground state branch, transitioning from one ground state to the other with probability $1 - P_{LZ}$. The detuning sweep is recast in terms of P_{LZ} in Fig. 4.1(b). Note that in the limit $\Delta \to 0$, the branches approach each other and $P_{LZ} \to 1$, called the diabatic case. In the opposite limit where $\Delta^2/\hbar$ is large relative to ν, $P_{LZ} \to 0$, called the adiabatic case. In the intermediate case, a superposition of the two states results. As an example, for $P_{LZ} = 1/2$, the resulting state is an equally weighted superposition of the qubit basis states $|0\rangle$ and $|1\rangle$ for $\varepsilon < 0$.

4.3 Energy Levels of Two-Electron States

A discussion of two-electron spin qubits begins with an analysis of the related energy levels. Consider the possible spin states of the (0,2) and (1,1) charge states. The ground state of (0,2) in a low magnetic field is composed of two electrons occupying the lowest energy orbital state in a spin singlet configuration, $S(0,2)$ [14]. Since the triplet state, $T(0,2)$, is a symmetric spin state, the corresponding spatial (orbital) component of the total wavefunction must be antisymmetric. This requires one of the electrons to occupy an excited orbital state. The result is an energy difference between $T(0,2)$ and $S(0,2)$ called the singlet-triplet splitting, $E_{ST} \approx 600$ μeV , making $T(0,2)$ inaccessible in the case of low DQD bias and small values of detuning [40]. When the two electrons are separated on different dots, however, the singlet-triplet energy splitting is usually reduced to a negligibly small value and the spin states $S(1{,}1)$ and $T(1{,}1)$ are thus nearly degenerate. At the boundary in the stability diagram that separates the (0,2) and (1,1) regions ($\varepsilon = 0$), these states are also degenerate with $S(0{,}2)$ in the case of zero tunnel coupling between the dots ($t = 0$). The resulting energy level crossing at $\varepsilon = 0$ is shown in Fig. 4.2(a). Introducing finite tunnel coupling between the dots ($t > 0$) produces the anticrossing of the singlet states in Fig. 4.2(b). The triplet $T(1{,}1)$, however, being orthogonal to $S(0{,}2)$ is unaffected. Finally, a magnetic field, B, splits the triplet states $T_-(1{,}1)$, $T_0(1{,}1)$, and $T_+(1{,}1)$ by the Zeeman energy $E_Z = g\mu_B B$, where μ_B is the Bohr magneton and $g = -0.44$ for electrons in GaAs [88]. The result is shown in Fig. 4.2(c).

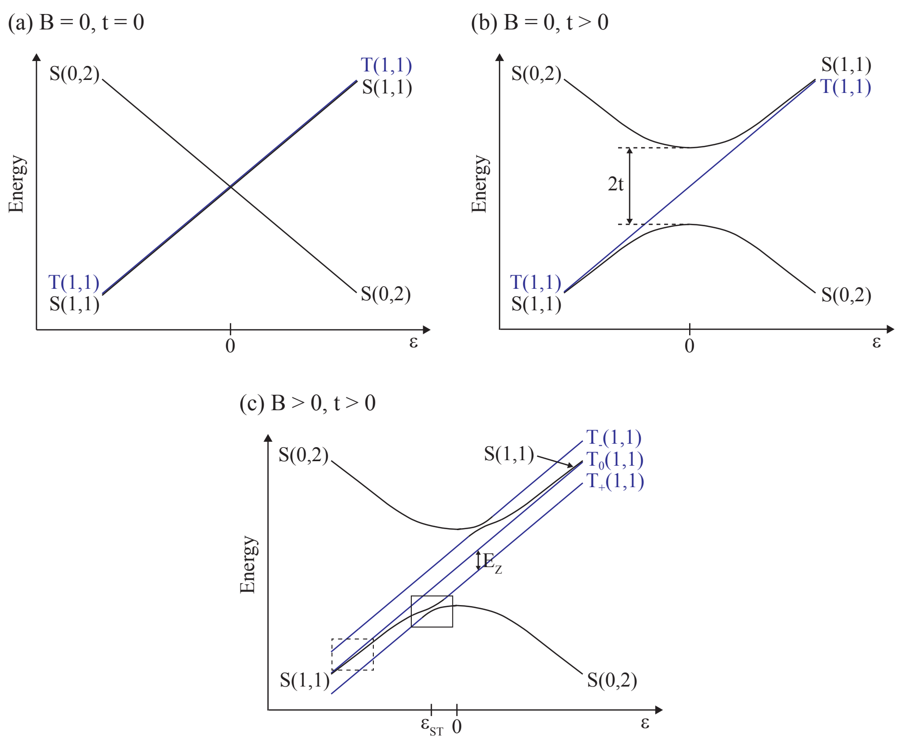

Figure 4.2: Two-electron spin state energy levels. (a) without tunnel coupling (b) with tunnel coupling (c) with tunnel coupling and a magnetic field. Hyperfine interaction with the lattice nuclei produces the anticrossing at $\varepsilon = \varepsilon_{ST}$.

Note that the energy of the spin polarized triplet $T_+(1,1)$ [and $T_-(1,1)$] is shown forming an anticrossing with a singlet branch at ε_{ST} (solid rectangle). The coupling that produces this anticrossing results from the hyperfine interaction between each quantum dot electron spin and the spin-3/2 Ga and As lattice nuclei in each of the dots [89, 90]. The interaction is described by the Hamiltonian

$$H_{\mathrm{HF}} = \mathbf{S}_1 \cdot \mathbf{h}_1 + \mathbf{S}_2 \cdot \mathbf{h}_2,$$

where $\mathbf{S}_i$ is operator for the electron spin in dot i and

$$\mathbf{h}_i = \sum_{k=1}^{n_i} A_i^k \mathbf{I}_i^k$$

is Overhauser effective magnetic field operator for the same dot [91]. The sum runs over the $n_i \approx 10^6$ nuclei in each dot. The spin operator for nucleus k in dot i is $\mathbf{I}_i^k$ and the coupling constant A_i^k characterizes the overlap of the electron wavefunction with nucleus k. Using raising and lower operators $S_i^{\pm} = S_i^x \pm \mathrm{i}S_i^y$ and $h_i^{\pm} = h_i^x \pm \mathrm{i}h_i^y$, H_{HF} can be recast in the following form [91]

$$H_{\mathrm{HF}} = \frac{1}{2}\sum_i (2S_i^z h_i^z + S_i^+ h_i^- + S_i^- h_i^+).$$

The first term adds to the energy of the triplet state while the second and third terms, called flip-flop terms, couple $S(1,1)$ and $T_+(1,1)$. Essentially a quantum dot electron spin flip and a corresponding nuclear spin flop, a process which conserves angular momentum, can turn $S(1,1)$ with spin 0 into $T_+(1,1)$ with spin 1 and vice versa.

The remainder of this chapter is primarily concerned with the qubit formed by the $S(1,1)$ and $T_+(1,1)$ states, the S-T_+ qubit. Superpositions of these states are created at the ε_{ST} anticrossing by Landau-Zener tunneling. As mentioned in the introduction to the chapter, other qubits based on two-electron states have also been proposed and implemented. A qubit formed by the singlets $S(0,2)$ and $S(1,1)$ is demonstated in Ref. [83]. Again Landau-Zener tunneling, this time at the $\varepsilon = 0$ anticrossing, is employed to create superposition states. Finally, $S(1,1)$ and $T_0(1,1)$ are basis states for the S-T_0 qubit first demonstrated in Ref. [11]. In this case, mixing of the basis states does not occur at an anticrossing but rather in the region of near degeneracy outlined with the dashed rectangle in Fig. 4.2(c).

4.4 Operation of the S-T$_+$ Spin Qubit

Fig. 4.3 summarizes the basic operation of the S-T_+ qubit. It shows the trajectory through the energy level diagram in the vicinity of the anticrossing at $\varepsilon = \varepsilon_{ST}$ and the motion of a vector on the Bloch sphere [92, 93, 94, 95]. The arrow in Fig. 4.4(a) represents the corresponding trajectory on the stability diagram.

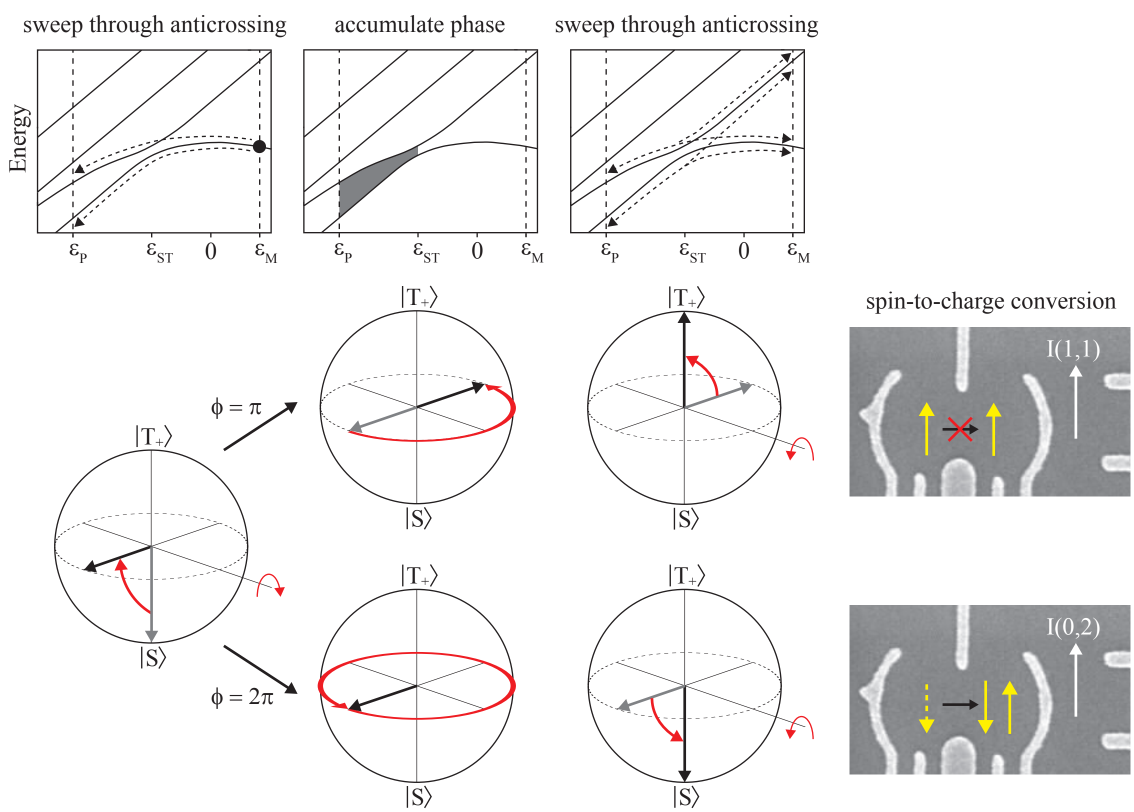

Figure 4.3: Operation of the S-T_+ qubit in terms of sweeps through the S-T_+ anticrossing and the corresponding motion of a vector on the Bloch sphere.

Starting with the system in the S(0,2) ground state at point M, a gate voltage pulse is created by an arbitrary waveform generator and delivered to the plunger gates via the high-bandwidth lines and bias tees described in Section 2.5. The timing diagram for the pulse is

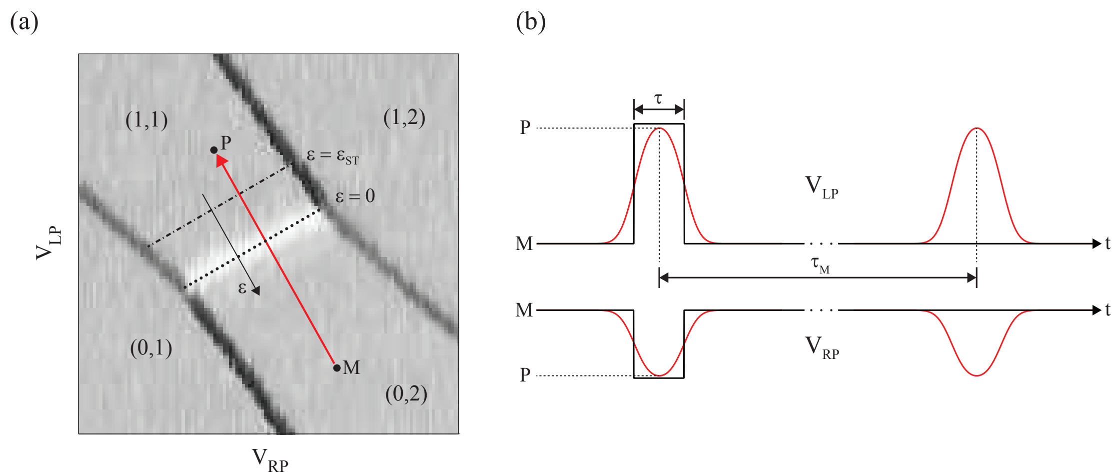

Figure 4.4: (a) Stability diagram in the few electron regime. The S-T_+ anticrossing ($\varepsilon = \varepsilon_{ST}$) is marked with a dash-dotted line. The trajectory of the plunger gate voltage pulse is represented by an arrow. (b) Timing diagram for the plunger gate voltage pulses. Synchronized Gaussian shaped voltage pulses are applied to the plunger gates to sweep out the trajectory shown in (a).

shown in Fig. 4.4(b). It is the result of a numerical convolution of a rectangular pulse and a Gaussian function of the form $\frac{1}{\sqrt{2\pi}s}e^{-t^2/2s^2}$. Typically $s = 4$ ns giving a 10-90% rise time of approximately 8 ns. The first half of the pulse moves an electron to the left dot by sweeping the system into the (1,1) ground state region through the anticrossing (ε_{ST}) to point P, in the process creating a superposition of the qubit states by the Landau-Zener effect. On the Bloch sphere, this operation is described by a rotation of the singlet state into the transverse plane, although this equal weighted superposition is created only in the $P_{LZ} = 0.5$ case. Since the $S(1,1)$ and $T_+(1,1)$ terms of this superposition possess different energies, a phase difference between the two terms $\phi = \frac{1}{\hbar}\int\{E_S[\varepsilon(t)] - E_{T_+}[\varepsilon(t)]\}dt$ accumulates during the time spent in the (1,1) ground state region beyond the anticrossing. The area corresponding to ϕ, located between E_S and E_{T_+}, that is swept out in moving from ε_{ST} to ε_P is shaded gray in the energy-level diagram of Fig. 4.3. This accumulation of phase difference between the two qubit states corresponds to a z-axis rotation on the Bloch sphere. That is, the weights of the two states in superposition remain the same. Only the relative phase changes. The second half of the pulse which sweeps the system back through the anticrossing to point M in the (0,2) ground state region corresponds to another rotation about the axis in the transverse plane. Finally the resulting qubit state is measured by a technique relying on a DC-QPC charge detector and the spin-blockade effect. If $\phi = 2\pi$, the final qubit state is S(1,1) and the system transitions to the tunnel coupled S(0,2) ground state. The corresponding QPC charge detector current is $I_{QPC} = I(0,2)$. If $\phi = \pi$, the final qubit state is T_{+}(1,1). Since tunneling between dots conserves spin and the T(0,2) state is inaccessible, the system remains in the (1,1) charge state for a characteristic time $T_1 \approx 100$ μs due to spin blockade [41, 52]. The charge detector current measured before the decay process is $I_{QPC} = I(1,1)$. This technique of mapping each spin state to a unique charge state that can be distinguished with a charge detector is called spin-to-charge conversion. In practice, the final qubit state at point M is determined by measuring I_{QPC} continuously during the execution of $\sim 10^5$ pulses. Since the pulse duration is $\tau \approx 20$ ns and the pulse period (time between pulses) is $\tau_m \approx 2$ μs, the time-averaged charge detector signal is largely determined by the charge state at point M. As ϕ increases and the relative weights of S and T_{+} in the final state changes, this time-averaged I_{QPC} changes in a periodic manner (i.e. oscillates) but stays within the range I(0,2) to I(1,1). If the final state is more heavily weighted towards S, I_{QPC} is closer to I(0,2) than I(1,1). Similarly, a final state more heavily weighted towards T_{+} corresponds to a value of I_{QPC} closer to I(1,1) than I(0,2). The qubit oscillations observed as ϕ varies are known as Landau-Zener-Stückelberg (LZS) oscillations.

This standard description of the S-T_{+} qubit operation needs slight modification to correctly capture the physics of most experiments. Due to the fluctuating magnetic field produced by the lattice nuclei, phase coherence is lost and the amplitude of the oscillations decay with a characteristic timescale $T_2^* \approx 15$ ns. As a result, the pulse length is typically chosen to be of the same order, 10-20 ns [96, 97]. As noted in Ref. [20], for an energy splitting of $2\Delta = 120$ neV and a Gaussian shaped pulse with a 10-90% rise time of about 7 ns, the Landau-Zener probability is $P_{LZ} = 0.96$. The rotation of the Bloch vector associated with the first sweep through the anticrossing therefore does not end with the vector in the transverse plane. To achieve maximum LZS oscillation amplitude (called maximum visibility) requires $P_{LZ} = 0.5$. For the device configuration discussed in Ref. [20], detuning ramp times of approximately 160 ns $\gg T_2^*$ are needed to achieve $P_{LZ} = 0.5$ [20]. There is recent progress towards achieving this optimal condition using a pulse with a detuning dependent energy level velocity. This new type of pulse has a slow ramp only near the anticrossing and an overall pulse length of less than T_2^* [98].

4.5 Spin Funnel

Consider the stability diagram of Fig. 4.5(a). This gray scale plot of QPC transconductance is acquired in the presence of a $\tau = 50$ ns gate voltage pulse ($\tau_m = 2$ μs, $s = 4$ ns) represented by the arrow on the diagram. That is, at each point of the stability diagram, $\sim 10^5$ pulses are executed and the average transconductance value is plotted. Since this pulse is significantly longer than $T_2^* \approx 15$ ns, only the result of incoherent mixing of S(1,1) and T_+(1,1) that occurs when the pulse just reaches the anticrossing is observed (white line). Alternatively, instead of acquiring an entire stability diagram, simply execute detuning sweeps ($1 \rightarrow 2$) while continuing to apply the pulse. The resulting data for various magnetic fields (applied in the plane of the 2DEG) is shown in Fig. 4.5(b). The vertical axis is the V_{LP} component of the $1 \rightarrow 2$ trajectory. Because the data has a funnel shape, such data sets are referred to as spin funnels. The existence of magnetic field dependence provides some evidence that the extra white line on the stability diagram is actually the result of $S - T_+$ mixing and not just an artifact of the pulse. To observe LZS oscillations, repeat the same experiment with a shorter duration pulse (same 8 ns rise time). Using a $\tau = 17$ ns pulse produces the data displayed in Fig. 4.5(c). The oscillations occur because as the system moves from point 1 to point 2, the pulse moves deeper into the (1,1) ground state region, further beyond the anticrossing and ϕ increases, changing the value of I_{QPC} and also transconductance, dI_{QPC}/dV_{LP}, in a periodic manner.

Consider the oscillations in Fig. 4.5(c) for $B = 80$ mT (vertical short dashed line). Starting at $V_{LP} = -0.381$ V and moving towards the charge transfer line (horizontal dotted line), first the line corresponding to incoherent mixing is encountered and then the coherent oscillations begin, consecutive bright fringes corresponding to $\Delta\phi = 2\pi$. In an attempt to understand the magnetic field dependence of the fringes, also consider the vertical long

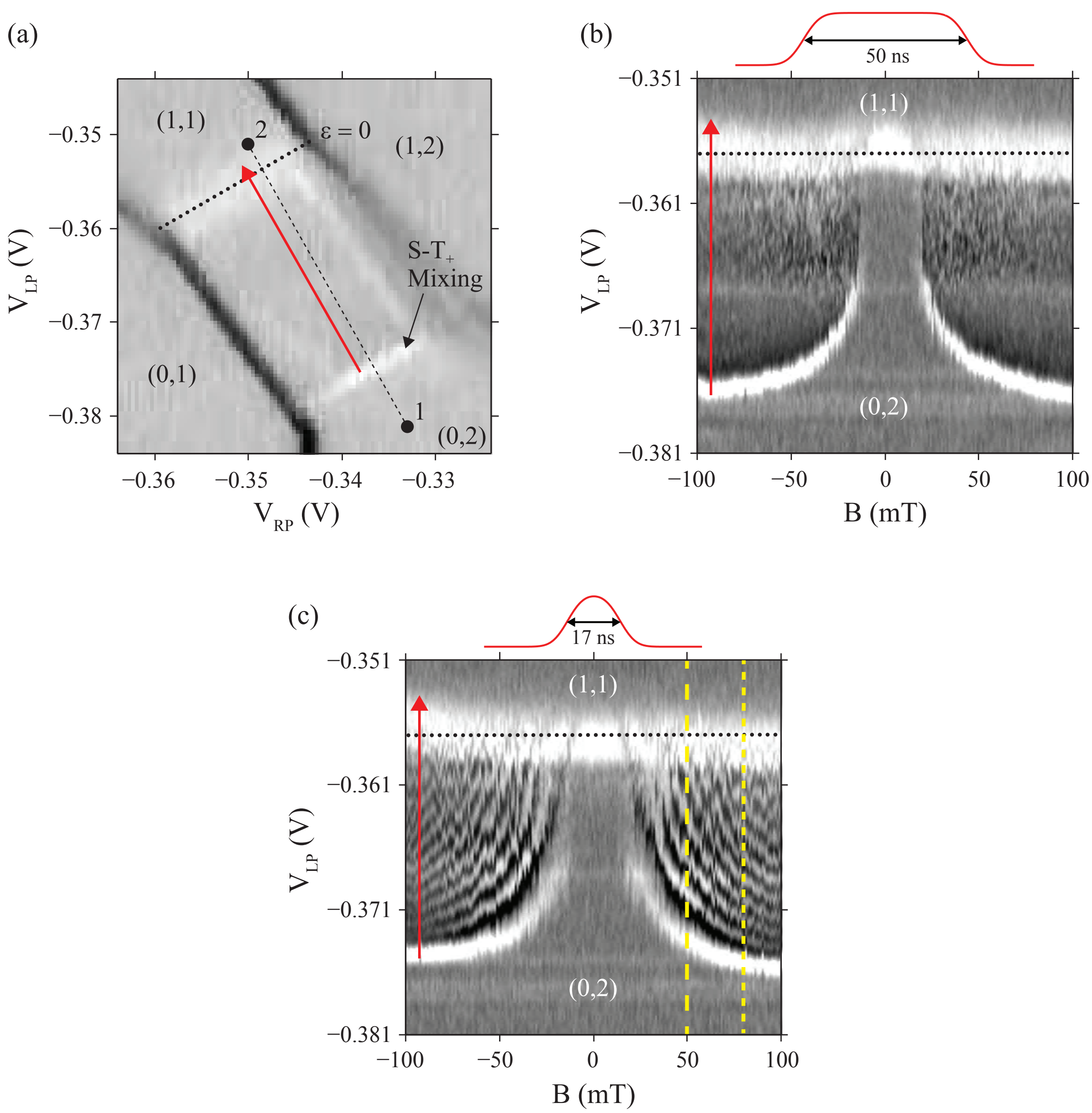

Figure 4.5: (a) Stability diagram acquired in the presence of a gate voltage pulse (τ = 50 ns, s = 4 ns, τ_m = 2 μs) and a magnetic field of 100 mT. (b) QPC transconductance as a function of the V_{LP} component of path 1 → 2 in (a) for various values of magnetic field. (c) Repeat the experiment with a τ = 17 ns pulse (long dash: 50 mT, short dash: 80 mT).

dashed line at B = 50 mT. Relative to the B = 80 mT case, the fringes start closer to the charge transfer line and possess a lower frequency. Referring to the energy level diagrams in Fig. 4.6, a decrease in B (and thus E_Z) moves the anticrossing ($\varepsilon = \varepsilon_{ST}$) away from the charge transfer line ($\varepsilon = 0$), deeper into the (1,1) region. In order for the pulse to reach the anticrossing, the initial point of the pulse (on the $1 \rightarrow 2$ trajectory) in the (0,2) region must therefore be located closer to the charge transfer line as the field decreases. The decrease in oscillation frequency with decreasing field results from a corresponding decrease in the area between the S and T_+ energy levels. Simply, a larger fraction of the pulse amplitude is required to sweep out $\Delta\phi = 2\pi$ and move between bright fringes as the field decreases.

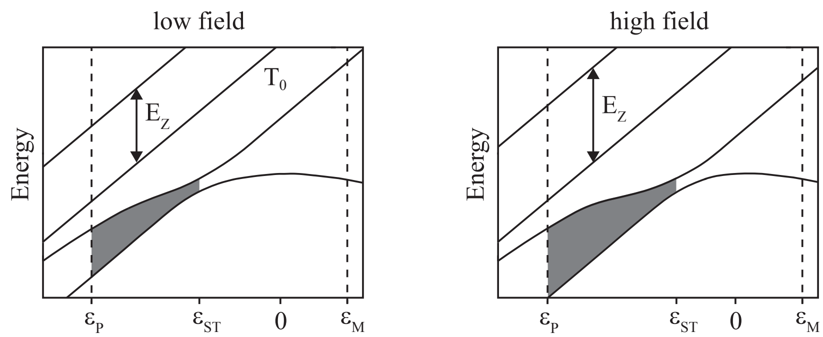

Figure 4.6: As the magnetic field increases, E_Z increases, moving the anticrossing towards $\varepsilon = 0$ and increasing the phase accumulated (gray area) for a given pulse.

4.6 Spin-to-charge Conversion

4.6.1 Introduction

To distinguish the states of a quantum dot spin qubit using a charge detector such as a QPC requires a technique that maps each spin state to a unique charge state. This section reviews the standard spin-to-charge conversion technique explained in Section 4.4 and then discusses alternative techniques involving metastable charge states [23]. The data and analysis presented here is also found in Ref. [99], a paper co-written with Sergei Studenikin and Andrew Sachrajda of NRC.

The data shown in this section is a small subset of the data acquired during the course of the graduate program. Most of the data contains distortions and is thus not easily interpreted. A brief discussion of the difficulties associated with acquiring LZS data as well as some preliminary data showing the effect of the QPC charge detector bias on the LZS oscillations is presented in Appendix A.

4.6.2 Role of Metastable Charge States

Consider Fig. 4.7(a) which shows a stability diagram in the few electron regime of the DQD. Addition lines (black and gray) and extensions of addition lines (dash) divide the diagram into four regions labeled R1, R2, R3, and R4. The majority of this section is devoted to explaining the spin-to-charge conversion mechanism in each of these regions. A plunger gate voltage pulse (arrow), chosen to be approximately parallel to the left dot addition line, is applied during the acquisition of a stability diagram to produce the LZS oscillations shown in Fig. 4.7(b). Note that in this case, the qubit operation involves the (2,0) rather than the (0,2) charge state. The operation of the qubit is otherwise the same as described in the previous sections. The pulse is τ = 17 ns in duration, possesses an 8 ns rise time (s = 4 ns) and is applied every τ_m = 2 μs. Each data point is the average QPC transconductance resulting from 5×10^4 individual pulses. The QPC transconductance is measured using V_{QPC} = 200 μV and a 240 μV_{rms}, 17 Hz sinusoidal oscillation on gate LP. A magnetic field of 80 mT is applied in the plane of the 2DEG approximately perpendicular to the line joining the two dots.

An analysis of Fig. 4.7(b) begins by noting that, unlike in the case of Fig. 4.7(a), the device is tuned to have very asymmetric tunnel couplings to the leads. By the technique described in Section 2.5, the tunneling rate between the right dot and the right lead is determined to be greater than 20 MHz. The corresponding tunneling time is therefore $T_R <$ 50 ns. The coupling between the left dot and the left lead is, however, comparatively weak. The missing left dot addition line (black short-dash) separating the (2,0) and (1,0) regions implies a tunneling rate of less than the 17 Hz modulation frequency and a corresponding tunneling time of $T_L >$ 50 ms.

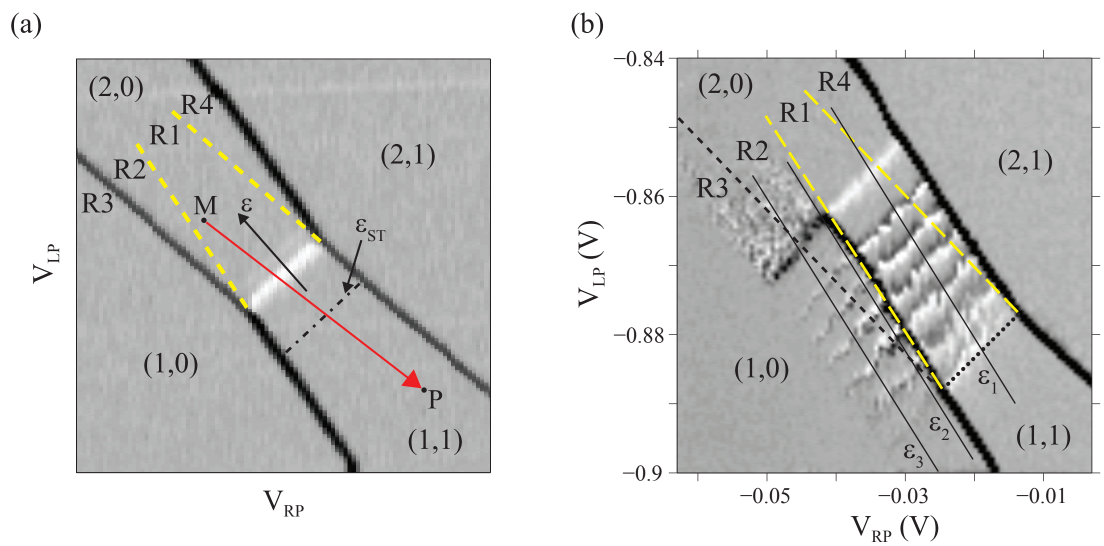

Figure 4.7: (a) Stability diagram in the few electron regime. Addition lines (black and gray) and extensions of addition lines (dash) form boundaries between the regions labeled R1, R2, R3, and R4. (b) Stability diagram acquired in the presence of the plunger gate pulse (τ = 17 ns, s = 4 ns, τ_m = 2 μs) shown in (a). The black short-dashed line represents the missing addition line and the black dotted line shows the position of the charge transfer line. The lines labeled ε_1, ε_2, and ε_3 indicate the positions of the line scans relevant to Fig. 4.10. An 80 mT magnetic field is applied in the plane of the 2DEG in a direction perpendicular to the line joining the two dots.

In the case of R1, the oscillations are contained within the highlighted boundaries shown in Fig. 4.8(a). The arrow represents a pulse which just reaches the S-T_+ avoided crossing. For initial points, M, within the boundaries, the pulse sweeps through the avoided crossing producing the observed LZS oscillations. Note the order of energy levels corresponding to region R1 shown in Fig. 4.9(a). The ground state is (2,0) while the first and second excited states are (1,1) and (1,0) respectively. The spin-to-charge conversion technique that maps spin states to charge states in R1 is shown below the energy-level diagram. Similar to the technique outlined in Section 4.4, a final state $S(1{,}1)$ quickly tunnels to the singlet ground state $S(2{,}0)$, resulting in $I_{QPC} = I(2{,}0)$. A $T_+(1{,}1)$ final state, however, is prevented from transitioning to the ground state for a time $T_1 \approx 100$ μs due to the spin blockade effect [41]. Since T_1 is longer than the measurement time (pulse period) $\tau_m = 2$ μs, $T_+(1{,}1)$ is effectively mapped to the (1,1) charge state and thus $I_{QPC} = I(1{,}1)$.

Moving from R1 to R2 in Fig. 4.7(b) involves crossing the extension of the right dot addition line separating the (1,0) and (1,1) ground state regions (long-dash). As shown in Fig. 4.9(b), (2,0) remains the ground state and (1,0) replaces (1,1) as the first excited state. The LZS oscillations of R2 are located within the highlighted triangular area of Fig. 4.8(b). As in R1, readout of $S(1{,}1)$ involves a rapid transition to the $S(2{,}0)$ ground state leading to a charge detector current $I_{QPC} = I(2{,}0)$. The spin-to-charge conversion process for $T_+(1{,}1)$, however, differs from that employed in R1. When the system returns to R2 after the pulse, an electron is ejected from the right dot and $T_+(1{,}1)$ transitions to the (1,0) charge state on a time scale $T_R < 50$ ns that is short relative to the relaxation time $T_1 \approx 100$ μs associated with a transition to the $S(2{,}0)$ ground state. Because the relaxation time from the (1,0) excited state to the (2,0) ground state, $T_L \approx 50$ ms, is long compared to the other time scales of system, the (1,0) state is considered a metastable excited state. Since $\tau_m < T_L$, $T_+(1{,}1)$ is effectively mapped to the (1,0) state and $I_{QPC} = I(1{,}0)$.

Consider the LZS oscillations in the highlighted region of Fig. 4.8(c). Since R3 is located in the (1,0) region of the stability diagram, (1,0) moves to the ground state position in the energy-level diagram shown in Fig. 4.9(c). The first and second excited states are (2,0) and (1,1) respectively. Similar to the spin-to-charge conversion technique employed in R2, readout of a spin state in R3 uses a metastable charge state. Following a pulse, since $T_R \ll T_1$, an electron is ejected from the right dot and $T_+(1{,}1)$ transitions to the (1,0)

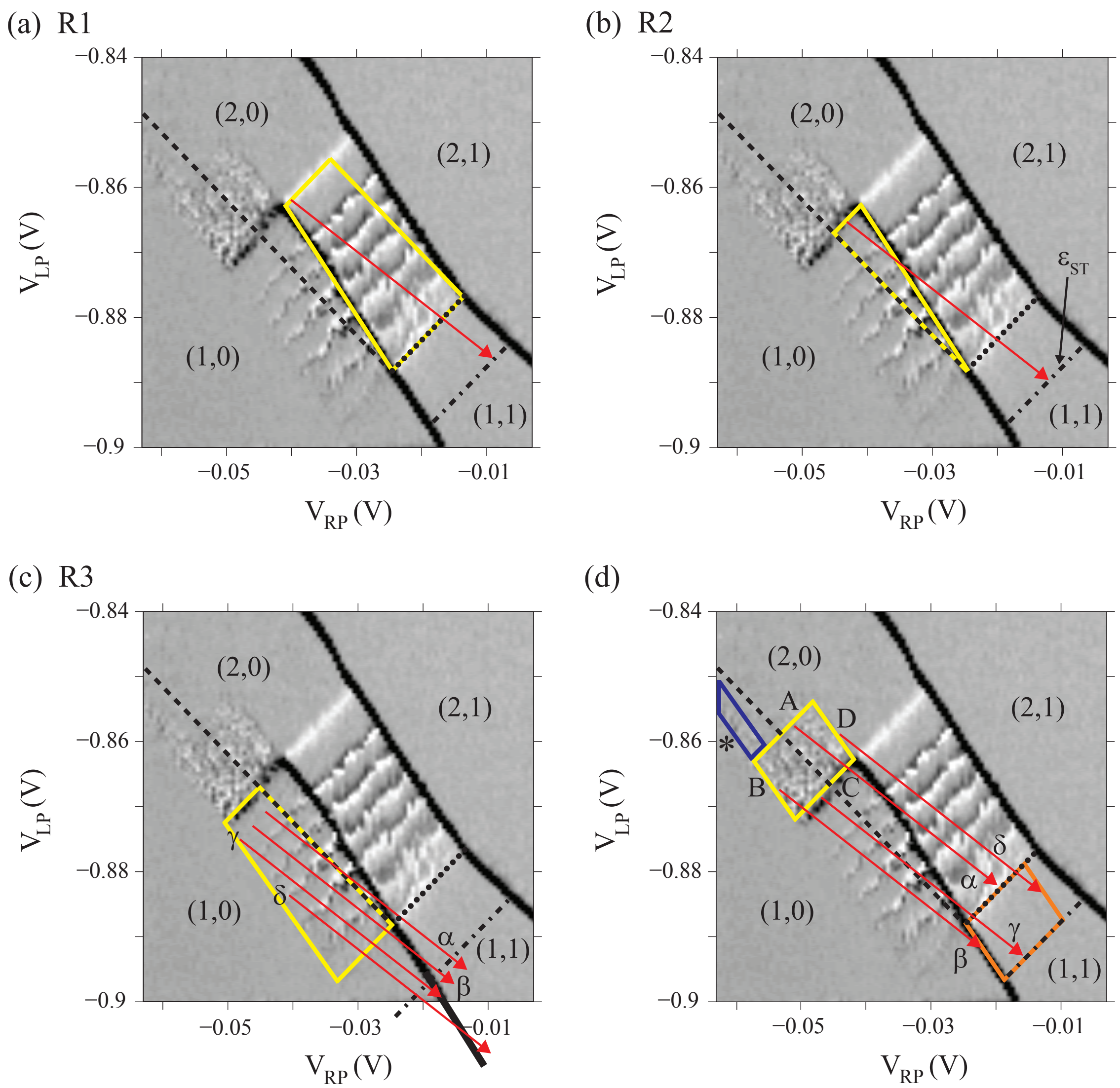

Figure 4.8: (a) [(b),(c)] LZS oscillations in region R1 [R2,R3] are outlined. (d) Fluctuations between the (1,0) and (2,0) charge states produce bounded regions of noise in R2 and R3 (A-D and $*$).

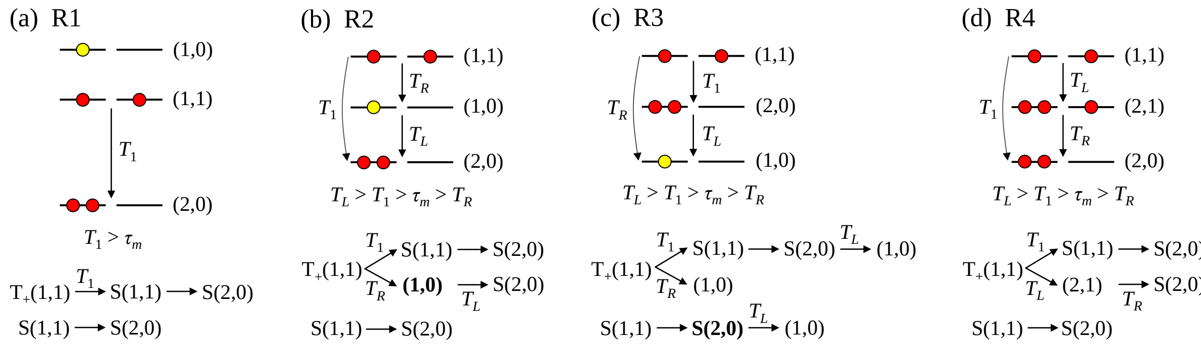

Figure 4.9: Energy level diagrams for regions (a) R1, (b) R2, (c) R3, and (d) R4 shown in Fig. 4.7(b). Pathways from the qubit states to the ground state are also shown (metastable states in bold). Spin-to-charge conversion in each region maps one of the qubit states to an excited charge state that is long-lived relative to τ_m.

ground state before it can decay to the first excited state, $S(2,0)$. The measured charge detector current is $I_{QPC} = I(1,0)$ in this case. Readout of $S(1,1)$ again involves a transition to $S(2,0)$. In R3, however, $S(2,0)$ is a metastable excited state due to the long tunneling time for the left dot, T_L. Since $\tau_m < T_L$, $S(1,1)$ is mapped to the (2,0) charge state and $I_{QPC} = I(2,0)$.

For region R4, (2,0) is the ground state while (2,1) and (1,1) are excited states as shown in the energy level diagram of Fig. 4.9(d). In this case, T_1 is short relative to the tunneling time T_L required for the transition of $T_+(1,1)$ to the (2,1) first excited state. Therefore, unlike in R2 and R3, the first excited state is not involved in the spin state readout. As in R1, $T_+(1,1)$ is mapped to (1,1), $S(1,1)$ is mapped to (2,0) and as result, the LZS oscillations in R4 appear identical to those in R1. Of course for a different choice of lead tunnel couplings, the (2,1) excited state could become a metastable charge state and be incorporated into the spin state readout as demonstrated in Ref. [23].

In regions R2 and R3, spin-to-charge conversion involves mapping $T_+(1,1)$ to the single electron state (1,0). Once (1,0) is occupied, an electron must be added to the DQD to create a two-electron spin state and initiate LZS processes again. In region R2, the system may decay to the (2,0) ground state during the period between pulses. Alternatively, since the tunneling time between the right dot and its lead $T_R < 50$ ns is comparable to or less than the pulse duration $\tau = 17$ ns, the system may transition to the (1,1) state during the segment of a pulse spent in the (1,1) ground state region. For region R3, since (1,0) is the ground state, an electron is added when a pulse enters the (1,1) ground state region. Examples of such pulses are labeled α and β in Fig. 4.8(c). Because the tunneling time between the left dot and its lead is long relative to the pulse duration, an electron is unlikely to be loaded into the DQD during the segment of pulse α spent in the (2,0) ground state region. The oscillations stop at the lower left boundary of R3 because for initial points on the boundary, pulses such as the one labeled γ just reach the addition line separating the (1,0) and (1,1) ground state regions. For initial points to the left of this boundary, an electron cannot be added to the right dot during a pulse.

Note that for pulse trajectories such as δ in Fig. 4.8(c) which start near the lower left boundary of R3, the system sweeps through an extension [into the (1,0) ground state region] of the S-T_+ avoided crossing. The existence of LZS oscillations near the lower left boundary, which run parallel to those in the rest of the stability diagram, indicates that an avoided crossing of the S and T_+ spin states of the excited charge state (1,1) exists within the (1,0) ground state region.

Fig. 4.10 shows QPC transconductance data measured along the lines labeled ε_1, ε_2, and ε_3 in Fig. 4.7(b). Plunger gate pulse duration is varied along the horizontal axis. Note that the pulse amplitude increases as the duration increases until full amplitude is attained at ~17 ns. This is the result of constructing the pulses to all have the same slew rate. Pulses with $\tau < 17$ ns duration do not rise to full amplitude before the falling edge begins. At full amplitude, a pulse has ~8 ns rise and fall times. Observe that the fringe (furthest from the charge transfer line) corresponding to incoherent mixing of the S and T_+ states is white in R1 and black in R2 and R3. In fact, close examination reveals that the coherent oscillations in R2 and R3 are also π phase shifted relative to those of R1. The source of this phase shift lies in the use of the (1,0) metastable state for spin-to-charge conversion in R2 and R3. Note that since the charge detector is closer to the right dot than the left dot $I(1{,}0) > I(2{,}0) > I(1{,}1)$. In region R1, a change from measuring a singlet to a triplet state creates a change in QPC current $\Delta I_{QPC} = I(1{,}1) - I(2{,}0) < 0$ while in regions R2 and R3, the resulting change is $\Delta I_{QPC} = I(1{,}0) - I(2{,}0) > 0$. This difference in the sign of ΔI_{QPC} leads to a difference in the sign of the transconductance signal, dI_{QPC}/dV_{LP}, and the observed π phase shift.

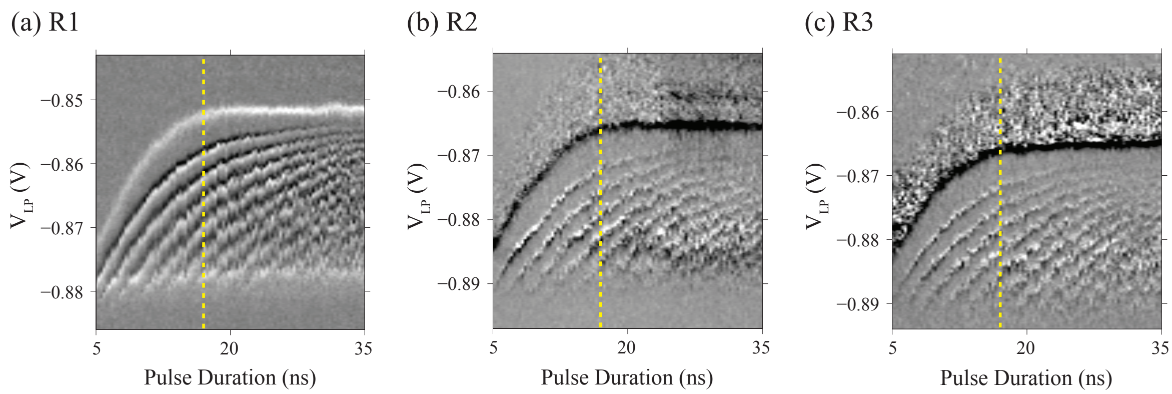

Figure 4.10: QPC transconductance as a function of initial detuning along V_{LP} and pulse duration for regions R1, R2, and R3. The vertical axes are projections onto the V_{LP} axis of the trajectories labeled ε_1, ε_2, and ε_3 in Fig. 4.7(b) (differences between the vertical axis gate voltages and those expected from Fig. 4.7(b) are due to device drift).

4.6.3 Telegraph Noise produced by the LZS Pulse

In addition to the LZS oscillations in R2 and R3, there is also a region of telegraph noise. Although such bounded regions of noise can result from the absorption of phonons produced by a biased QPC charge detector [100], this particular noise region is a result of the plunger gate pulses. It divided into two parts in Fig. 4.8(d). The parallelogram shaped region with boundaries labeled A-D is mapped by the pulses (arrows) to an area within the (1,1) ground state region of the stability diagram that lies between the charge transfer line (dot) and the S-T_+ avoided crossing (dash-dot). The noise spans across both R2 and R3 but in both cases, the underlying mechanism involves transitions between the (2,0) and (1,0) charge states. To observe the noise using the low-bandwidth DC-QPC charge detector requires a metastable state to slow down the transitions to the ground state. In the R3 case, for example, (1,0) is the ground state and (2,0) is the metastable first excited state. Access to the (2,0) state, however, first requires a transition to the (1,1) second excited state. This occurs during the segment of the pulse spent in the mapped area of the (1,1) region of the stability diagram. Note that the (1,1) excited state can be either a triplet T(1,1) or a singlet S(1,1). If T(1,1) is created, the system will relax to (1,0) after the pulse. If the system occupies S(1,1), a transition to the (2,0) metastable charge state will follow. Since S(1,1) and T(1,1) occur randomly, the noise is observed. The noise stops at boundary A because the associated pulse α does not reach the (1,1) region. At boundary C, the pulse labeled γ just reaches the the S-T_+ avoided crossing and the oscillations begin. Pulse β connects boundary B to the right dot addition line separating the (1,0) and (1,1) ground state regions. Along this addition line, the (1,0) and (1,1) states are degenerate and the pulse therefore provides a means by which the system can transition out of the (1,0) ground state of R3 and into the (1,1) second excited state. Since the pulse continues to reach the addition line for initial points up the V_{LP} axis, noise is observed within the outlined region labeled $\ast$. Finally, boundary D, located on the extension of the addition line separating the (1,0) and (1,1) ground state regions, is connected by pulse δ to the area between the charge transfer line and the S-T_+ avoided crossing. To the right of this boundary, there is no long-lived metastable state, so any fluctuations are suppressed due to fast relaxation to the ground state.

4.7 Ground State Initialization

Consider the dashed triangle on the stability of Fig. 4.11 formed by the charge transfer line and the extensions of the (1,0)↔(1,1) and (1,1)↔(2,1) addition lines. Conventional operation of the S-T_+ (R1 of Fig. 4.7) and S-T_0 qubits involves applying a gate voltage pulse (arrow) that sweeps the system from point M, within the triangle, to point P in the (1,1) region and back to point M for readout of the final spin state. As explained in Section 4.6.2, within the triangle, transitions between an excited state triplet T(1,1) and the singlet ground state S(2,0) are blocked for $T_1 \approx 100$ μs, allowing standard spin-to-charge conversion at point M. Outside the triangle, in the absence of metastable charge states, the spin blockade condition is usually lifted due to exchange of electrons with the leads [41, 52]. Of course after spin state readout, the system occupies either the ground state S(2,0) or the excited state T(1,1). If the final spin state is T(1,1) and decay to S(2,0) does not occur during the period between pulses, τ_m, the next pulse begins with the system still in T(1,1).

To simplify theoretical analysis, usually it is desirable to prevent this possibility and instead initialize to S(2,0) before each pulse. Such a procedure requires applying another gate voltage pulse, called an initialization pulse, which configures the system to briefly lift the spin blockade condition. This initialization pulse moves the system from M to $\mathrm{I_n}$ and then back to M before sweeping to P. At initialization point $\mathrm{I_1}$, located outside the dashed triangle, (1,0) is lower in energy than (1,1), allowing a spin independent path to the ground state via the process T(1,1) → (1,0) → S(2,0). This is a commonly employed technique of singlet state initialization [101, 102, 103]. Although uncommon, choosing point $\mathrm{I_2}$ also lifts the spin blockade condition by the process T(1,1) → (2,1) → S(2,0), again by exchange of electrons with the leads. Deeper into the (2,0) region at point $\mathrm{I_3}$, T(2,0) is accessible and a transition to the ground state by the process T(1,1) → T(2,0) → (1,0) → S(2,0) is possible [104]. Lastly, initialization can also be accomplished by sweeping into a neighboring charge state. At $\mathrm{I_4}$, the system transitions to the (1,0) ground state. In the process of returning to M, an electron is added to the left dot, creating the S(2,0) ground state. A similar argument can be made for $\mathrm{I_5}$.

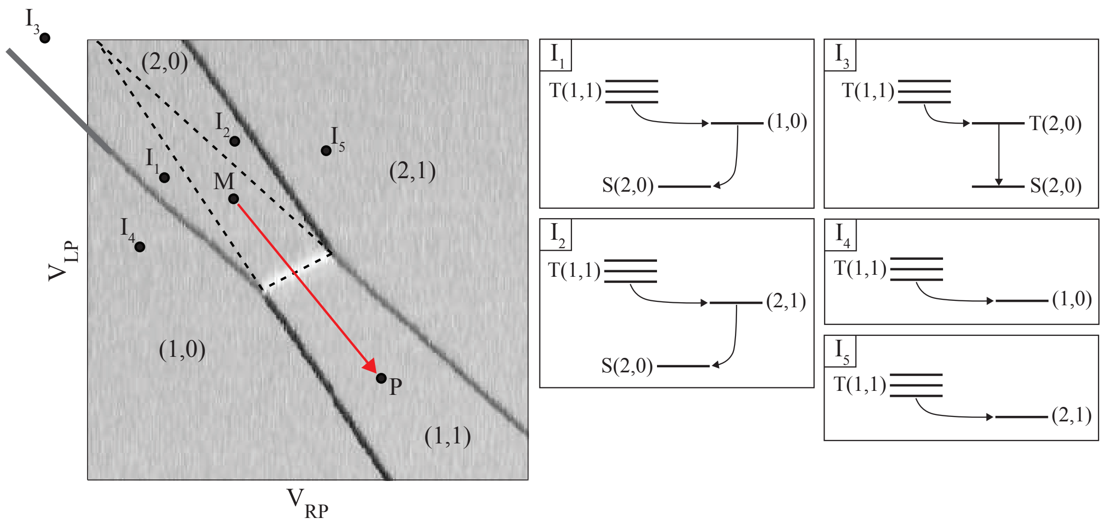

Figure 4.11: Standard spin-to-charge conversion is possible within the dashed triangle of the (2,0) region. The arrow represents a pulse from M, within the triangle, to P in the (1,1) region. Between each pulse, initialization to S(2,0) is accomplished by sweeping the system to one of the points $\mathrm{I_n}$ where the spin blockade condition is lifted.

4.7.1 LZS Oscillations without Applied Initialization

Motivated by the potential difficulty of implementing such state initialization techniques in a complex quantum dot circuit with nearly isolated inner dot electrons (eg. linear triple dot), the NRC group has studied both theoretically and experimentally S-T_+ LZS oscillations without applied initialization in a DQD [105]. Numerical calculations from Ref. [105] are displayed in Fig. 4.12(a). The probability of measuring $S(2,0)$ after the LZS pulse, $P(S)$, as a function of initial detuning (position of point M) is shown for both initialization and non-initialization cases. For the purposes of this discussion, simply note the waveform shape in both cases. With initialization, the oscillations are sinusoidal while without initialization they contain sharp peaks centered on the points for which $P(S) = 1$. Theoretical and experimental LZS oscillations in the non-initialization case for various measurement periods, τ_m, are displayed in Fig. 4.12(b) and (c) respectively. Again these results are from Ref. [105]. In the experimental case, T_1 is in the range 20-60 μs while

T_1 = 60 μs for the calculations. Note that as the ratio τ_m/T_1 increases, the waveform of the oscillations approaches sinusoidal in the sense that the bright and dark regions for some of the largest τ_m/T_1 cases have approximately equal widths along the detuning axis. This indicates that even without an initialization procedure in the form of a gate voltage pulse, partial initialization occurs between the pulses simply due to relaxation to the ground state.

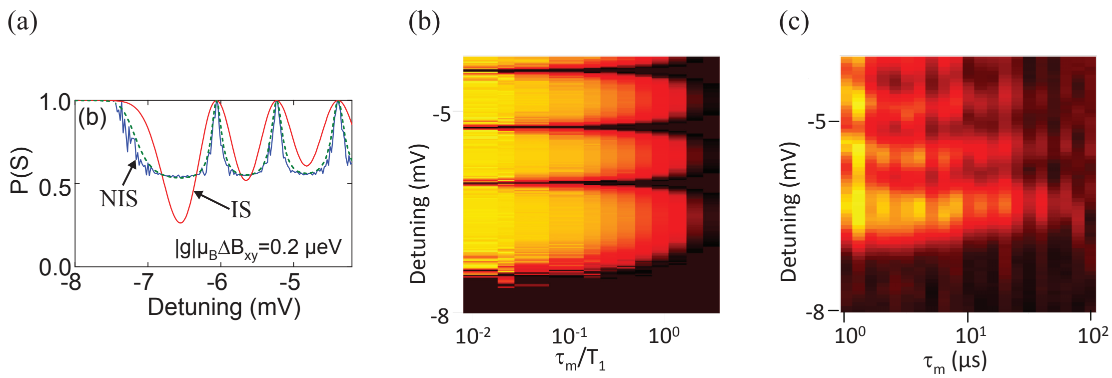

Figure 4.12: (a) Calculated probability of measuring a singlet after a pulse, $P(S)$, as a function of detuning (IS - with initialization step, NIS - no initialization step) (b) Calculations showing $P(S)$ as a function of detuning for various values of τ_m/T_1. (c) Experimental data of $P(S)$ as a function of detuning and τ_m. Similar to (b), for some of the larger values of τ_m, initializing to the ground state singlet via T_1-relaxation produces oscillations with a sinusoidal character. Reprinted figures with permission from Granger et al., Physical Review B **91**, 115309 (2015). Copyright (2015) by the American Physical Society.

The S-T_+ qubit data discussed in Section 4.6.2 is acquired without an initialization procedure.[1] Line scans taken at the positions of the dashed lines in Fig. 4.10(a), (b), (c) are displayed in Fig. 4.13(a), (b), and (c) respectively. Note that I_{QPC} is proportional to $P(S)$ but that this data is QPC transconductance, dI_{QPC}/dV_{LP}. Each sharp peak in $P(S)$ for the non-initialization case of Fig. 4.12(a) corresponds to a sharp dip followed by a sharp

[1] Of course the tunnel rates and resulting metastable charge states prevent using several of the initialization procedures outlined in Fig. 4.11.

peak in transconductance. Even though $\tau_m = 2\ \mu$s, $T_1 \approx 100\ \mu$s and thus $\tau_m/T_1 \approx 0.02$, the oscillations in R1 appear nearly sinusoidal. There are, however, markedly nonsinusoidal oscillations in regions R2 and R3. Since $T_+(1,1)$ is mapped to (1,0) in regions R2 and R3, the relaxation time in R1, T_1, associated with coupling to the nuclear spin bath, is replaced by the much longer metastable relaxation time T_L. With $\tau_m/T_L \approx 10^{-5}$, the nonsinusoidal waveform is clearly apparent.

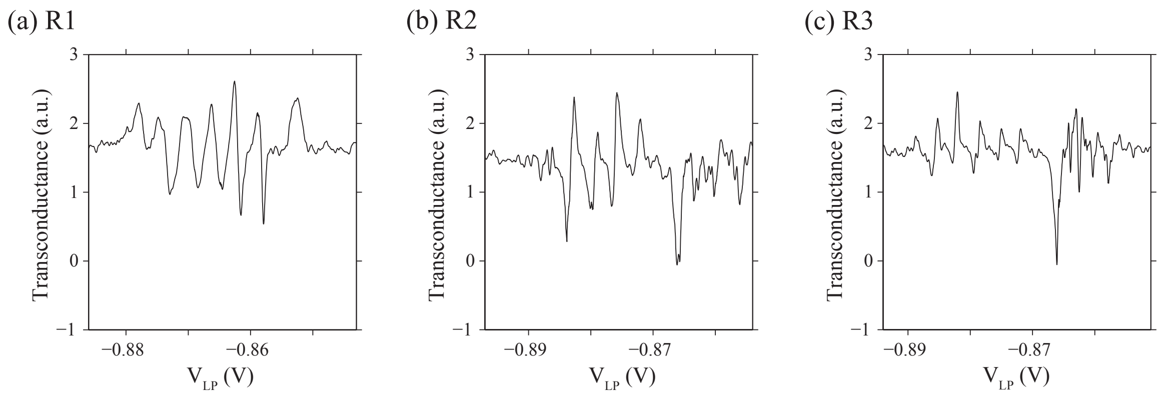

Figure 4.13: Line scans taken at the positions of the vertical dashed lines in Fig. 4.10.

4.7.2 Boxcar Integrator

As alluded to above, ground state initialization can be accomplished by simply waiting at point M between LZS pulses for the system to relax to the ground state. Because the transition $T_+(1,1) \rightarrow S(1,1) \rightarrow S(2,0)$ occurs in a time of order $T_1 \approx 100\ \mu$s, a delay between pulses of approximately $5T_1 \approx 500\ \mu$s needs to be added to the pulse period τ_m. Instead of continuously measuring the output of the charge detector during this longer τ_m, the signal-to-noise can be improved by measuring only immediately after the pulse. This is accomplished using a boxcar integrator (eg. Standford Research Systems, model SR250). An associated timing diagram is shown in Fig. 4.14(a). The Gaussian pulse is applied and the charge detector signal is measured for t_m, a few μs. The remainder of τ_m is the wait time, t_w, during which the charge detector signal is not sampled. The boxcar integrator averages the results of 10^4 such cycles. Since the DC-QPC has a bandwidth of 25 kHz, it takes approximately 1/25 kHz = 40 μs after the LZS pulse before the charge detector registers a response. Measuring in the first few μs immediately after the pulse is thus not possible with the DC-QPC readout. The RF-QPC with its ~100 ns response time (i.e. 15 MHz bandwidth) is required for these boxcar measurements. Fig. 4.14(b) shows a first attempt to use the boxcar integrator with the RF-QPC to measure LZS oscillations. In this case, τ_m = 100 μs and t_m = 3 μs. The charging lines are drawn on the stability diagram. They do not show in the data because the boxcar is operated in AC coupled mode (> 10 Hz).

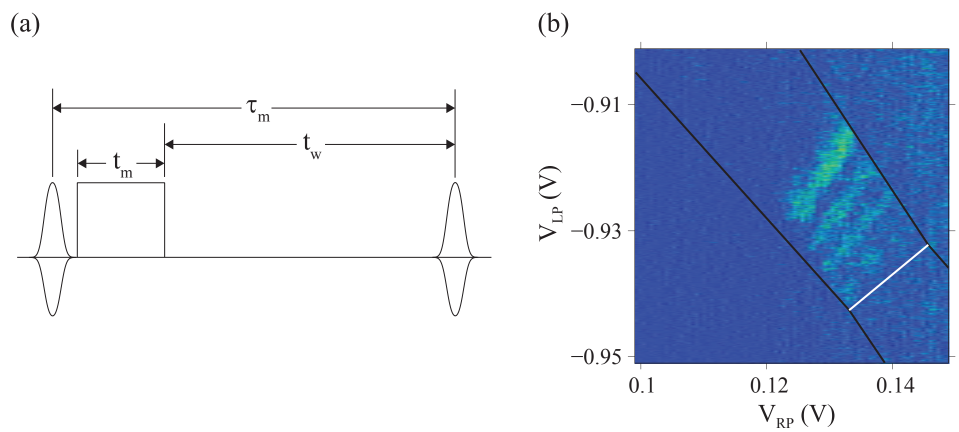

Figure 4.14: (a) Timing diagram for an LZS measurement involving the RF-QPC and the boxcar integrator. Immediately after the Gaussian pulse, the boxcar samples the charge detector signal for a time t_m. A wait time, t_w allows for T_1 decay of a T_+(1,1) excited state to the S(2,0) ground state before the next pulse. (b) Stability diagram acquired with the RF-QPC and boxcar (t_m = 3 μs; LZS pulse: τ = 17 ns, s = 4 ns, τ_m = 100 μs).

4.8 Conclusions and Future Work

Operation of the S-T_+ qubit in a DQD has been demonstrated. For a DQD with asymmetric couplings to the leads, spin-to-charge conversion involving a metastable charge state is possible. Combining this qubit readout technique with Gaussian pulses that do not contain a ground state initialization step produces non-sinusoidal LZS oscillations. If the response time of the QPC readout is comparable to the lifetime of the metastable state, telegraph noise associated with the LZS pulse is observed in the charge stability diagram.

References

[1] S. Guéron, M. M. Deshmukh, E. B. Myers, and D. C. Ralph. Tunneling via Individual Electronic States in Ferromagnetic Nanoparticles. *Physical Review Letters*, 83:4148, 1999.

[2] S. J. Chorley, J. Wabnig, Z. V. Penfold-Fitch, K. D. Petersson, J. Frake, C. G. Smith, and M. R. Buitelaar. Measuring the Complex Admittance of a Carbon Nanotube Double Quantum Dot. *Physical Review Letters*, 108:036802, 2012.

[3] M. D. Schroer, K. D. Petersson, M. Jung, and J. R. Petta. Field Tuning the g Factor in InAs Nanowire Double Quantum Dots. *Physical Review Letters*, 107:176811, 2011.

[4] D. Loss and D. P. DiVincenzo. Quantum computation with quantum dots. *Physical Review A*, 57:120, 1998.

[5] C. Kloeffel and D. Loss. Propects for Spin-Based Quantum Computing in Quantum Dots. *Annual Review of Condensed Matter Physics*, 4:51, 2013.

[6] D. Divincenzo. The Physical Implementation of Quantum Computation. *Fortschritte der Physik*, 48:771, 2000.

[7] R. Brunner, Y.-S. Shin, T. Obata, M. Pioro-Ladrière, T. Kubo, K. Yoshida, T. Taniyama, Y. Tokura, and S. Tarucha. Two-Qubit Gate of Combined Single-Spin Rotation and Interdot Spin Exchange in a Double Quantum Dot. *Physical Review Letters*, 107:146801, 2011.

[8] S. Amasha, K. Maclean, Iuliana P. Radu, D. M. Zumbühl, M. A. Kastner, M. P. Hanson, and A. C. Gossard. Electrical Control of Spin Relaxation in a Quantum Dot. *Physical Review Letters*, 100:046803, 2008.

[9] F. H. L. Koppens, K. C. Nowack, and L. M. K. Vandersypen. Spin Echo of a Single Electron Spin in a Quantum Dot. *Physical Review Letters*, 100:236802, 2008.

[10] M. Pioro-Ladrière, T. Obata, Y. Tokura, Y.-S. Shin, T. Kubo, K. Yoshida, T. Taniyama, and S. Tarucha. Electrically driven single-electron spin resonance in a slanting Zeeman field. *Nature Physics*, 4:776, 2008.

[11] J. R. Petta, A. C. Johnson, J. M. Taylor, E. A. Laird, A. Yacoby, M. D. Lukin, C. M. Marcus, M. P. Hanson, and A. C. Gossard. Coherent Manipulation of Coupled Electron Spins in Semiconductor Quantum Dots. *Science*, 309:2180, 2005.

[12] E. Knill, R. Laflamme, and W. H. Zurek. Resilient quantum computation. *Science*, 279:342, 1998.

[13] D. Aharonov and M. Ben-Or. Fault-tolerant quantum computation with constant error rate. *SIAM Journal on Computing*, 38:1207, 2008.

[14] R. Hanson, L. P. Kouwenhoven, J. R. Petta, S. Tarucha, and L. M. K. Vandersypen. Spins in few-electron quantum dots. *Reviews of Modern Physics*, 79:1217, 2007.

[15] S. Foletti, H. Bluhm, D. Mahalu, V. Umansky, and A. Yacoby. Universal quantum control of two-electron spin quantum bits using dynamic nuclear polarization. *Nature Physics*, 5:903, 2009.

[16] I. van Weperen, B. D. Armstrong, E. A. Laird, J. Medford, C. M. Marcus, M. P. Hanson, and A. C. Gossard. Charge-State Conditional Operation of a Spin Qubit. *Physical Review Letters*, 107:030506, 2011.

[17] M. D. Shulman, O. E. Dial, S. P. Harvey, H. Bluhm, V. Umansky, and A. Yacoby. Demonstration of Entanglement of Electrostatically Coupled Singlet-Triplet Qubits. *Science*, 336:202, 2012.

[18] R. Hanson, L. H. Willems van Beveren, I. T. Vink, J. M. Elzerman, W. J. M. Naber, F. H. L. Koppens, L. P. Kouwenhoven, and L. M. K. Vandersypen. Single-Shot Readout of Electron Spin States in a Quantum Dot Using Spin-Dependent Tunnel Rates. *Physical Review Letters*, 94:196802, 2005.

[19] H. Bluhm, S. Foletti, I. Neder, M. Rudner, D. Mahalu, V. Umansky, and A. Yacoby. Dephasing time of GaAs electron-spin qubits coupled to a nuclear bath exceeding 200 μs. *Nature Physics*, 7:109, 2011.

[20] J. R. Petta, H. Lu, and A. C. Gossard. A Coherent Beam Splitter for Electronic Spin States. *Science*, 327:669, 2010.

[21] H. Ribeiro, J. R. Petta, and G. Burkard. Harnessing the GaAs quantum dot nuclear spin bath for quantum control. *Physical Review B*, 82:115445, 2010.

[22] L. Gaudreau, G. Granger, A. Kam, G. C. Aers, S. A. Studenikin, P. Zawadzki, M. Pioro-Ladrière, Z. R. Wasilewski, and A. S. Sachrajda. Coherent control of three-spin states in a triple quantum dot. *Nature Physics*, 8:54, 2012.

[23] S. A. Studenikin, J. Thorgrimson, G. C. Aers, A. Kam, P. Zawadzki, Z. R. Wasilewski, A. Bogan, and A. S. Sachrajda. Enhanced charge detection of spin qubit readout via an intermediate state. *Applied Physics Letters*, 101:233101, 2012.

[24] M. Field, C. G. Smith, M. Pepper, D. A. Ritchie, J. E. F. Frost, G. A. C. Jones, and D. G. Hasko. Measurements of Coulomb Blockade with a Noninvasive Voltage Probe. *Physical Review Letters*, 70:1311, 1993.

[25] K. Ono, D. G. Austing, Y. Tokura, and S. Tarucha. Current Rectification by Pauli Exclusion in a Weakly Coupled Double Quantum Dot System. *Science*, 297:1313, 2002.

[26] D. J. Reilly, C. M. Marcus, M. P. Hanson, and A. C. Gossard. Fast single-charge sensing with a rf quantum point contact. *Applied Physics Letters*, 91:162101, 2007.

[27] M. C. Cassidy, A. S. Dzurak, R. G. Clark, K. D. Petersson, I. Farrer, D. A. Ritchie, and C. G. Smith. Single shot charge detection using a radio-frequency quantum point contact. *Applied Physics Letters*, 91:222104, 2007.

[28] G. Grosso and G. P. Parravicini. *Solid State Physics*. Academic Press, Toronto, 2000.

[29] J. H. Davies. *The Physics of Low-Dimensional Semiconductors*. Cambridge University Press, New York, 1998.

[30] S. Datta. *Electronic Transport in Mesoscopic Systems*. Cambridge University Press, New York, 1995.

[31] W. G. van der Wiel, S. De Franceschi, J. M. Elzerman, T. Fujisawa, S. Tarucha, and L. P. Kouwenhoven. Electron transport through double quantum dots. *Reviews of Modern Physics*, 75:1, 2003.

[32] T. Ihn. *Semicondutor Nanostructures: Quantum States and Electronic Transport*. Oxford University Press, New York, 2010.

[33] B. J. van Wees, H. van Houten, C. W. J. Beenakker, J. G. Williamson, L. P. Kouwenhoven, D. van der Marcel, and C. T. Foxon. Quantized Conductance of Point Contacts in a Two-Dimensional Electron Gas. *Physical Review Letters*, 60:848, 1988.

[34] D. A. Wharam, T. J. Thornton, R. Newbury, M. Pepper, H. Ahmed, J. E. F. Frost, D. G. Hasko, D. C. Peacock, D. A. Ritchie, and G. A. C. Jones. One-dimensional transport and the quantisation of the ballistic resistance. *Journal of Physics C*, 21:L209, 1988.

[35] Y. V. Nazarov and Y. M. Blanter. *Quantum Transport: Introduction to Nanoscience*. Cambridge University Press, New York, 2009.

[36] M. Ciorga, A. S. Sachrajda, P. Hawrylak, C. Gould, P. Zawadzki, S. Jullian, Y. Feng, and Z. Wasilewski. Addition spectrum of a lateral dot from Coulomb and spin-blockade spectroscopy. *Physical Review B*, 61:R16315, 2000.

[37] J. M. Elzerman, R. Hanson, J. S. Greidanus, L. H. Willems van Beveren, S. De-Franceschi, L. M. K. Vandersypen, S. Tarucha, and L. P. Kouwenhoven. Few-electron quantum dot circuit with integrated charge read out. *Physical Review B*, 67:161308, 2003.

[38] L. M. K. Vandersypen, J. M. Elzerman, R. N. Schouten, L. H. Willems van Beveren, R. Hanson, and L. P. Kouwenhoven. Real-time detection of single-electron tunneling using a quantum point contact. *Applied Physics Letters*, 85:4394, 2004.

[39] D. Taubert, D. Schuh, W. Wegscheider, and S. Ludwig. Determination of energy scales in few-electron double quantum dots. *Review of Scientific Instruments*, 82:123905, 2011.

[40] A. C. Johnson, J. R. Petta, and C. M. Marcus. Singlet-triplet spin blockade and charge sensing in a few-electron double quantum dot. *Physical Review B*, 72:165308, 2005.

[41] A. C. Johnson, J. R. Petta, J. M. Taylor, A. Yacoby, M. D. Lukin, C. M. Marcus, M. P. Hanson, and A. C. Gossard. Triplet-singlet spin relaxation via nuclei in a double quantum dot. *Nature*, 435:925, 2005.

[42] A. B. Zorin. The thermocoax cable as the microwave frequency filter for single electron circuits. *Review of Scientific Instruments*, 66:4296, 1995.

[43] K. Bladh, D. Gunnarsson, E. Hürfeld, S. Devi, C. Kristoffersson, B. Smålander, S. Pehrson, T. Claeson, and P. Delsing. Comparison of cryogenic filters for use in single electronics experiments. *Review of Scientific Instruments*, 74:1323, 2003.

[44] A. Fukushima, A. Sato, A. Iwasa, Y. Nakamura, T. Komatsuzaki, and Y. Sakamoto. Attenuation of Microwave Filters for Single-Electron Tunneling Experiments. *IEEE Transactions on Instrumentation and Measurement*, 46:289, 1997.

[45] J. M. Martinis, M. H. Devoret, and J. Clarke. Experimental tests for the quantum behavior of a macroscopic degree of freedom: The phase difference across a Josephson junction. *Physical Review B*, 35:4682, 1987.

[46] A. Lukashenko and A. V. Ustinov. Improved powder filters for qubit measurements. *Review of Scientific Instruments*, 79:014701, 2008.

[47] F. P. Milliken, J. R. Rozen, G. A. Keefe, and R. H. Koch. 50 Ω characteristic impedance low-pass metal powder filters. *Review of Scientific Instruments*, 78:024701, 2007.

[48] C. W. J. Beenakker. Theory of Coulomb-blockade oscillations in the conductance of a quantum dot. *Physical Review B*, 44:1646, 1991.

[49] E. B. Foxman, P. L. McEuen, U. Meirav, N. S. Wingreen, Y. Meir, P. A. Belk, N. R. Belk, and M. A. Kastner. Effects of quantum levels on transport through a Coulomb island. *Physical Review B*, 47:10020, 1993.

[50] L. DiCarlo, H. J. Lynch, A. C. Johnson, L. I. Childress, K. Crockett, and C. M. Marcus. Differential Charge Sensing and Charge Delocalization in a Tunable Double Quantum Dot. *Physical Review Letters*, 92:226801, 2004.

[51] J. R. Petta, A. C. Johnson, C. M. Marcus, M. P. Hanson, and A. C. Gossard. Manipulation of a Single Charge in a Double Quantum Dot. *Physical Review Letters*, 93:186802, 2004.

[52] J. R. Petta, A. C. Johnson, A. Yacoby, C. M. Marcus, M. P. Hanson, and A. C. Gossard. Pulsed-gate measurements of the singlet-triplet relaxation time in a two-electron double quantum dot. *Physical Review B*, 72:161301, 2005.

[53] I. T. Vink, T. Nooitgedagt, R. N. Schouten, and L. M. K. Vandersypen. Cryogenic amplifier for fast real-time detection of single-electron tunneling. *Applied Physics Letters*, 91:123512, 2007.

[54] R. J. Schoelkopf, P. Wahlgren, A. A. Kozhevnikov, P. Delsing, and D. E. Prober. The Radio-Frequency Single-Electron Transistor (RF-SET): A Fast and Ultrasensitive Electrometer. *Science*, 280:1238, 1998.

[55] T. Müller, T. Choi, S. Hellmüller, K. Ensslin, T. Ihn, and S. Schön. A circuit analysis of an in situ tunable radio-frequency quantum point contact. *Review of Scientific Instruments*, 84:083902, 2013.

[56] J. Love. *Resolved Dynamics of Single Electron Tunneling Using the RF-SET*. PhD thesis, Yale University, 2007.

[57] J. Teufel. *Superconducting Tunnel Junctions as Direct Detectors for Submillimeter Astronomy*. PhD thesis, Yale University, 2008.

[58] L. Roschier, P. Hakonen, K. Bladh, P. Delsing, K. W. Lehnert, L. Spietz, and R. J. Schoelkopf. Noise performance of the radio-frequency single-electron transistor. *Journal of Applied Physics*, 95:1274, 2004.

[59] D. M. Pozar. *Microwave Engineering*. Addison-Wesley, New York, 1990.

[60] W. W. Xue, B. Davis, F. Pan, J. Stettenheim, T. J. Gilheart, A. J. Rimberg, and Z. Ji. On-chip matching networks for radio-frequency single-electron transistors. *Applied Physics Letters*, 91:093511, 2007.

[61] A. Aassime, D. Guannarsson, K. Bladh, P. Delsing, and R. Schoelkopf. Radio-frequency single-electron transistor: Toward the shot-noise limit. *Applied Physics Letters*, 79:4031, 2001.

[62] W. Schottky. *Annals of Physics (Leipzig)*, 57:541, 1918.

[63] Th. Martin and R. Landauer. Wave-packet approach to noise in multichannel mesoscopic systems. *Physical Review B*, 45:1742, 1992.

[64] V. K. Khlus. Current and voltage fluctuations in microjunctions between normal metals and superconductors. *Soviet Journal of Experimental and Theoretical Physics*, 66:1243, 1987.

[65] G. B. Lesovik. Excess quantum noise in 2D ballistic point contacts. *JETP Letters*, 49:592, 1989.

[66] A. Kumar, L. Saminadayar, D. C. Glatti, Y. Jin, and B. Etienne. Experimental Test of the Quantum Shot Noise Reduction Theory. *Physical Review Letters*, 76:2778, 1996.

[67] M. Reznikov, R. De Picciotto, M. Heiblum, D. C. Glatti, A. Kumar, and L. Saminadayar. Quantum shot noise. *Superlattices and Microstructures*, 23:901, 1998.

[68] S. Haykin. *An Introduction to Analog and Digital Communications.* Wiley, Toronto, 1989. Chapter 4, Example 4, Eq. 4.52.

[69] M. Pioro-Ladrière, J. H. Davies, A. R. Long, A. S. Sachrajda, L. Gaudreau, P. Zawadzki, J. Lapointe, J. Gupta, Z. Wasilewski, and S. Studenikin. Origin of switching noise in GaAs/$Al_xGa_{1-x}As$ lateral gated devices. *Physical Review B*, 72:115331, 2005.

[70] T. Müller, B. Küng, S. Hellmüller, P. Studerus, K. Ensslin, T. Ihn, M. Reinwald, and W. Wegscheider. An in situ tunable radio-frequency quantum point contact. *Applied Physics Letters*, 97:202104, 2010.

[71] C. Barthel, M. Kjærgaard, J. Medford, M. Stopa, C. M. Marcus, M. P. Hanson, and A. C. Gossard. Fast sensing of double-dot charge arrangement and spin state with a radio-frequency sensor quantum dot. *Physical Review B*, 81:161308, 2010.

[72] M. Yuan, Z. Yang, D. E. Savage, M. G. Lagally, M. A. Eriksson, and A. J. Rimberg. Charge sensing in a Si/SiGe quantum dot with a radio frequency superconducting single-electron transistor. *Applied Physics Letters*, 101:142103, 2012.

[73] W. Lu, Z. Ji, L. Pfeiffer, K. W. West, and A. J. Rimberg. Real-time detection of electron tunnelling in a quantum dot. *Nature*, 423:422, 2003.

[74] K. D. Petersson, C. G. Smith, D. Anderson, P. Atkinson, G. A. C. Jones, and D. A. Ritchie. Charge and Spin State Readout of a Double Quantum Dot Coupled to a Resonator. *Nano Letters*, 10:2789, 2010.

[75] J. I. Colless, A. C. Mahoney, J. M. Hornibrook, A. C. Doherty, H. Lu, A. C. Gossard, and D. J. Reilly. Dispersive Readout of a Few-Electron Double Quantum Dot with Fast rf Gate Sensors. *Physical Review Letters*, 110:046805, 2013.

[76] M. Nakahara and T. Ohmi. *Quantum Computing: From Linear Algebra to Physical Realizations*. CRC Press, Boca Raton, Florida, 2008.

[77] I. L. Chuang, L. M. K. Vandersypen, X. Zhou, D. W. Leung, and S. Lloyd. Experimental realization of a quantumm algorithm. *Nature*, 393:143, 1998.

[78] L. M. K. Vandersypen and I. L. Chuang. NMR techniques for quantum control and computation. *Reviews of Modern Physics*, 76:1037, 2004.

[79] J. Johansson, S. Saito, T. Meno, H. Nakano, M. Ueda, K. Semba, and H. Takayanagi. Vacuum Rabi Oscillations in a Macroscopic Superconducting Qubit LC Oscillator System. *Physical Review Letters*, 96:127006, 2006.

[80] D. Schrader, I. Dotsenko, M. Khudaverdyan, Y. Miroshnychenko, A. Rauschenbeutel, and D. Meschede. Neutral Atom Quantum Register. *Physical Review Letters*, 93:150501, 2004.

[81] J. Stehlik, Y. Dovzhenko, J. R. Petta, J. R. Johansson, F. Nori, H. Lu, and A. C. Gossard. Landau-Zener-Stückelberg interferometry of a single electron charge qubit. *Physical Review B*, 86:121303, 2012.

[82] J. M. Elzerman, R. Hanson, L. H. Willems van Beveren, B. Witkamp, L. M. K. Vandersypen, and L. P. Kouwenhoven. Single-shot read-out of an individual electron spin in a quantum dot. *Nature*, 430:431, 2004.

[83] F. Forster, G. Petersen, S. Manus, P. Hänggi, D. Schuh, W. Wegscheider, S. Kohler, and S. Ludwig. Characterization of Qubit Dephasing by Landau-Zener-Stückelberg-Majorana Interferometry. *Physical Review Letters*, 112:116803, 2014.

[84] E. A. Laird, J. M. Taylor, D. P. DiVincenzo, C. M. Marcus, M. P. Hanson, and A. C. Gossard. Coherent spin manipulation in an exchange-only qubit. *Physical Review B*, 82:075403, 2010.

[85] C. Zener. Non-adiabatic Crossing of Energy Levels. *Proceedings of the Royal Society*, A137:696, 1932.

[86] L. D. Landau and E. M. Lifshitz. *Quantum Mechanics: Non-Relativistic Theory.* Pergamon Press, Toronto, third edition, 1977.

[87] J. R. Rubbmark, M. M. Kash, M. G. Littman, and D. Kleppner. Dynamical effects at avoided level crossings: A study of the Landau-Zener effect using Rydberg atoms. *Physical Review A*, 23:3107, 1981.

[88] D. M. Zumbühl, C. M. Marcus, M. P. Hanson, and A. C. Gossard. Cotunneling Spectroscopy in Few-Electron Quantum Dots. *Physical Review Letters*, 93:256801, 2004.

[89] A. Brataas and E. I. Rashba. Nuclear dynamics during Landau-Zener singlet-triplet transitions in double quantum dots. *Physical Review B*, 84:045301, 2011.

[90] I. Neder, M. S. Rudner, H. Bluhm, S. Foletti, B. I. Halperin, and A. Yacoby. Semiclassical model for the dephasing of a two-electron spin qubit coupled to a coherently evolving nuclear spin bath. *Physical Review B*, 84:035441, 2011.

[91] H. Ribeiro, J. R. Petta, and G. Burkard. Interplay of charge and spin coherence in Landau-Zener-Stückelberg-Majorana interferometry. *Physical Review B*, 87:235318, 2013.

[92] E. Shimshoni and Y. Gefen. Onset of Dissipation in Zener Dynamics: Relaxation versus Dephasing. *Annals of Physics*, 210:16, 1991.

[93] Y. Kayanuma. Stokes phase and geometrical phase in a driven two-level system. *Physical Review A*, 55:R2495, 1997.

[94] A. V. Shytov, D. A. Ivanov, and M. V. Feigel'man. Landau-Zener interferometry for qubits. *The European Physical Journal B*, 36:263, 2003.

[95] M. Sillanpää, Teijo Lehtinen, A. Paila, Y. Makhlin, and P. Hakonen. Continuous-Time Monitoring of Landau-Zener Interference in a Cooper-Pair Box. *Physical Review Letters*, 96:187002, 2006.

[96] D. J. Reilly, J. M. Taylor, E. A. Laird, J. R. Petta, C. M. Marcus, M. P. Hanson, and A. C. Gossard. Measurement of Temporal Correlations of the Overhauser Field in a Double Quantum Dot. *Physical Review Letters*, 101:236803, 2008.

[97] D. J. Reilly, J. M. Taylor, J. R. Petta, C. M. Marcus, M. P. Hanson, and A. C. Gossard. Exchange Control of Nuclear Spin Diffusion in a Double Quantum Dot. *Physical Review Letters*, 104:236802, 2010.

[98] H. Ribeiro, G. Burkard, J. R. Petta, H. Lu, and A. C. Gossard. Coherent Adiabatic Spin Control in the Presence of Charge Noise Using Tailored Pulses. *Physical Review Letters*, 110:086804, 2013.

[99] J. D. Mason, S. A. Studenikin, A. Kam, Z. R. Wasilewski, A. S. Sachrajda, and J. B. Kycia. Role of metastable charge states in a quantum-dot spin-qubit readout. *Physical Review B*, 92:125434, 2015.

[100] D. Taubert, M. Pioro-Ladrière, D. Schröer, D. Harbusch, A. S. Sachrajda, and S. Ludwig. Telegraph Noise in Coupled Quantum Dot Circuits Induced by a Quantum Point Contact. *Physical Review Letters*, 100:176805, 2008.

[101] J. R. Petta, J. M. Taylor, A. C. Johnson, A. Yacoby, M. D. Lukin, C. M. Marcus, M. P. Hanson, and A. C. Gossard. Dynamic Nuclear Polarization with Single Electron Spins. *Physical Review Letters*, 100:067601, 2008.

[102] C. Barthel, D. J. Reilly, C. M. Marcus, M. P. Hanson, and A. C. Gossard. Rapid Single-Shot Measurement of a Singlet-Triplet Qubit. *Physical Review Letters*, 103:160503, 2009.

[103] C. Barthel, J. Medford, C. M. Marcus, M. P. Hanson, and A. C. Gossard. Interlaced Dynamical Decoupling and Coherent Operation of a Singlet-Triplet Qubit. *Physical Review Letters*, 105:266808, 2010.

[104] E. A. Laird, J. R. Petta, A. C. Johnson, C. M. Marcus, A. Yacoby, M. P. Hanson, and A. C. Gossard. Effect of Exchange Interaction on Spin Dephasing in a Double Quantum Dot. *Physical Review Letters*, 97:056801, 2006.

[105] G. Granger, G. C. Aers, S. A. Studenikin, A. Kam, P. Zawadzki, Z. R. Wasilewski, and A. S. Sachrajda. Visibility study of S-T_+ Landau-Zener-Stückelberg oscillations without applied initialization. *Physical Review B*, 91:115309, 2015.

[106] C. Cohen-Tannoudji, B. Diu, and F. Laloë. *Quantum Mechanics, Volume 1.* Wiley, New York, 1977.

Appendix A

Miscellaneous Issues with LZS Data

This section is a brief summary of LZS data that are not fully understood. It is included for the benefit of a future student working on a related project. Most of the discussion concerns various distortions in the LZS data.

Most of the data from a 2013 cooldown is of the type shown in Fig. A.1(a). This stability diagram is constructed by starting in the bottom left corner and sweeping bottom to top and stepping left to right. That is, V_{LP} is changed on the inner loop and V_{RP} on the outer loop. Note the abrupt change along a vertical line (indicated with the arrow) approximately halfway into the LZS region. Moving to the right of this line, the oscillations change direction and begin to run nearly perpendicular to the charge transfer line (dotted). Again starting at the bottom left corner, the stability diagram of Fig. A.1(b) is the result of sweeping left to right and stepping bottom to top. That is, V_{RP} is on the inner loop and V_{LP} on the outer loop. The abrupt change in the oscillations, which in this case takes place on a horizontal line (arrow), is again parallel to the sweep direction. Observe that in both cases, the line marking the change in the direction of the oscillations intersects the point at which the first bright fringe and an extension of a addition line also meet (circle). At present, however, it is unclear how this observation relates to the distortions in the data.

Since the positions of the oscillations are determined by the S and T_+ energy levels, it is reasonable to think that the observed change in the direction of the oscillations must be related to a change in these energy levels. As noted is Section 4.3, Landau-Zener tunneling

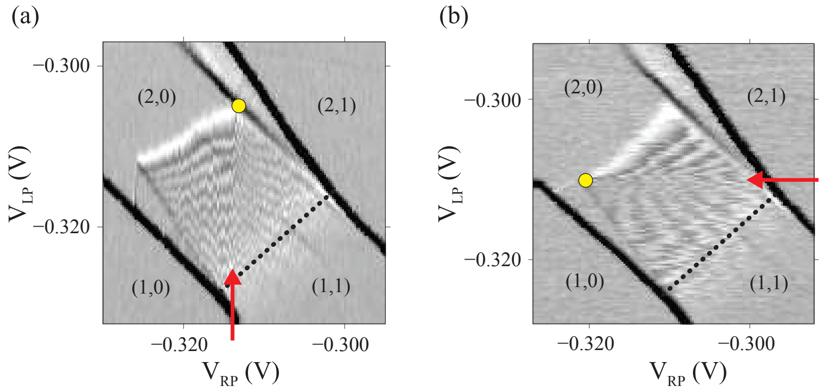

Figure A.1: (a) Stability diagram acquired by sweeping V_{LP} (inner loop) and stepping V_{RP} (outer loop). (b) Sweep V_{RP} and step V_{LP}. The change in the direction of the oscillations occurs on a line parallel to the sweep direction (arrow). This line intersects the point at which the first fringe and an extension of an addition line meet (circle). The position of the charge transfer line is indicated with a dotted line.

can produce a transition from a spin 0 singlet to a spin 1 triplet. Conservation of angular momentum is satisfied since this electron spin flip is associated with a nuclear spin flop. Repeated Landau-Zener tunneling events could build-up the nuclear field (which points in the direction of the external magnetic field) thus changing the Zeeman splitting of the triplets, E_Z, and as a result, the relative positions of the S and T_+ energy levels and the position of the anticrossing [101]. This dynamic nuclear polarization (DNP) effect may by related to the change in the direction of the oscillations but it is unclear why DNP would abruptly change along a line parallel to the sweep direction. Changing the pulse rise time, angle, or period does not eliminate the abrupt change in the direction of the oscillations. The problem is also not related to a lack of synchronization between the LP and RP gate voltage pulses.

Stability diagrams corresponding to various values of QPC charge detector bias voltage, V_{QPC}, are shown in Fig. A.2. Note that the vertical line that marks the change in the character of the oscillations moves to the right as V_{QPC} decreases. Again, it appears to intersect the point at which the extension of the (1,1)$\leftrightarrow$(2,1) addition line and the first

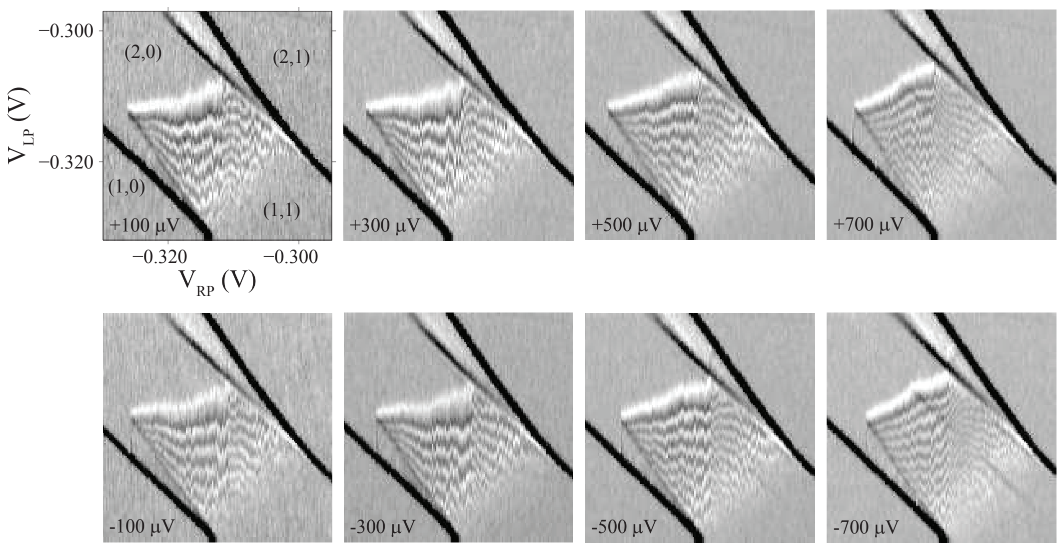

Figure A.2: Effect of V_{QPC} on the LZS oscillations. As the magnitude of the bias increases, the oscillation frequency increases and the first fringe moves away from the charge transfer line.

bright fringe also meet. Perhaps more interesting and important than the distortions in the data is the fact that the LZS oscillation frequency increases as V_{QPC} increases in magnitude. Also the first bright fringe moves away from the charge transfer line as the magnitude of V_{QPC} increases. Recall that an increase in E_Z associated with an increasing external magnetic field produces these same two effects. Apparently, by some as yet unknown mechanism, V_{QPC} (or I_{QPC}) can also change E_Z. Certainly investigating QPC charge detector backaction by studying the effect on LZS oscillations could be the basis of a new project.

Examples of LZS data from a 2014 cooldown of a similar device are shown in Fig. A.3. The stability diagram of part (a) is acquired using the DC-QPC and the stability diagram of part (b) is acquired with the RF-QPC. The distortions in the data have a different character from those of the 2013 cooldown. The reason for showing this data is to point out the fringe furthest from the charge transfer line labeled with an arrow in (b). It is observed only in RF-QPC data and results from the incoherent mixing of the S and T_+ states driven by the 520 MHz, -85 dBm rf bias. Very simply, the pulse no longer has to

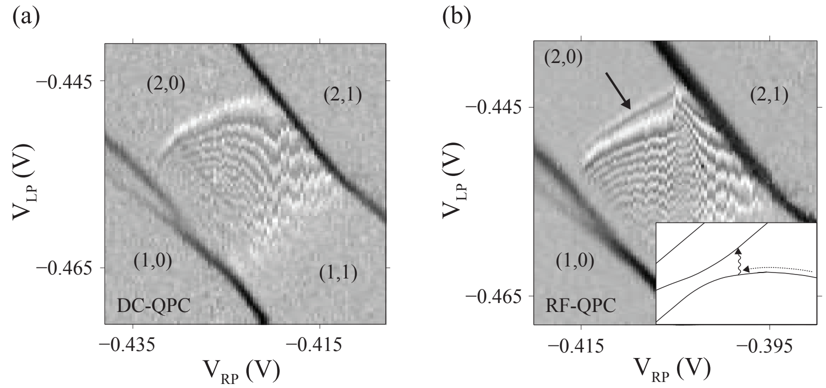

Figure A.3: LZS oscillations measured using the (a) DC-QPC (b) RF-QPC. The additional fringe in the RF-QPC case (arrow) is due to the 520 MHz, −85 dBm rf carrier signal. Inset: S-T_+ mixing occurs when a pulse reaches the position at which $E_{T_+} - E_S = hf$, $f = 520$ MHz. The new fringe corresponds to a pulse that just reaches the point at which this resonance condition is satisfied.

reach the anticrossing for mixing to occur. Energy is absorbed from the rf carrier and the system transitions from the ground state S to the T_+ excited state as shown in the inset to (b).

During the same cooldown, the effect of various gate voltages on the LZS oscillations were investigated, revealing some connection between tunnel rates and distortions in the data. Fig. A.4(a) shows oscillations with slight distortions. Decreasing the top gate from $V_T = -0.540$ V to $V_T = -0.555$ V creates straight oscillations, all parallel to the charge transfer line as shown in (b). This gate voltage change has two effects. It decreases both the tunnel rates to the leads and the interdot tunnel rate. Returning to $V_T = -0.540$ V and then decreasing the right side gate (RS) voltage from $V_{RS} = -0.989$ V to $V_{RS} = -0.999$ V also seems to eliminate the distortions as shown in Fig. A.5. This change similarly decreases the tunnel rates to the leads. However, unlike in the case of decreasing V_T, decreasing V_{RS} pushes the dots closer together and thus increases the interdot tunnel rate. Much work remains to fully understand the source of the distortions in the LZS data but there is some evidence that the dot-to-lead tunnel rates play a role.

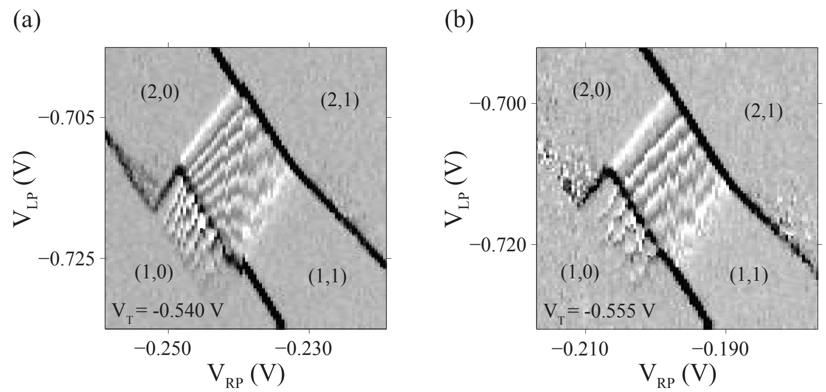

Figure A.4: LZS oscillations for two values of V_T. Decreasing V_T in (b) lowers the dot-to-lead tunnel rates and repairs the distortions shown in (a).

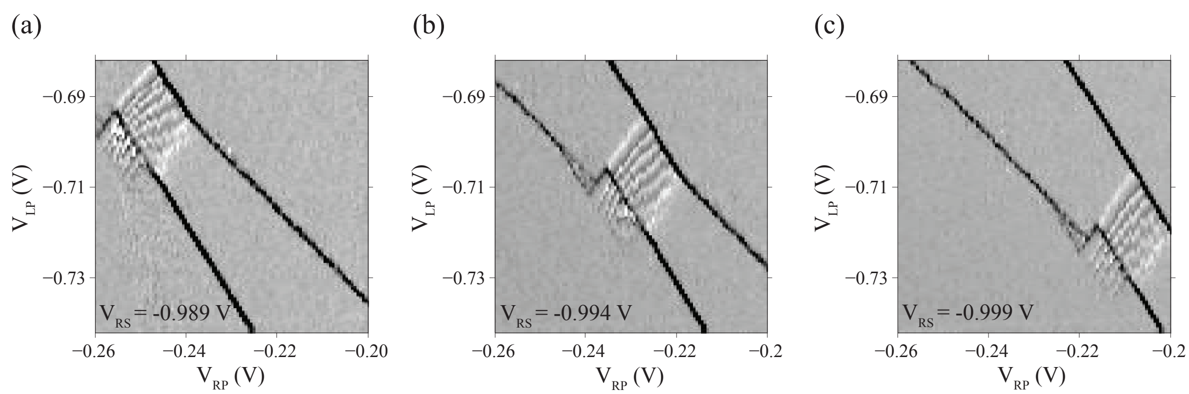

Figure A.5: LZS oscillations for various values of V_{RS}. As V_{RS} decreases [(a) to (c)], the dot-to-lead coupling decreases and the slight distortions present in (a) are eliminated.

Appendix B

Two-Level Systems

This section reviews the theory of quantum mechanical two-level systems. The formalism is needed for discussions of tunnel-coupled quantum dots, the Landau-Zener effect, and two-electron spin qubits. The following development of the theory is similar to that found in Refs. [31] and [106]; notation is borrowed from both. Consider a system described by a Hamiltonian H_0 with eigenstates $|1\rangle$ and $|2\rangle$ and corresponding eigenenergies E_1 and E_2. The 2×2 matrix representation of H_0 in the basis of its eigenstates is

$$H_0 = \begin{pmatrix} E_1 & 0 \\ 0 & E_2 \end{pmatrix}$$

The eigenvalue equations of this system are

$$H_0|1\rangle = E_1|1\rangle$$
$$H_0|2\rangle = E_2|2\rangle.$$

Introduce a coupling between the two states which is represented by a purely off-diagonal, time-independent, Hermitian matrix

$$V = \begin{pmatrix} 0 & \Delta \\ \Delta^* & 0 \end{pmatrix}$$

making the total Hamiltonian $H = H_0 + V$. The matrix V could, for example, describe tunnel coupling between two quantum dots near the charge transfer line of a stability diagram or the coupling of quantum dot electron spin states due to an interaction with the nuclear spins of the GaAs substrate. With the addition of off-diagonal matrix elements to the Hamiltonian, the original basis states, $|1\rangle$ and $|2\rangle$, are no longer eigenstates of the system. The new eigenstates satisfy the following eigenvalue equations:

$$H|a\rangle = E_a|a\rangle$$
$$H|b\rangle = E_b|b\rangle$$

Since this simple model captures some the physics of a chemical bond, the eigenstates are sometimes referred to as bonding, $|b\rangle$, and anti-bonding, $|a\rangle$, states. Not surprisingly, the bonding state has the lower energy of the two. Solving the characteristic equation, $\mathrm{Det}[H - EI] = 0$ (I is the identity matrix), gives the following eigenvalues:

$$E_a = E_m + \frac{\Omega}{2}$$
$$E_b = E_m - \frac{\Omega}{2}$$

where $\Omega = \sqrt{\varepsilon^2 + 4\Delta^2}$, $E_m = \frac{1}{2}(E_1 + E_2)$, and $\varepsilon = E_2 - E_1$. The energy eigenvalues E_1, E_2, E_a, and E_b are plotted as a function of ε (detuning) in Fig. B.1(a). The energies in the absence of coupling, E_1 and E_2, cross at $\varepsilon = 0$. The introduction of coupling produces an anticrossing with energies E_a and E_b forming the branches of a hyperbola. The minimum separation of the branches is $2|\Delta|$ which occurs at $\varepsilon = 0$. The eigenstates of H written in the basis of $|1\rangle$ and $|2\rangle$ are given by

$$\begin{aligned} |a\rangle &= \cos\frac{\theta}{2}e^{-i\phi/2}|1\rangle + \sin\frac{\theta}{2}e^{i\phi/2}|2\rangle \\ |b\rangle &= -\sin\frac{\theta}{2}e^{-i\phi/2}|1\rangle + \cos\frac{\theta}{2}e^{i\phi/2}|2\rangle \end{aligned} \tag{B.1}$$

where $\tan\theta = 2|\Delta|/\varepsilon$. See Ref. [106] (Complement $\mathrm{B_{IV}}$) for a detailed derivation of these expressions.

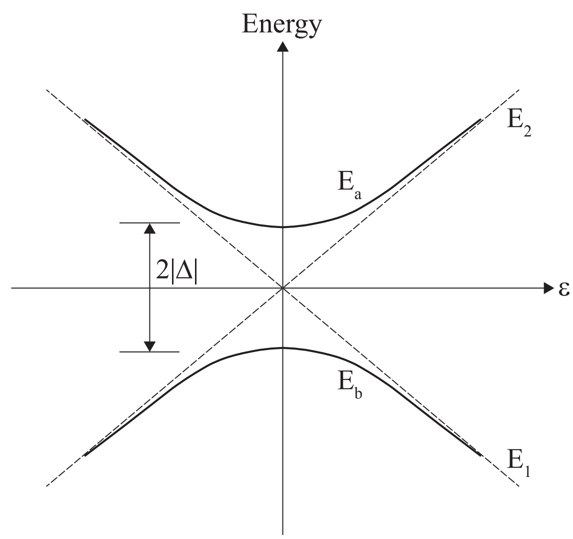

Figure B.1: (a) Energy levels E_a and E_b of the two coupled states as a function of detuning $\varepsilon = E_2 - E_1$. They form branches of a hyperbola with asymptotes given by the energies E_1 and E_2 of the uncoupled states (dashed lines). The off-diagonal matrix element, Δ, which characterizes the coupling, gives a minimum branch separation of $2|\Delta|$ at $\varepsilon = 0$.